



TECHNISCHE  
UNIVERSITÄT  
DRESDEN

**HZDR**



HELMHOLTZ  
ZENTRUM DRESDEN  
ROSSENDORF

# Effect of microstructure on the magnetic properties of transition metal implanted $\text{TiO}_2$ films

## Dissertation

zur Erlangung des akademischen Grades

Doctor rerum naturalium (Dr. rer. nat.)

vorgelegt der fakultät Mathematik und Naturwissenschaften

der Technischen Universität Dresden

von Oğuz Yildırım

geboren am 04.11.1987 in Bornova

Supervisor: Prof. Dr. Jürgen Faßbender

Die Dissertation wurde in der Zeit von 06/12 bis 10/15  
im Institut für Ionenstrahlphysik und Materialforschung  
am Helmholtz-Zentrum Dresden-Rossendorf angefertigt.



1. Gutachter: Prof. Dr. Jürgen Faßbender

2. Gutachter: Prof. Dr. Nikolai Perov

Datum der Einreichung: 03.12.2015

Datum der Verteidigung: 24.02.2016



This work is supported by Initiative and Networking Fund of the German Helmholtz Association, Helmholtz-Russia Joint Research Group *HRJRG* – 314, and the Russian Foundation for Basic Research, RFBR #12 – 02 – 91321 – *SIG*



*to my lovely wife and my family*  
*sevgili eđime ve aileme*





## Abstract

The combined electronic, optic and magnetic properties of transition metal (TM) implanted ferromagnetic  $\text{TiO}_2$  is of interest for spintronic applications. The nature of the observed abundant ferromagnetism in such materials has been investigated for more than one and a half decades, yet still no clear explanation for its appearance can be given. In this thesis, the origin of the ferromagnetic order in TM: $\text{TiO}_2$  systems is studied by investigating the interplay between structural order, defects and incorporation of implanted ions within the host lattice. The defect properties of the host  $\text{TiO}_2$  are altered by preparing different microstructures of  $\text{TiO}_2$  (e.g. amorphous, polycrystalline anatase and epitaxial anatase). The difference in microstructure is also found to influence the incorporation of the implanted ions with the host lattice. The crystallographic incorporation of the implanted TM atoms is found only in crystalline films. Moreover, it is observed that the suppression of the dopant related secondary phases can also be achieved by changing the microstructure. The obtained experimental results are compared with the existing theoretical frameworks, while the most relevant one describing our findings is elucidated. Based on this discussion, we propose an ideal microstructural candidate for a dilute magnetic oxide material based on our results.



## **Kurzfassung**

Die kombinierten elektrischen, optischen und ferromagnetischen Eigenschaften von  $\text{TiO}_2$ , welches mit einem Übergangsmetall (TM) dotiert wurde, sind für Anwendungen in der Spintronik von hoher Bedeutung. Obwohl dieses Material seit mehr als anderthalb Jahrzehnten untersucht wird, kann derzeit noch keine eindeutige Erklärung für den beobachteten Ferromagnetismus gegeben werden. In dieser Arbeit wird die Ursache für die ferromagnetische Ordnung in TM: $\text{TiO}_2$ -Systemen untersucht, indem der Zusammenhang von struktureller Ordnung, Defekten und der Einlagerung der implantierten Ionen im Wirtsgitter analysiert wird. Durch die Verwendung unterschiedlicher Mikrostrukturen (z.B. amorphes, polykristalliner Anatas und epitaktischer Anatas) wurden auch die Defekteigenschaften des Wirts-Titanoxid variiert. Dabei zeigte sich ein Einfluss der unterschiedlichen Mikrostrukturen auf die Einlagerung der implantierten Atome in das Wirtsgitter. So konnte die Substitution von Ti-Atomen durch Atome des dotierten Übergangsmetalls nur in kristallinen Filmen beobachtet werden. Weiterhin wurde herausgefunden, dass die vom Dotanden hervorgerufenen Sekundärphasen durch die initiale Mikrostruktur unterdrückt werden können. Die experimentellen Ergebnisse wurden mit aktuellen Theorien verglichen. Zusammenfassend wird ein Überblick über die wichtigsten Ergebnisse gegeben, auf Basis welcher eine optimale Mikrostruktur für ein verdünntes magnetisches Oxid vorgeschlagen wird.



---

## Contents

---

<b>1</b>	<b>Introduction</b>	<b>2</b>
1.1	Spintronics . . . . .	2
1.2	Dilute magnetic oxides . . . . .	5
<b>2</b>	<b>Fundamentals</b>	<b>13</b>
2.1	Introduction . . . . .	13
2.2	Magnetism in diluted magnetic oxides . . . . .	13
2.2.1	Possible locations of dopant $3d$ ions in an oxide matrix . . . . .	14
2.2.2	Mean field model . . . . .	15
2.2.3	Bound magnetic polaron model . . . . .	16
2.2.4	Charge transfer model . . . . .	17
2.2.5	Ferromagnetism in undoped oxides . . . . .	19
2.2.6	Extrinsic sources of ferromagnetism . . . . .	20
2.3	Motivation . . . . .	21
<b>3</b>	<b>Experimental</b>	<b>24</b>
3.1	Sample preparation . . . . .	24
3.1.1	DC magnetron sputtering . . . . .	24
3.1.2	Ion implantation . . . . .	27
3.2	X-ray methods . . . . .	29
3.2.1	X-ray diffraction . . . . .	29
3.2.2	X-ray absorption . . . . .	31
3.2.2.1	Synchrotron radiation . . . . .	31
3.2.2.2	Physics of X-ray absorption . . . . .	31
3.3	SQUID magnetometry . . . . .	35
3.3.1	Avoiding magnetic contamination . . . . .	37
3.4	Positron annihilation spectroscopy . . . . .	38
<b>4</b>	<b>TM Implantation into Different <math>\text{TiO}_2</math> Structures (TM = Co, Mn, V)</b>	<b>43</b>
4.1	Experiments . . . . .	43

4.2	Co <sup>+</sup> implantation: from diluted paramagnetism to superparamagnetic clusters . . . . .	45
4.2.1	Cluster-free Co <sup>+</sup> -implanted TiO <sub>2</sub> thin films . . . . .	45
4.2.1.1	Experiments . . . . .	45
4.2.1.2	Structural properties . . . . .	46
4.2.1.3	Implantation-induced structural defects . . . . .	47
4.2.1.4	Magnetic properties . . . . .	50
4.2.1.5	Local environment of implanted Co atoms . . . . .	51
4.2.1.6	Summary . . . . .	52
4.2.2	Revealing nano-clusters within Co <sup>+</sup> -implanted TiO <sub>2</sub> thin films . . . . .	54
4.2.2.1	Experiments . . . . .	54
4.2.2.2	Structural properties . . . . .	54
4.2.2.3	Magnetic properties . . . . .	57
4.2.2.4	Local environment of implanted Co atoms . . . . .	59
4.2.2.5	Summary . . . . .	61
4.3	Mn <sup>+</sup> implantation: from a non-magnet to a ferromagnet . . . . .	63
4.3.1	Experiments . . . . .	63
4.3.2	Relation between lattice damage and defects . . . . .	64
4.3.3	Electrical transport properties . . . . .	65
4.3.4	Local environment of implanted Mn atoms . . . . .	66
4.3.5	Magnetic properties . . . . .	67
4.3.6	Summary . . . . .	69
4.4	V <sup>+</sup> -implanted TiO <sub>2</sub> thin films . . . . .	71
4.4.1	Experiments . . . . .	71
4.4.2	Magnetic properties . . . . .	71
4.4.3	Summary . . . . .	74
<b>5</b>	<b>The effect of the open volume defects on the magnetic properties of V:TiO<sub>2</sub> films prepared by doping during deposition</b> . . . . .	<b>76</b>
5.1	Experiments . . . . .	76
5.2	Structural Properties . . . . .	77
5.3	Investigation of the open volume defects . . . . .	78
5.4	Magnetic, optical and electrical properties . . . . .	79
5.5	Summary . . . . .	81
<b>6</b>	<b>Conclusions</b> . . . . .	<b>84</b>
6.1	Defects in TiO <sub>2</sub> . . . . .	84
6.2	Formation of secondary phases . . . . .	85
6.3	Evolution of the ferromagnetism in different microstructures of TiO <sub>2</sub> . . . . .	87
<b>7</b>	<b>Acknowledgments</b> . . . . .	<b>91</b>







# CHAPTER 1

---

## Introduction

---

In this chapter, a brief introduction to spin-based electronics and its relation to magnetic semiconductors is given. The concept of spintronics is discussed in the frame of electron motion. A discussion on the integration of spintronics concepts into oxide based semiconductors is given. In the final section a brief history of dilute magnetic oxides along with the controversial experimental results and the state of the art are presented.

### 1.1 Spintronics

The word spintronics is born from the marriage of the intrinsic angular momentum of the electron, its spin, and conventional electronics, which to-date has ignored the spin of the electron. The magnetic moments in solid materials are associated with their electrons. An electron has two distinct motions, (i) one is along an orbit around nucleus and is called orbital motion and (ii) a motion about its own axis, which causes an intrinsic angular momentum called spin angular momentum. Those two motions of an electron are coupled by so-called spin-orbit interactions. The orbital motion of an electron around nucleus, similar to a current in a loop of wire, induces a magnetic field, which is perpendicular to the direction of motion. The intrinsic angular momentum of an electron has two different

orientations, which is a consequence of spin motion. This was initially visualized and described by the hydrogen fine-structure [1] and the Stern-Gerlach experiments [2, 3]. These experiments suggested two possible states for the intrinsic angular momentum both of which have the quantum number of  $s = 1/2$ . The quantum numbers associated with an electron spin follow the characteristic pattern of

$$s = \frac{\sqrt{s(s+1)}\hbar}{2\pi}, m_s = \pm \frac{1}{2} \quad (1.1)$$

The potential energy induced by magnetic field,  $B$ , in applied field direction is  $U = \pm\mu_B B$ . Two different spin states, thus two different intrinsic angular momentum directions of an electron lead to energy splitting between both states, which is induced by a magnetic field (Fig. 1.2).

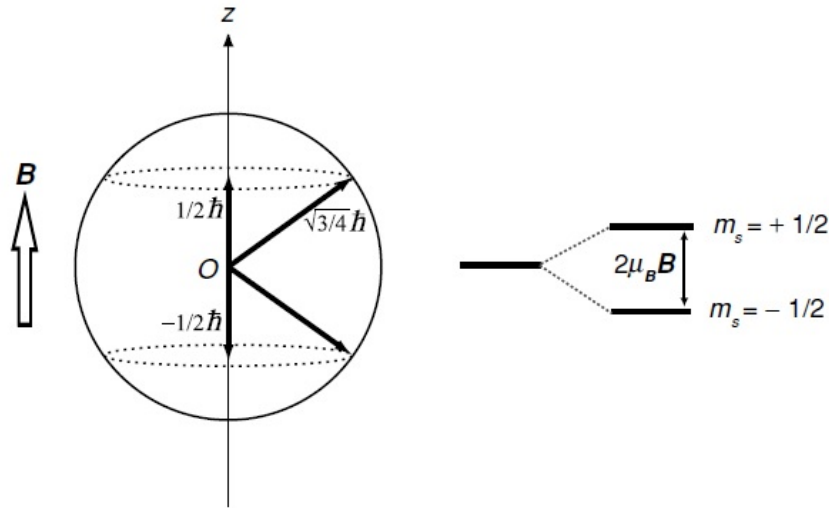


Figure 1.1: The energy splitting of the both spin states of an electron under an applied external magnetic field.

The energy splitting of the spin states of an electron has well-defined quantum states. Therefore, this property of an electron gives us the opportunity to use it in magnetic memory devices, where two different and well-separated states refer to logic states of "0" and "1". Hence, the concept of spintronics brings a possibility to use the spin degree of freedom of an electron, apart from its charge degree of freedom, which is currently being used for charge-based applications [4]. The control of the spin state of an electron inside a material is done either by controlling the population and the phase of the whole

system, or by manipulating the spin state of a single or few-spin systems [5], which also defines the magnetic orientation of the system. Spintronics is already a well-appreciated area. It has already shown its significance by the discovery of giant magneto-resistance (GMR) in 1988 [6, 7]. The GMR effect is based on the relative orientation of two thin magnetic layers separated by a non-magnetic layer. When both magnetic layers are aligned in the parallel configuration, an applied current passes through whole stack with a low resistance. However, in the anti-parallel configuration, electrons passing through the stack experience a giant electric resistance, due to increased scattering in the opposite layer (Fig.1.2).

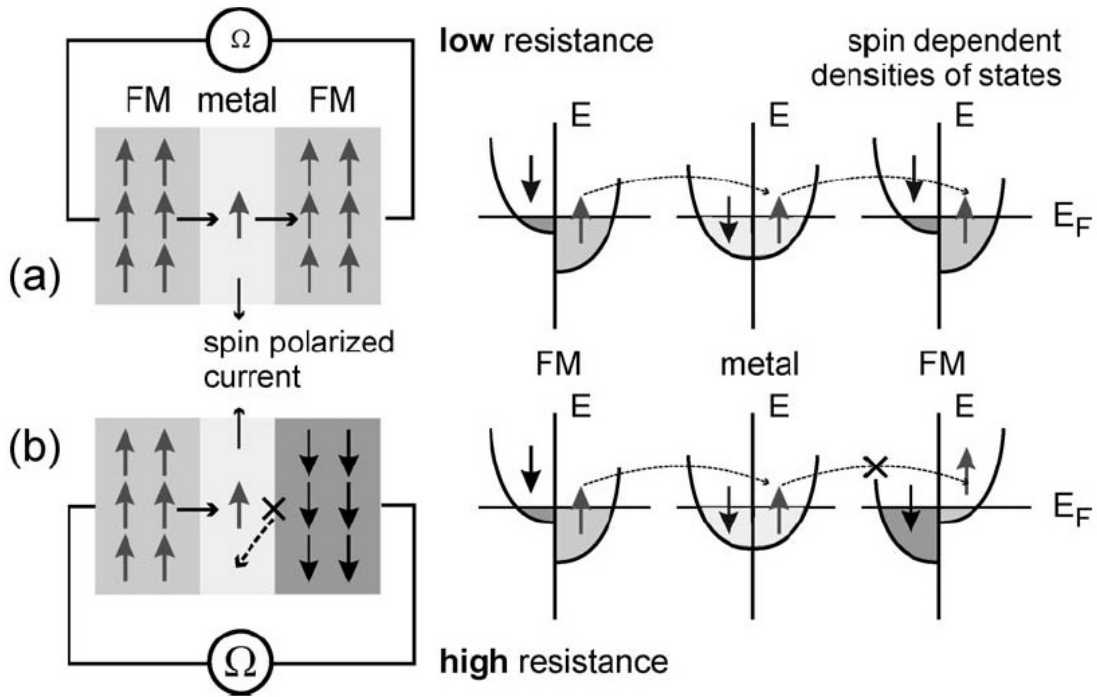


Figure 1.2: Schematic illustration of GMR stack, which consists of two ferromagnetic layers. The magnetic orientation of the ferromagnetic layers with respect to each other defines the resistance state, i.e. (a) shows parallel alignment, where a spin polarized electron can travel from one majority state to another by being exposed to a low resistivity. (b) in the antiparallel configuration, since the majority spins can only be scattered into majority spins of the second layer, they experience a giant magneto resistance while passing through antiparallel oriented layers. [8].

Even though it has currently been used in many memory devices, GMR-based magnetic storage is a power consuming and strongly size dependent technology. The power consumption of GMR-based devices occurs due to motions of the read-head, which has to

travel freely above magnetic layer in order to read or write each individual bits. The size dependency occurs due to magnetic stability of small particles (e.g. superparamagnetism appear for ferromagnetic particles below a certain diameter). More recently, Slonczewski [9] and Berger [10] independently predicted that, a current passing through perpendicularly to the plane of a metallic multilayer stack can induce a spin transfer torque (STT), which can re-orient the magnetization direction in one of the layers. In a STT-based magnetic memory device reading/writing occurs without a motion of any parts. Moreover, in an STT-based device, bits/stacks are perpendicularly aligned, therefore magnetic bits are more stable in horizontal configuration as compared to the GMR-based devices. The STT-induced magnetization change can also be achieved within a dilute magnetic semiconductor (DMS) material [11]. Furthermore, instead of applying electrical current through the stack, an applied electric field can be used to induce STT in a DMS [12]. Applying an electric field helps to avoid Joule heating, which makes the system more stable and less energy consuming. Also, as a natural property of DMS, having low remanence magnetization values in turn, makes the DMS-based systems more efficient as compared to conventional metal ferromagnets, thus makes them better candidates for STT-based systems.

## 1.2 Dilute magnetic oxides

The family of dilute magnetic oxide (DMO) materials has long been considered as an integral part of the DMS family. A DMS material consists of a host semiconducting material, in which doped magnetic ions are incorporated. The doping of a magnetic element into a semiconductor material is expected to form substitutional sites, where the dopant magnetic ion replaces a host atom and supplies a local magnetic moment. Reaching a sufficient amount of such substitutional sites, and thus a sufficient amount of magnetic moment, leads to the onset of ferromagnetism [13] (Fig. 1.3).

Early studies on DMS materials were focused on II-VI systems [15], in which magnetic interactions mostly governed by antiferromagnetic coupling, thus resulting in antiferromagnetic and spin-glass behavior, or, for some cases only at very low temperatures ( $T_c \leq 1.8$  K), giving rise to ferromagnetism [16]. Afterwards, the discovery of III-V materials

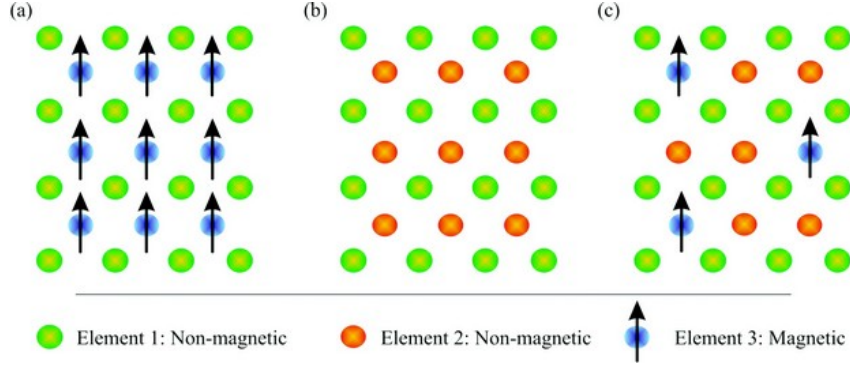


Figure 1.3: Evolution of the magnetic structure of a DMS. (a) a ferromagnetic material, where the magnetic ions are evenly distributed and their magnetic moments are aligned in same direction. (b) shows a non-magnetic semiconductor host, while (c) illustrates the magnetic structure of a DMS, where magnetic moment carrier dopant atoms have a low concentration and they incorporated into the host lattice [14].

[17, 18] (GaAs, InAs, etc.) brought the Curie temperature of DMS systems, closer to room temperature, at around 170 K. Magnetic interactions in ferromagnetic DMS systems are mediated by mobile charge carriers between localized magnetic moments (explained detailed in chapter 2). The strict relation between the charge carriers and magnetic state of the material brings also the possibility to control electrically the magnetic properties of these systems and are already exploited in industry in field-effect transistors [19] and spin-LED devices [20].

The idea of using oxide-based semiconductor materials as DMS materials, was introduced by Dietl's prediction on TM doped p-type ZnO [21]. After the aforementioned study, there have been huge research efforts put into oxides in order to implement them in current DMS research. The experimental concept of an oxide-based DMS is rather straightforward. As shown in figure 1.3 similar to a DMS, introducing ferromagnetism into a non-magnetic oxide host material is achieved by means of doping a few atomic percent of magnetic ion, (e.g. transition metals). Therefore, the general formula of a oxide-based DMS can be expressed as

$$A_{1-x}M_xO_y \quad (1.2)$$

where,  $A$  represents the host metal ion, which forms the initial oxide material,  $M$  represents the doped transition metal ion, which is expected to introduce magnetic moment

and  $O$  represents the oxygen atom, which can have different concentrations depending the host material (e.g. for ZnO,  $y$  is 1, while for TiO<sub>2</sub>,  $y$  is 2). The first successful experimental attempt on oxide-based magnetic semiconductor was performed by Matsumoto et. al. at 2001, by cobalt doping into anatase TiO<sub>2</sub> [22]. This study attracted much interest, but on the other hand, also sparked a strong debate on the origin of the observed ferromagnetism. Following this study, Co doped TiO<sub>2</sub> was of interest. Many different experimental methods, i.e. pulsed laser deposition [23], magnetron sputtering [24], sol-gel processing [25], molecular beam epitaxy [26], ion implantation into single crystals [27] were employed. In the figure 1.6, the amount of the publications on cobalt doped magnetic TiO<sub>2</sub> is plotted versus years. Initial efforts were mostly put on to prepare oxide-based systems. Apart from different preparation methods, almost all of the  $3d$  metals were introduced into the oxides in order to dope them magnetically [28, 29, 30, 31]. As an example, for ZnO, magnetic moment per dopant atom values, which are extracted from saturation magnetization values at room temperature, for different  $3d$  dopant types were experimentally studied and given in figure 1.5 [28]. In this study, it is also shown that magnetic anisotropy exists in the samples. The confirmation of the dopant-host incorporation was tried to be done by a variety of the experimental characterization methods. For example, X-ray absorption experiments were performed, in order to deduce the electronic state and local coordination of the dopant cobalt atoms within anatase TiO<sub>2</sub> matrix [32]. This study showed that cobalt atoms have +2 oxidation state with a distorted octahedral oxide coordination, when they replace titanium sites in the lattice. It is worth to note that, Ti either in anatase or in rutile TiO<sub>2</sub> has +4 oxidation state. So that, there is also a charge imbalance in TM doped oxide systems, if the substitution of the dopant is successfully achieved. Moreover, X-ray absorption methods were also employed to investigate the origin of the magnetic moments by performing X-ray magnetic circular dichroism (XMCD) [33, 34, 35]. XMCD measurements showed that magnetic moments can be originated from Ti-based defects [33], as well as from the dopant atom [35]. Likewise, anomalous Hall effect (AHE) was initially proposed to be a unique property to confirm the DMS character of Fe doped TiO<sub>2</sub> [36]. Because, AHE is one of the most important criteria for a DMS material for its intrinsic origin of ferromagnetism, for example for GaMnAs systems [37, 38]. Additionally, it is recently found that introducing ferromagnetic order

into anatase  $\text{TiO}_2$  requires a certain amount of free charge carriers [39]. Thus, the results on charge transport properties reflects a strict relation between magnetic properties of DMOs and their charge carriers.

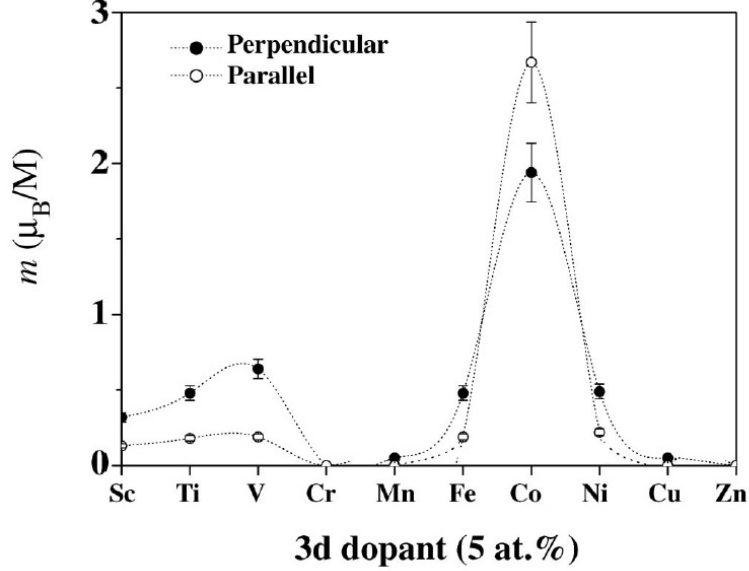


Figure 1.4: Experimental saturation magnetization values of 5 at. % TM doped ZnO films measured at room temperature (TM=Sc-Cu) [28].

Accordingly, in 2003, initial questions regarding to the source of the observed ferromagnetism were raised due to observation of dopant related nanoclusters within the oxide matrix [40]. As shown in figure 1.6, interest was quite high in Co-doped  $\text{TiO}_2$  until the observation of precipitated secondary phases. The formation of the TM dopant-based nanoclusters was found to be dependent on the heat treatment parameters either in Co implanted films [27] or in during-deposition-doped anatase  $\text{Co}:\text{TiO}_2$  films [41]. If the clusters are larger than superparamagnetic limit, or their blocking temperatures are above room temperature, the ferromagnetic response of the material will be dominated by the clusters and this ferromagnetic behavior persists up to dopants Curie/blocking temperature, which may lead to wrong conclusions if the characterization is not performed carefully. For instance, for Co metal, if the clusters are larger than 10 nm, the measured magnetic moment will be as high as  $1.7 \mu_B/\text{Co}$  and their blocking temperature will be higher than room temperature [42]. Moreover, it is found that the AHE can be observed in spite of the presence of metallic cobalt clusters [43]. The co-occurrence of

metallic cobalt nanoclusters and AHE is explained in such way; if an electric field is applied to each nanoparticle along their  $x$ -axis, it will lead to current in each particle along  $y$ -direction, which is proportional to clusters magnetization component in  $z$ -axis. Since  $\text{TiO}_2$ , in which all of the cobalt clusters are embedded, is conductive, nanoclusters inject current into host  $\text{TiO}_2$  along its  $y$ -axis, in the presence of an external magnetic field, and this current will be probed as AHE. In their study, Shinde *et. al.* also found that AHE appears in the temperature range, where the superparamagnetic cobalt nanoclusters are ferromagnetic (below  $T_B$ ). Therefore, this study also showed that only AHE cannot be used as a tool to distinguish intrinsic and extrinsic origins of FM within DMOs.

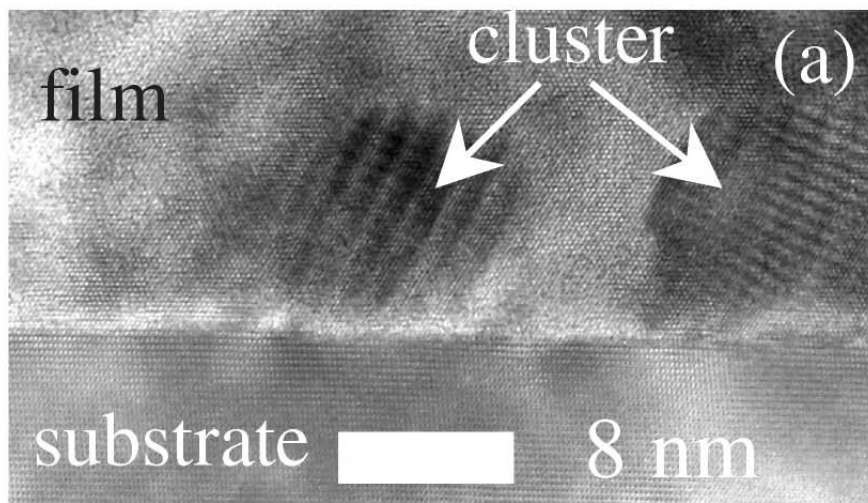


Figure 1.5: Transmission electron microscopy images of fine metallic cobalt clusters found in rutile  $\text{TiO}_2$  [43].

Also, studies on undoped oxide systems, i.e. for  $\text{ZnO}$  or  $\text{Sn}_2\text{O}$  [44] and  $\text{HfO}_2$  [45] revealed weak ferromagnetism at room temperature, when oxygen is reduced from the lattice. In undoped  $\text{TiO}_2$  it is found that ferromagnetism occurs due to coupling of  $\text{Ti}^{+3}$  ions.  $\text{Ti}^{+3}$  ions form upon an oxygen atom removal from the lattice and sufficient amount of oxygen vacancies is found to lead a ferromagnetic onset in  $\text{TiO}_2$  [46]. In accordance with this, an extra care was started to be given either to avoid or to reveal extrinsic sources of ferromagnetism in such systems. Despite the controversial experimental findings, the origin of the abundant ferromagnetism has emerged as the most important question waiting for an answer, “if the observed ferromagnetism is originated from an



intrinsic source, what is the coupling mechanism?”. The reason for this question is that the common super-exchange and double-exchange coupling interactions can explain up to second neighboring magnetic interactions, while for magnetically doped oxide semiconductors, such an interaction can be up to the tenth neighbor. This question still remains unanswered. Moreover, the ferromagnetism observed in oxide-based DMS cannot be explained by using Zener model, while the magnetic interactions in III-V based DMS systems are well-explained using the same model. Therefore, this conflict between oxide-based and III-V based DMS materials, results in a separate classification for the oxide-based systems as dilute magnetic oxides (DMOs).

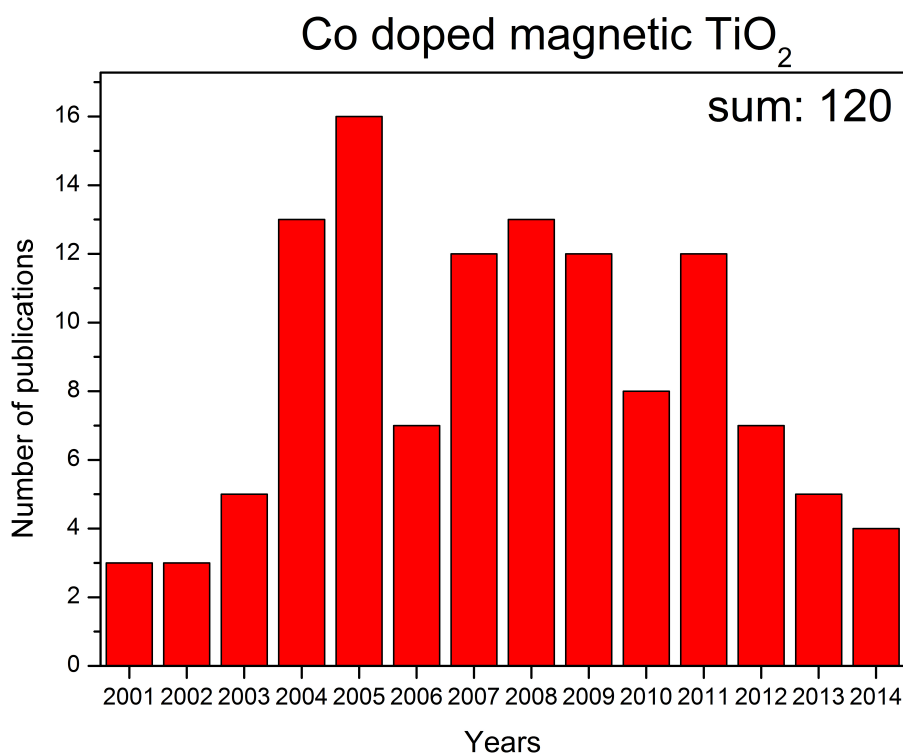


Figure 1.6: The number of publications on magnetic properties of Cobalt doped TiO<sub>2</sub>. The search was performed by using ISI database, by using “Co, TiO<sub>2</sub>, magnetic ”keywords. The results are carefully read through and refined only to DMO related publications.

The current knowledge about ferromagnetic DMOs, depending on the latest experimental results can be summarized as; (i) FM can be introduced to an oxide host already at 5 at.% open-volume defect concentration [46] and structural grain boundaries are the major contributors to the defect-induced FM [47]; (ii) in order to initiate intrinsic ferromagnetic order within a TM doped anatase TiO<sub>2</sub>, there is a threshold free carrier

concentration, which was recently found to be around  $1.8 \times 10^{18} \text{cm}^{-3}$  [39]; (iii) the control of the magnetic state of a Co-doped anatase  $\text{TiO}_2$  can be done by means of electric fields, i.e. without an applied electric field, the sample shows paramagnetic properties, while the presence of an electric field induces ferromagnetic ordering [48].



### 2.1 Introduction

In Chapter 2, a brief discussion will be given in order to explain the possible sources of FM in DMOs. The theoretical frameworks, which are proposed to explain the observed ferromagnetic properties in DMOs, are discussed by comparing existing experimental studies.

### 2.2 Magnetism in diluted magnetic oxides

As explained in the previous chapter, the experimental concept of preparing a DMO appears to be simple, TM doping into  $\text{TiO}_2$  with a few atomic percent concentration, below the percolation threshold, by having the intention of replacing some Ti atoms in the  $\text{TiO}_2$  lattice with the dopant. Eventually, expectation is to achieve substitutional dopant sites, which are separated by long distances, yet ferromagnetically ordered. If the ferromagnetic interaction occurs due to dopant-host incorporation, it has to cover large distances. Such a long-range magnetic interaction is inexplicable in terms of common super-exchange and double exchange interactions, which take into account nearest-

neighbor interactions only up to second nearest neighbors. Therefore, the discovery of the oxide-based diluted magnetic semiconductors, or diluted magnetic oxides, fueled also a debate on the origin and the mechanism of the observed FM in such systems, and this debate still continues for almost one and a half decades.

In spite of controversial results, common points can be extracted from earlier studies in order to have a better understanding and also find a better route to prepare DMO materials. In most of cases, dopant concentration is found to be an independent parameter [49], while the amount and type of defects [50], including type of the dopant has already been shown to affect the magnetic properties of DMOs by experimental results [51, 52, 53] as well as theoretical calculations [54]. Additionally, as Calderon and Sarma [55] predicted and experimentally established [39], free charge carriers have a large impact on FM of DMOs, which is similar to DMS systems.

### 2.2.1 Possible locations of dopant $3d$ ions in an oxide matrix

As mentioned in the previous section (2.2), the experimental concept of DMOs is straightforward, a  $3d$  metal is introduced into an oxide material at concentrations of a few atomic percent. In this section, upon TM doping, possible locations of the dopant atoms within the oxide matrix are discussed and described.

When a small concentration of dopant is introduced into the oxide matrix, we can postulate following dopant configurations (I) the dopant atoms can form antiferromagnetic (AFM) pairs, as depicted with red circles in figure 2.1. AFM pairs are either formed over oxygen ligands, which leads to super-exchange, or due to nearest-neighbor interactions, which leads to direct d-d interactions, which is known for Cr and Mn, for example; (II) dopants can form clusters, which involves three or more dopant atoms. Clusters can also include host atoms by forming secondary phases, depicted by the green circle in figure 2.1. Those clusters can give rise to a ferromagnetic signal, if they contain any ferromagnetic phase; (III) lastly, dopant atoms can be well separated from each other. Such an isolated ion, can be formed either by dopant-host substitution or as interstitials. The desired location of the TM dopant atom within a DMO is a substitutional site, which is believed to introduce FM by interacting with other substituting TM ions.

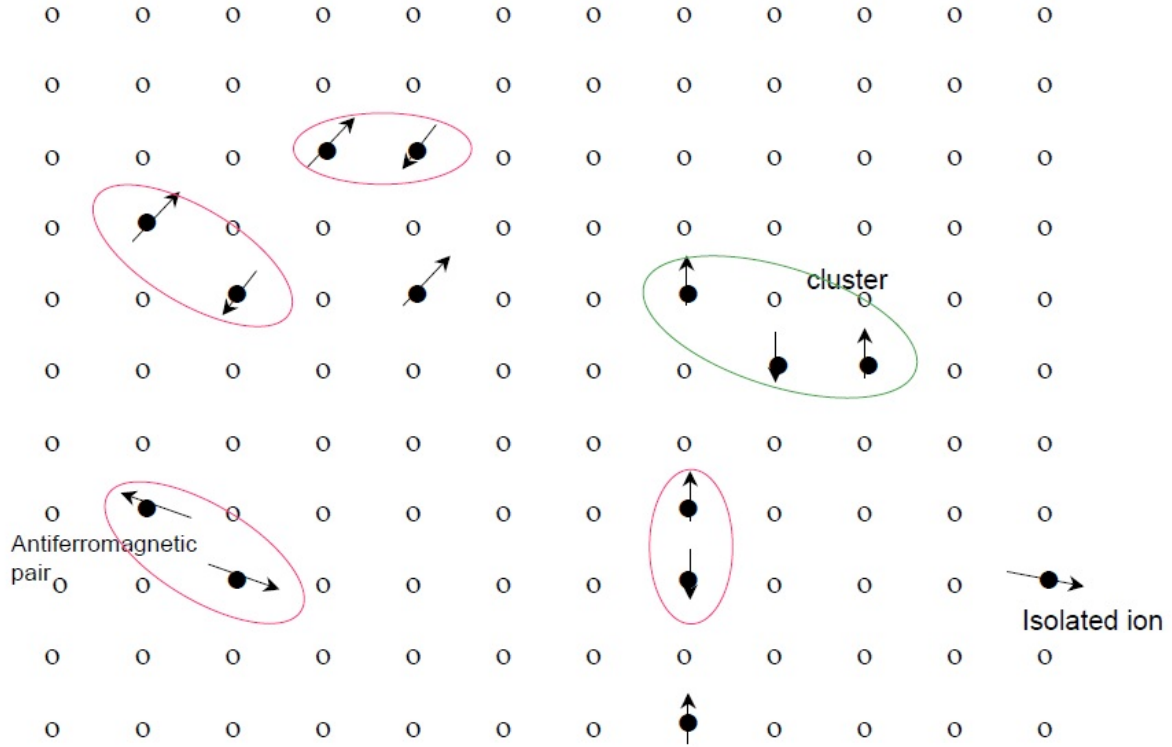


Figure 2.1: Possible dopant (filled dots) locations within host oxide (empty dots) lattice, below percolation concentration [50].

### 2.2.2 Mean field model

The ferromagnetic order in III-V semiconductors, has already been successfully explained by the mean field model [21]. The mean field model for DMS materials is based on RKKY (Ruderman-Kittel-Kasuya-Yosida) and Zener interactions. Both interactions give equivalent results in the mean field approximation. The Zener model suggests that ferromagnetic order between localized spins occurs via delocalized charge carriers. The ferromagnetic order, lowers the energy of the carriers, which are associated with spin-split bands. In the RKKY model, if the mean field approximation is employed, the mean distance between the nearest spins is much lower than the Fermi wave length of the carriers. The shorter distance leads to ferromagnetic interactions between the localized spins. In order to fulfill the requirements of the ferromagnetic ordering according to mean field Zener model, localized spins in the system have to have short nearest neighbor distance (while at the same time being larger than a certain value, where antiferromagnetic interactions start). The presence of a certain amount of free charge carriers is also required.

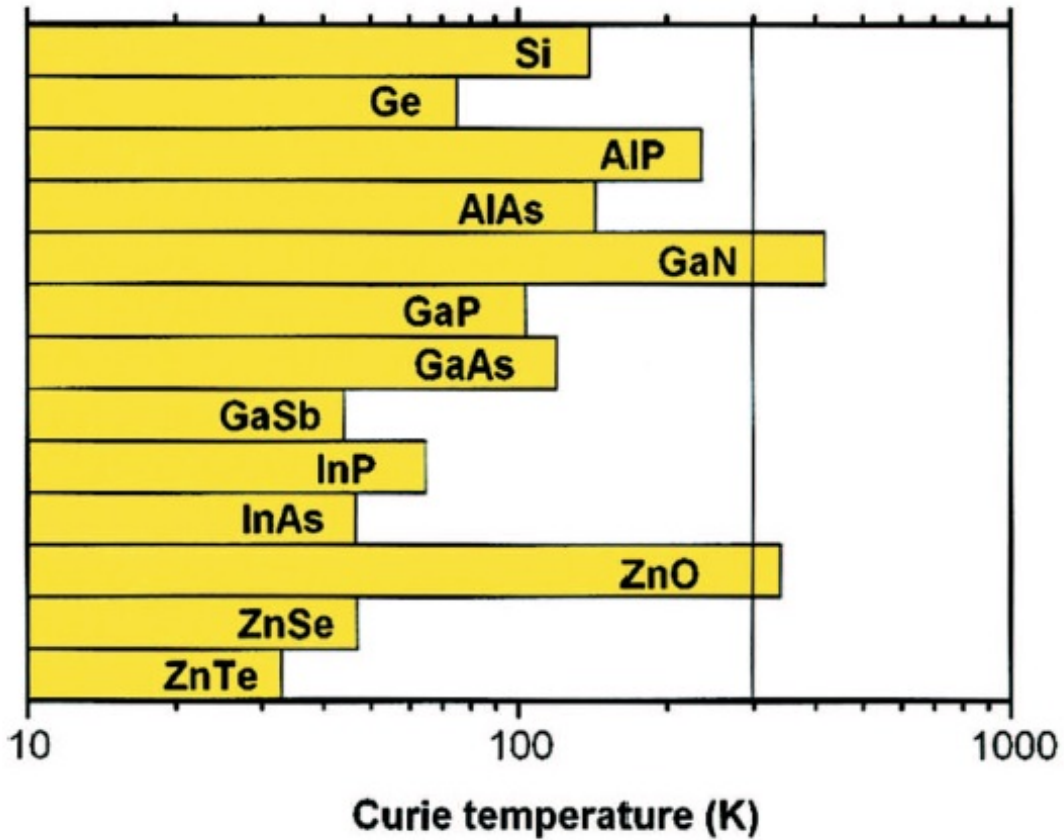


Figure 2.2: Calculated Curie temperatures of various p-type DMS materials, containing 5 at.% Mn and  $3.5 \times 10^{20} \text{ cm}^{-3}$  hole concentration[21]

More examples on the prediction of DMS systems containing 5 at.% Mn and  $3.5 \times 10^{20} \text{ cm}^{-3}$  holes can be found in the figure 2.2. Therefore, the mean field Zener model explains III-V DMSs very well, however it fails explaining either DMOs [56, 57, 48] or insulating FM DMS and DMOs [58, 59], because in this approximation, charge carriers are treated as free carriers and nearest neighboring distances are shorter as compared to the nearest-neighboring distances of TM atoms within DMOs.

### 2.2.3 Bound magnetic polaron model

Bound magnetic polarons (BMPs) were initially used to explain changes of carrier concentration in Eu-based chalcogenides [60]. Afterwards, in 2005, Coey suggested the use of BMPs to explain high temperature ferromagnetic order in TM doped oxides [50]. A BMP consists of an impurity electron and forms a shallow donor, where the local

magnetization is inhomogeneous. A shallow donor in n-type oxides is associated with an oxygen based defect. Thus, an electron accompanied by a defect will be confined in an hydrogen-like orbital. Increasing the donor concentration expands the orbital radius and eventually, orbitals overlap and form an impurity band. Up to a certain donor concentration, electrons are localized in the band, however exceeding this critical donor concentration leads to delocalization of the impurity band states. The delocalized impurity band electrons can interact with the dopant  $3d$  electrons and form bound magnetic polarons. In order to spread this ferromagnetic interaction over the whole sample volume, the majority of the BMPs should overlap. Only overlapping magnetic polarons can align their spins with respect to each other. Otherwise, this coupling remains localized in the vicinity of each polaron volume and the average magnetic response of the material will be paramagnetic (Fig. 2.3). The percolation threshold of BMPs depends on dopant cation concentration and the amount of the defects.

The BMP model, in contrast to the charge transfer model (which, will be discussed in section 2.2.4), depends also on dopant concentration and type, which, for some of the experimental studies, also has found to affect magnetic properties of DMOs [61]. BMP theory has already been suggested to be valid many times by numerous studies [62, 63, 64]. Up to now, it is the most appreciated framework by the community. Yet, a debate about BMP theory and its approach to explain the observed FM within the insulating TM doped oxides [59] and high Curie temperatures, is still ongoing.

## 2.2.4 Charge transfer model

The charge transfer model is based on charge reservoirs induced by TM doping. The idea of charge reservoirs was developed due to inconsistent charge states of the TM dopants when they substitute the host cation. For example, Ti in  $\text{TiO}_2$  has a +4 oxidation state, however, the possible dopants, Co, Mn or Fe tends to have different oxidation states, i.e. +1, +2, +3 or a mixture of those states when they replace Ti atom within  $\text{TiO}_2$ . Therefore, this situation results in charge imbalance, which leads to creation of charge reservoirs. According to the charge transfer model for ferromagnetic ordering, there must be three main components existing:



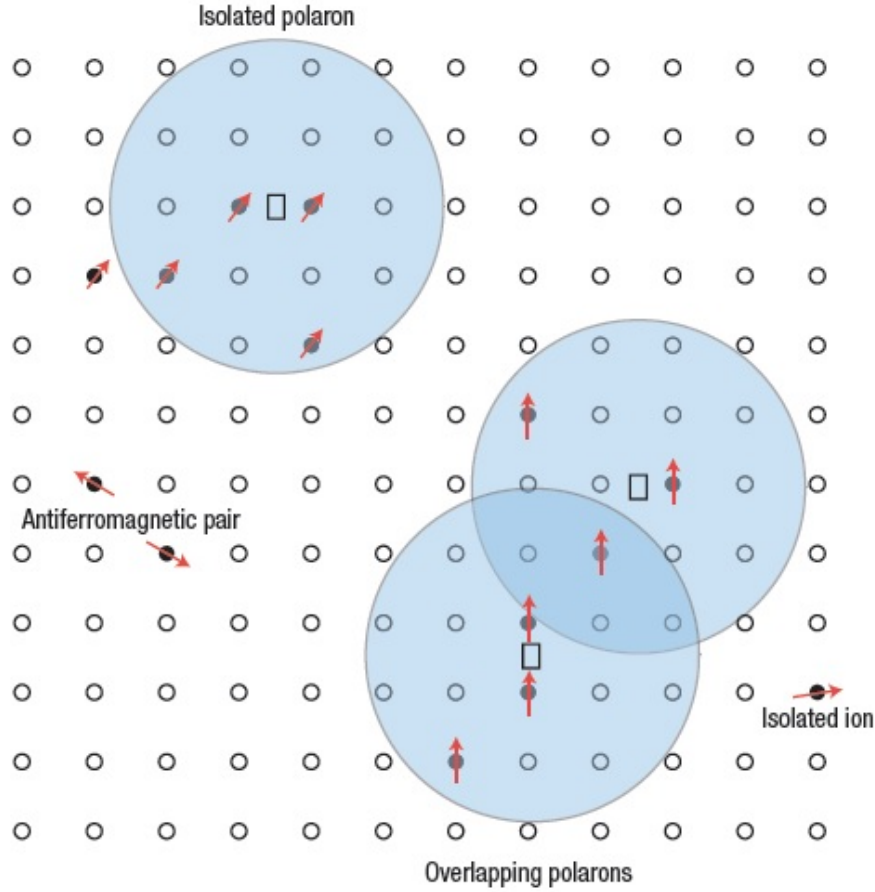


Figure 2.3: Bound magnetic polaron formation in the vicinity of the shallow donor states and their percolation [50]

- (i) a defect-based impurity band with high density of states around the Fermi level;
- (ii) a charge reservoir as an electron supplier, which occurs due to mixed electronic state of the dopant atoms;
- (iii) an effective exchange integral  $I$  associated with the defect states.

In a classical Stoner ferromagnet, which contains an uniform magnetization over the whole volume, the ferromagnetic state is defined by the density of states at the Fermi level ( $N(E_F)$ ) in the unsplit band, while in the charge transfer model the Stoner criterion  $IN(E_F) > 1$  is satisfied by a large exchange integral  $I$ . This can only occur, when the

impurity band compensates the kinetic energy of the band splitting and the electrons are transferred from the charge reservoir to the impurity band. Thus, uniformity is not necessary. Therefore, only defect containing regions become ferromagnetic (Fig. 2.4). The excess electrons, which are available due to mixed electronic state of the dopant cation, percolate in the structural defects. Accordingly, FM occurs in a very small sample volume, where defects are located and  $3d$  cations do not contribute directly to FM. This idea may explain FM observed in undoped defect-rich oxides and insulating TM doped oxides [65, 47]. In order to create charge reservoirs, it is necessary to have mixed valance states among either the host atoms, e.g.  $\text{Ti}^{+3}$  and  $\text{Ti}^{+4}$  or in the dopant atoms, e.g.  $\text{Co}^{+2}$  and  $\text{Co}^{+3}$  with almost equal fractions. However, most of the experimental studies suggest usually a single oxidation state for the majority of the TM atoms. Therefore, only the charge transfer model alone is not sufficient to explain all of the observed results as a general framework.

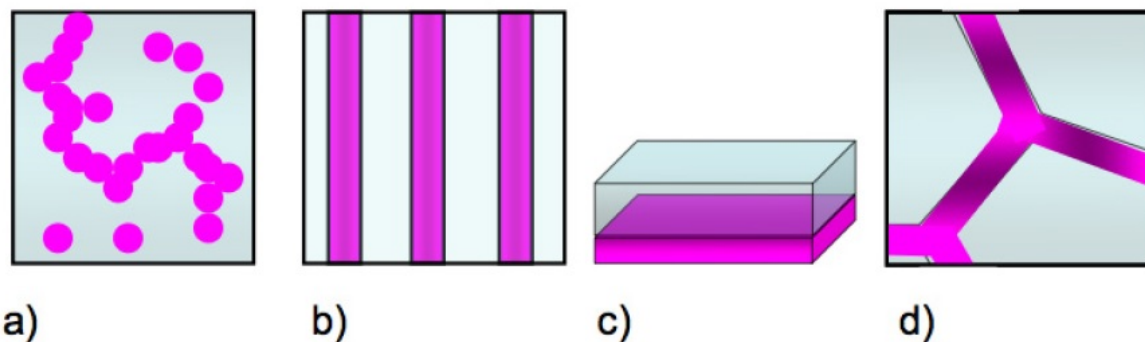


Figure 2.4: Possible defect distributions inside a thin film. (a) random distribution of point defects, (b) spinodal decomposition, (c) interface defects and (d) grain boundary defects [54]

### 2.2.5 Ferromagnetism in undoped oxides

Further experimental studies on oxides showed that the magnetic TM dopant is not an essential ingredient in order to introduce FM in semiconducting oxides. As already reported, a mechanical stress induced by a hammer [66], oxygen-poor growth conditions [67] or grain boundaries [47] can induce FM without the presence of any TM dopant. Moreover, even the presence of a magnetic impurity dopant can lead to defect-induced

FM in Co:ZnO system, in which the dopant Co atoms remain paramagnetic [68, 33]. The aforementioned studies showed that there should be something else behind this unusual ferromagnetic order than  $d$ - or  $f$ - shell based magnetism. For instance, in CaO system has been demonstrated that dilute  $\text{Ca}^{+2}$  vacancies within a rocksalt structure induce ferromagnetic ground states. This FM in undoped oxides is also called as  $d^0$  magnetism, due to absence of a  $3d$  dopant. As introduced in previous sections, even in the possible intrinsic scenarios, defects, i.e. vacancies, grain boundaries, etc., play an important role in the magnetic order of the DMOs. Moreover, such defects have a long recognized importance as they dictate the electrical and optical properties of the host semiconductor by creating anomalies in the band structure. Recent studies have shown that defects may be responsible for initiating hybridization at the Fermi-level, which leads to spin-split states and establishes a long range ferromagnetic order between defects [69]. Moreover, a recent study suggested that already 5 at.% vacancy concentration can promote FM above room temperature [46]. Such a pure defect-induced ferromagnetic order in semiconducting oxides is an undesired situation for DMS applications and is tried to be avoided.

### 2.2.6 Extrinsic sources of ferromagnetism

In contrast to the debate on the origin of intrinsic FM in DMOs, there is a general consensus on the extrinsic sources of FM. Extrinsic sources of FM are twofold: dopant-induced secondary phases, such as elemental metallic nanoclusters, or unwanted compound phases, i.e.  $\text{CoTiO}_3$ ,  $\text{Co}_2\text{O}_3$ ,  $\text{Co}_3\text{O}_4$  within Co:TiO<sub>2</sub>. Nanocluster formation depends on a variety of preparation parameters (i.e. deposition rate, substrate/annealing temperature etc.), and probing such fine structures within a relatively large matrix can be a challenge. Average cluster sizes can differ from 1 nm to hundreds of nanometers [70, 71] and usually it is not possible to detect them by means of conventional X-ray diffraction measurements [27], due to their small size and low concentration. Metallic clusters of naturally ferromagnetic elements, if they are above the superparamagnetic limit or if the measurement temperature is below the superparamagnetic blocking temperature, can give rise to a ferromagnetic signal. Secondary phases can have variety of compositions, and accordingly a variety of magnetic properties, including ferromagnetic phases. If the

secondary phase formation is induced by spinoidal decomposition, the decomposed secondary phase accommodates the same crystal orientation with the host, and therefore makes it even harder to be probed experimentally [72]. The second possible origin of extrinsic FM in DMOs is magnetic contamination. Sample handling with stainless steel tweezers can already contaminate the sample with a speck of a magnetic material, which can give around  $10^{-6}$  emu total magnetic signal [73] and it is worth mentioning that this amount of magnetic signal is already large enough to draw wrong conclusions.

## 2.3 Motivation

The possibility of controlling magnetic properties by means of electrical manipulation or vice versa, makes DMOs a hot research topic. Unfortunately, as already described previously, theoretical understanding and the experimental preparation of a DMO is not trivial. Although there still is no comprehensive framework, which consistently explains entire experimental results for DMOs, common points from each framework may help to proceed one step further. Defects, in the context of either for BMP model or for the charge transfer model are suggested to be necessary in order to introduce FM in DMOs and have been already experimentally confirmed [62, 74, 63]. The second point is the incorporation of the dopant within the host lattice. The determination of local coordination of the dopants can be used as a tool to distinguish between metallic/oxide secondary phase states and the intended oxidation state (substitutional). Moreover, if the charge transfer model is valid, identifying the dopants oxidation state is necessary in order to find out the possible mixed electronic states of the dopant atoms. As a last point, prevention from the possible extrinsic sources of FM, either having contamination-free sample handling or suppressing any kind of cluster/secondary phase formation, is also important.

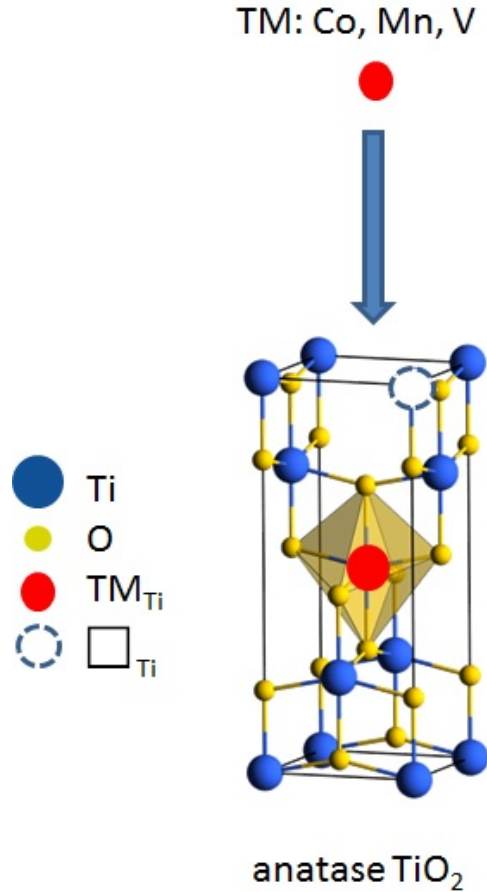


Figure 2.5: An illustration of effect of the TM implantation into anatase  $\text{TiO}_2$ . The implantation leads formation of substitutional sites along with creation of open-volume defects.

Therefore, in this thesis, it is aimed to change defect properties of the host  $\text{TiO}_2$  by changing the initial microstructure and to identify dopants' local coordination within different microstructures of  $\text{TiO}_2$  and observe resulting magnetic properties. Moreover, the creation of more open-volume defects upon ion-implantation is used as an advantage, due to need of sufficient amount of defects (Fig. 2.5). Accordingly, the best microstructure, in which ferromagnetic order can be introduced by avoiding possible extrinsic sources was tried to find. During the whole process, samples are prevented from magnetic contamination by taking due care (see chapter 3).



### 3.1 Sample preparation

In this study, two different approaches of DMO sample preparation are used. All of the films, which are presented in this thesis, have been deposited by means of magnetron sputtering. The different approaches have been employed in TM doping process into  $\text{TiO}_2$ . Most of the experiments were performed on TM implanted  $\text{TiO}_2$  samples, which are doped after deposition, however, in parallel, alloy targets were used to prepare in-situ vanadium doped samples. Details are explained in chapters 4 and 5.

#### 3.1.1 DC magnetron sputtering

A schematic view of a DC magnetron sputtering system is depicted in figure 3.1. A target material, which is aimed to be deposited on a substrate, acts as a cathode and sits on top of permanent magnets. A water cooling system helps to protect magnets from overheating, which may cause a permanent damage of the magnets. The anode, which is made out of a metal and surrounds the target in order to decrease the cathode-anode distance. The short distance between cathode and anode allows us to ignite the plasma at relatively low voltages. Facing cathode the substrates are mounted on a sample holder,

which may be floated, grounded or biased. In this study, the substrates are mounted on a floated sample holder. The substrates, depending on the aimed microstructure, may be heated by using a heating element within the sample holder.  $\text{Ar}^+$  gas acts as the medium, in which the electrical discharge is initiated. Due to an applied electric field,  $\text{Ar}^+$  ions are accelerated to high energies and finally hit the target. Collisions between the target atoms and gas ions lead to removal of the target atoms. This event is also called sputtering. The target, along with the source components (i.e. magnets, cooling system, etc.) and the sample holder are kept under vacuum. In our system the base pressure is less than  $5 \times 10^{-7}$  mbar.

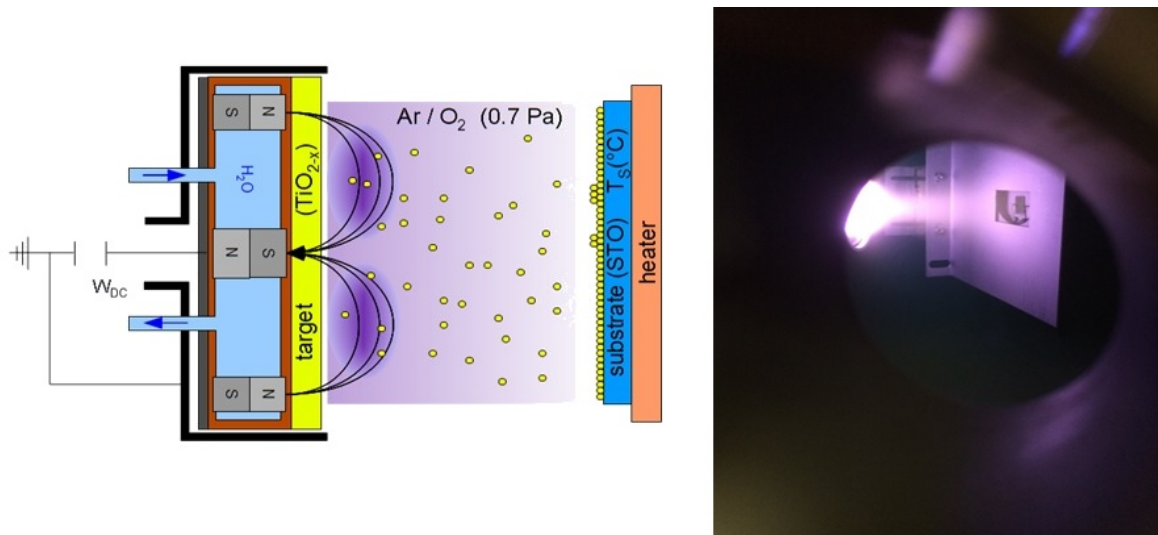


Figure 3.1: A schematic view of a DC magnetron sputtering deposition system along with its real image. Sketch has been taken by courtesy of Dr. Steffen Cornelius [75].

The sputtering process is a self-sustained process when there is high concentration of  $\text{Ar}^+$  ions in the plasma. The  $\text{Ar}^+$  ion density increases due to inelastic collisions in the gas, which leads to the creation of more electron-ion pairs. Moreover, the collisions of the  $\text{Ar}^+$  ions and the target result in secondary electron formation. The secondary electrons accelerate away from the target into the discharge, where they increase the ionization of the gas by inelastic scattering. At this point, the discharge starts to glow, due to excitations of the gas atoms. In order to sustain the plasma state of the discharge, the probability of collisions between the electrons and the Ar atoms should be sufficient. At low gas pressures, this probability becomes too small due to the large mean free path



of the electrons, which causes loss of the electrons from the discharge and eventually an insufficient number of ionized atoms. On the other hand, if the gas pressure becomes too high, frequent collisions prevent the electrons from ionizing the gas, therefore, the discharge is quenched.

In order to increase the sputtering efficiency further, magnets are placed in such a configuration so that the magnetic field, which penetrates into the target, generates a close path on targets surface. The secondary electrons become trapped and move along a helical path in the magnetic field. Therefore, the presence of the magnetic field increases the number of secondary electrons close to the target surface and thus the number of bombarding ions. This increases the deposition rate and allows us to maintain the plasma even at low gas pressures.

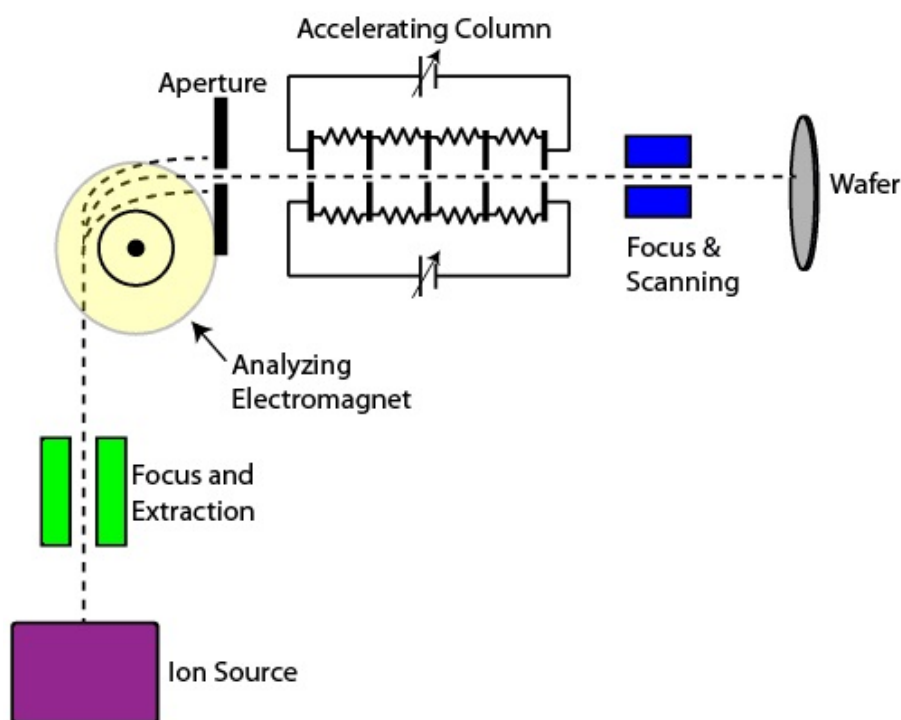


Figure 3.2: A schematic view of an ion implantation setup along with its elements [76].

Due to its high deposition rate, relatively high quality (even for thick films) and high reproducibility, DC magnetron sputtering is desirable for scientific and industrial applications. Moreover, it is applicable to a variety of different materials, from oxides to metals, including hard coatings, low friction coatings, decorative coatings, and even

semiconductor applications for transistors and other functional materials [77]. On the other hand, some of the drawbacks of DC magnetron sputtering can be listed as follows: (i) magnetic targets are not desirable due to interference of its magnetic field with the magnets field, which may lead to a non-uniform and mis-aligned magnetic fields on and through the target; (ii) Due to its high growth rate, it is challenging to grow ultra-thin films; and, (iii) compared to molecular beam epitaxy, the quality of the structures is lower.

### 3.1.2 Ion implantation

In the ion implantation process, energetic ions are accelerated towards a solid material and modify its structural and functional properties. Within this thesis, ion implantation is used to dope  $\text{TiO}_2$  films with transition metal ions and also to create defects.

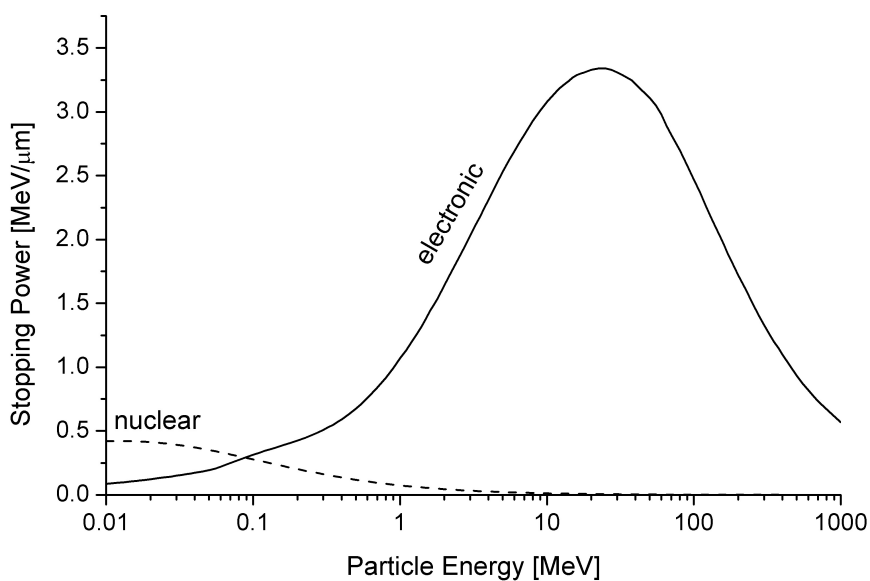


Figure 3.3: Ion energy dependent cross-sections for nuclear and electronic stopping [78].

Figure 3.2 shows a sketch of an ion implanter. During the ion implantation process, ions are generated in an ion source. The generated ions are pulled by the focus and extraction electrodes and reach a mass analyzer. The mass analyzer is composed of an electromagnet, which can be tuned in such way that it can provide an exact amount

of force in order to let only the ions with desired charge and mass pass through. Subsequently, the ions are accelerated at a high potential, by which they gain the desired kinetic energy for the implantation into the target. When an ion undergoes collisions with the target atoms, it loses its energy. The energy loss in ion-solid interactions occurs due to electronic and nuclear stopping. The electronic stopping of an ion is related to inelastic collisions, i.e. excitation and ionization of the target atoms. Such energy loss does not create atomic displacements in the target, usually it dissipates as heat. Electronic stopping is effective in the high energy regime and its cross-section is proportional to the velocity of the implanted ion. In contrast, nuclear stopping occurs as a consequence of elastic collisions of an ion within solid. Therefore, nuclear stopping can cause atomic displacements. If the displaced atom has a high enough energy to lead to displacement of other atoms in the solid, a cascade of recoiled atoms can be created. Nuclear stopping dominates the low and intermediate ion energy regions (Fig. 3.3). Combining both sources of energy losses within a solid, the average rate of an energy loss usually around some tens of eV/Å [79].

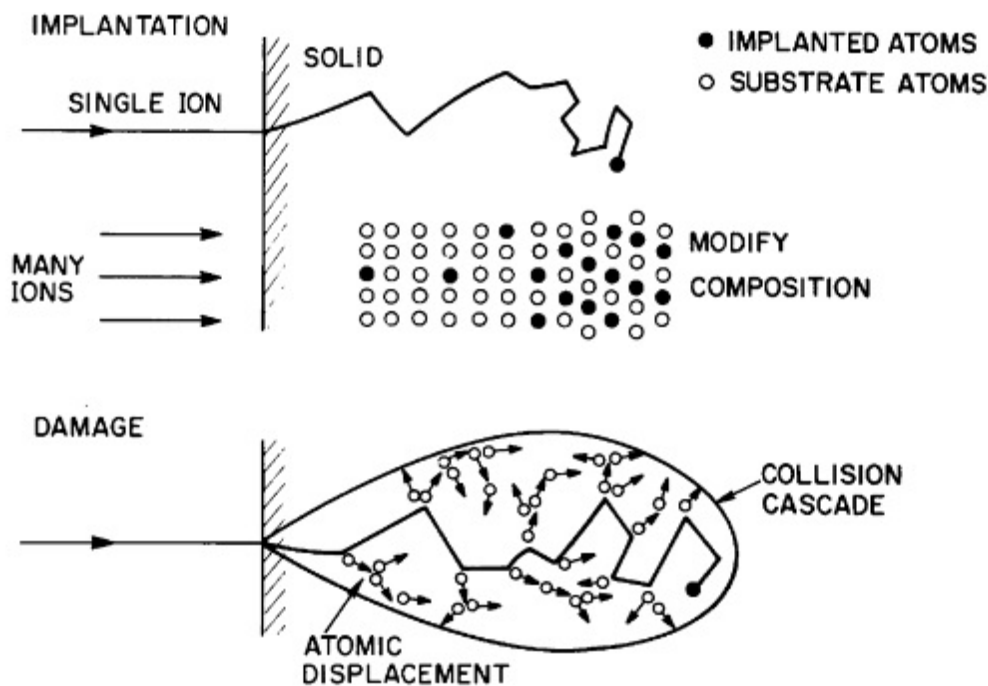


Figure 3.4: A schematic of ion-solid interactions [79].

Ion implantation is a well-developed method for semiconductor industry. Ion implantation, unlike the most of other doping processes, offers the possibility to introduce individual dopant atoms into a target, far from thermal equilibrium [80]. On the other hand, defects are created from the interaction of implanted ions with target atoms (Fig. 3.4). Defects are often considered unwanted in a solid, i.e. semiconductors are usually annealed upon ion implantation in order to reduce the defect formation and also to electrically activate the dopant atoms. In DMOs, as already explained in the previous chapter, defects are one of the key components to achieve ferromagnetism. Most of the previous studies on DMOs were done either by growing/preparing samples at high temperatures or room temperature growth accompanied by a subsequent annealing process. Such heat treatments recover the host crystalline structure including annealing the defects out, which may lead to collapsing of ferromagnetism. Ion-implantation offers a unique benefit in this case as it gives the opportunity to control exactly the amount of doping by the ion flux. Moreover, it is a contamination free process [81].

## 3.2 X-ray methods

### 3.2.1 X-ray diffraction

X-rays have wavelengths between  $1 \text{ \AA} - 100 \text{ \AA}$ , which is of the same order of the lattice spacing of a crystalline solid. Therefore, X-rays are used for structural investigations of a crystalline solid. A crystalline solid consists of periodically arranged atoms and this arrangement can be defined in reciprocal space (or so-called  $k$ -space). In the reciprocal space, a lattice of a solid can be represented by a reciprocal vector ( $\mathbf{Q}$ ), which involves reciprocal lattice vectors. These are in turn, based on real space lattice vectors  $\mathbf{a}$ ,  $\mathbf{b}$  and  $\mathbf{c}$  and can be expressed as follows;

$$a^* = \frac{2\pi(\mathbf{b} \times \mathbf{c})}{\mathbf{a} \cdot (\mathbf{b} \times \mathbf{c})}, b^* = \frac{2\pi(\mathbf{a} \times \mathbf{c})}{\mathbf{a} \cdot (\mathbf{b} \times \mathbf{c})}, c^* = \frac{2\pi(\mathbf{a} \times \mathbf{b})}{\mathbf{a} \cdot (\mathbf{b} \times \mathbf{c})} \quad (3.1)$$

The X-ray scattering vector  $\mathbf{q}$  is in the form of  $ha^* + kb^* + lc^*$ .  $\mathbf{Q}$  can be expressed in terms of lattice plane distances ( $d_{hkl}$ ) as

$$|\mathbf{Q}_{hkl}| = \frac{2\pi}{d_{hkl}}n \quad (3.2)$$

In the constructive conditions the scattering vector will follow the reciprocal lattice,  $\mathbf{q} = \mathbf{Q}_{hkl}$ . As shown in figure 3.5, since the scattering vector is  $|\mathbf{q}| = 2|\mathbf{k}|\sin\theta$ , the Laue condition for diffraction, which is also known as Bragg formula can be written as [82];

$$2d_{hkl}\sin\theta = n\lambda \quad (3.3)$$

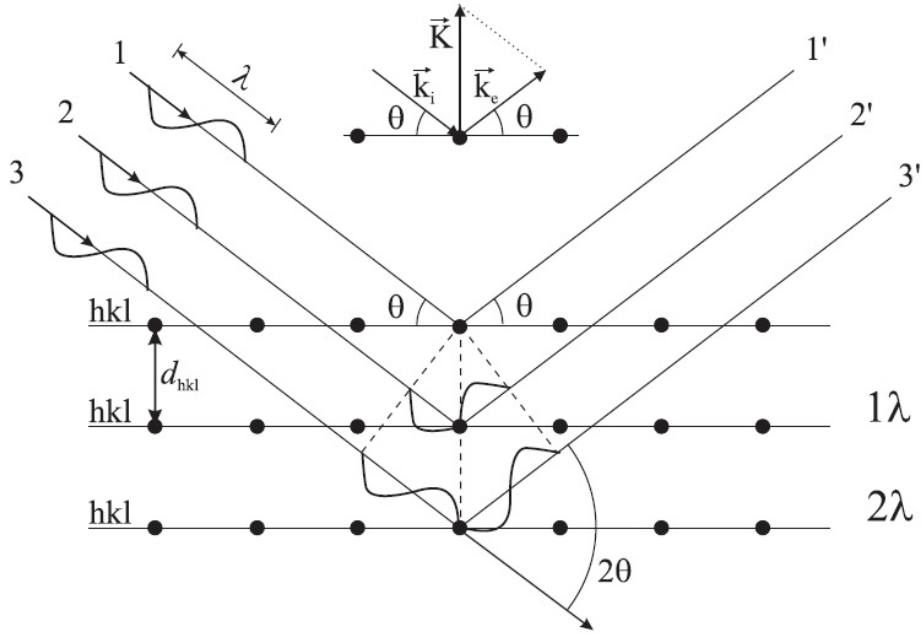


Figure 3.5: Reflection of X-rays from atomic planes of a crystalline solid.

Phase identification of a crystalline solid is done by means of  $\theta$ - $2\theta$  measurements, named after its measurement geometry. By definition, the incoming beam strikes the sample at an angle of  $\theta$ , while the X-ray detector is always kept in  $2\theta$  angle with respect to the incoming X-ray beam (Fig. 3.6). The scattering vector is perpendicular to the sample normal, therefore only the distances ( $d_{hkl}$ ), which are parallel to the sample normal, are probed by X-rays. If the Bragg equation is satisfied, the reflected beam intensity increases dramatically, which is observed as a diffraction peak. By scanning over a range of  $2\theta$ , a diffraction pattern can be formed and the most abundant phase in a sample can be

identified in a diffraction pattern.

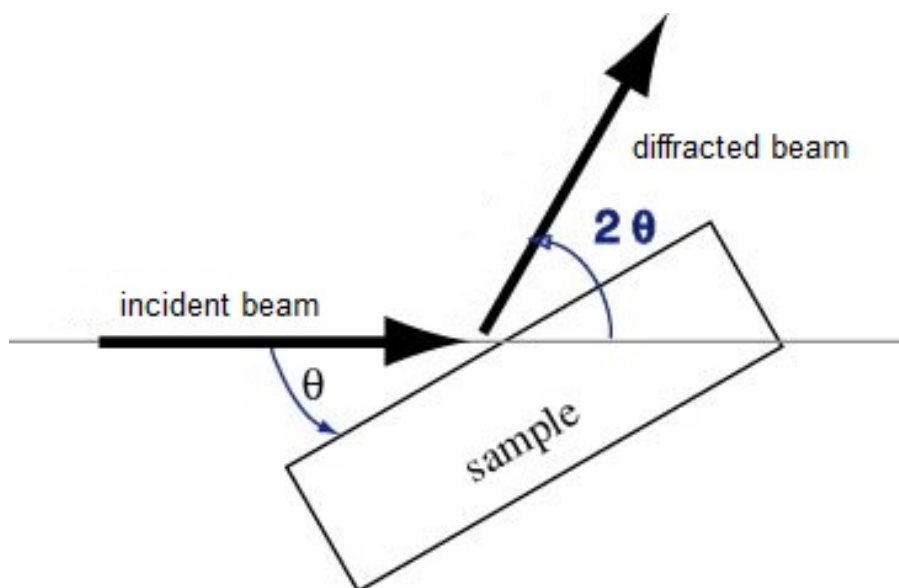


Figure 3.6: An illustration of  $2\theta$ - $\theta$  measurement geometry.

## 3.2.2 X-ray absorption

### 3.2.2.1 Synchrotron radiation

In a synchrotron accelerator, electrons are accelerated at around GeV. Subsequently, electrons are transferred into a storage ring. In the storage ring, the electrons gain speed accelerated to  $\approx 0.9 c$  (light speed) and their path is kept stable by electro-magnets (Fig. 3.7). X-rays are produced in an undulator and delivered to the end stations, which is equipped with shutters, monochromator, mirrors and slits. The monochromator allows the user to define the beam energy, which is illuminating the sample, while the polarization of the beam along with the beam size, focus, intensity and the other optical parameters can be adjusted by mirrors, slits and polarizers [83].

### 3.2.2.2 Physics of X-ray absorption

X-rays, owing to their energies, is defined as ionizing radiation. Therefore X-rays can have sufficient energy to eject a core level electron from an atom. For each element there is a specific binding energy for core electrons, thus removal of an electron can give an unique information about electronic states of a material. The absorption of X-rays can

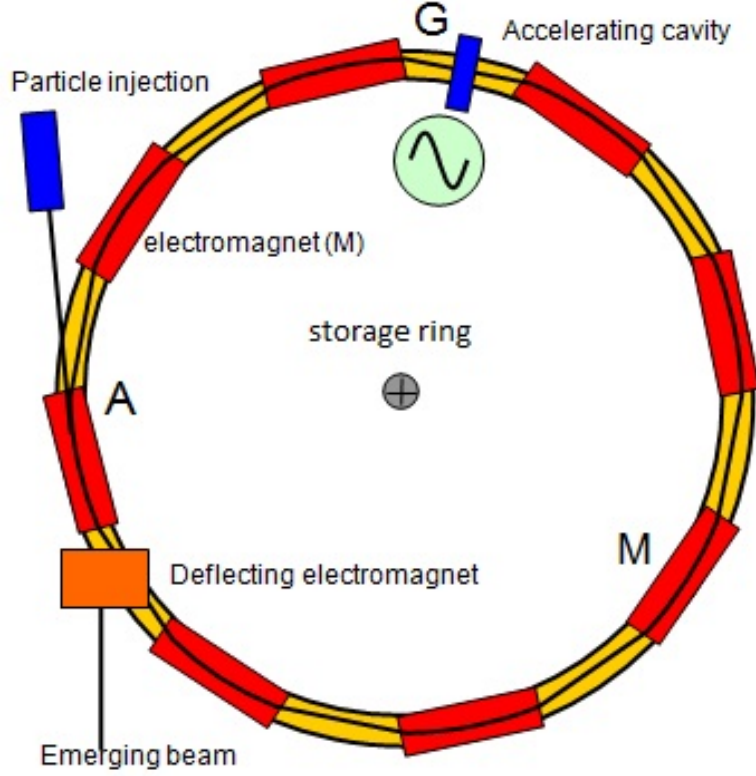


Figure 3.7: A schematic of synchrotron radiation facility [84].

simply be expressed by using Beers law [85]

$$\frac{I(E)}{I_0} = e^{-\mu(E)x} \quad (3.4)$$

where  $I_0$  is the beam intensity before interacting with the material,  $I(E)$  is the transmitted beam intensity after interacting with a material,  $x$  is the thickness of the material and the  $\mu(E)$  is the absorption coefficient. The absorption coefficient depends on the density of the material ( $\rho$ ), nuclear charge ( $Z$ ) and the atomic mass of the element ( $A$ ) and the incident X-ray energy ( $E$ ) [86].

$$\mu \approx \frac{\rho Z^4}{AE^3} \quad (3.5)$$

If the X-ray energy is scanned on a material, at a certain energy, an abrupt increase occurs at the emitted X-ray intensity, which belongs to an electron ejection and is also called "edge jump" [87]. The electronic state of the ejected electron is defined by the

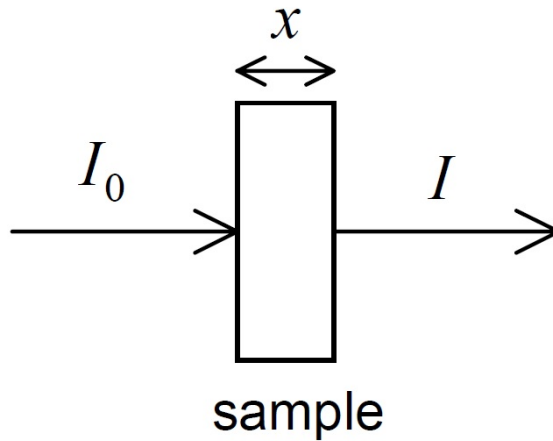


Figure 3.8: X-rays absorption within a material.

binding energy. The energy of an absorption edge for an individual element can be approximated using

$$E_k \sim Z(Z - 1) \times 13.6eV \tag{3.6}$$

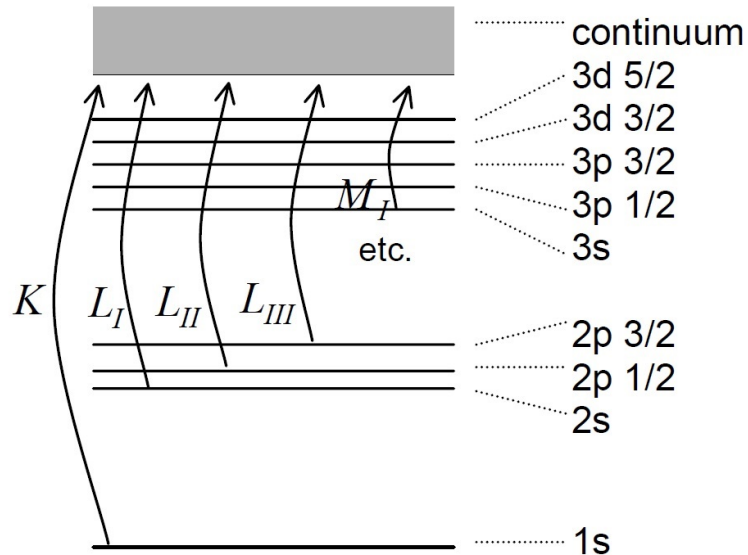


Figure 3.9: Transitions of electronic states within an atom.

The second factor is reduced to  $(Z - 1)$  in order to approximate the shielding of the nuclear charge by a second  $s$ -electron. The simple X-ray absorption measurement



involves the measurement of only the incident and transmitted X-ray intensities and is called transmission mode. However, in transmission mode, the signal intensity depends on the sample thickness and density, which defines the absorption and therefore limits the obtained signal in transmission mode. Moreover, if the absorption edges are energetically too close for two different elements within a single material, such a geometry fails to resolve edges of both elements. In order to avoid this kind of limitation, fluorescence mode should be used. In the fluorescence geometry, the X-rays intensity which are emitted from the material, is proportional to the X-ray absorption cross-section. In this geometry, the sample emits a large spectrum of X-rays, and so the fluorescence detector should be energy resolving. If the detector is energy resolved, the region of interest can be specified and by doing necessary adjustments, i.e. limiting energy/channel ratio, tuning the incident beam to optimize the signal, etc., the highest fluorescence intensity can be achieved. The X-ray absorption spectrum is divided into two different regions depending on the X-ray energy, as shown in figure 3.10. The X-ray absorption near edge spectrum

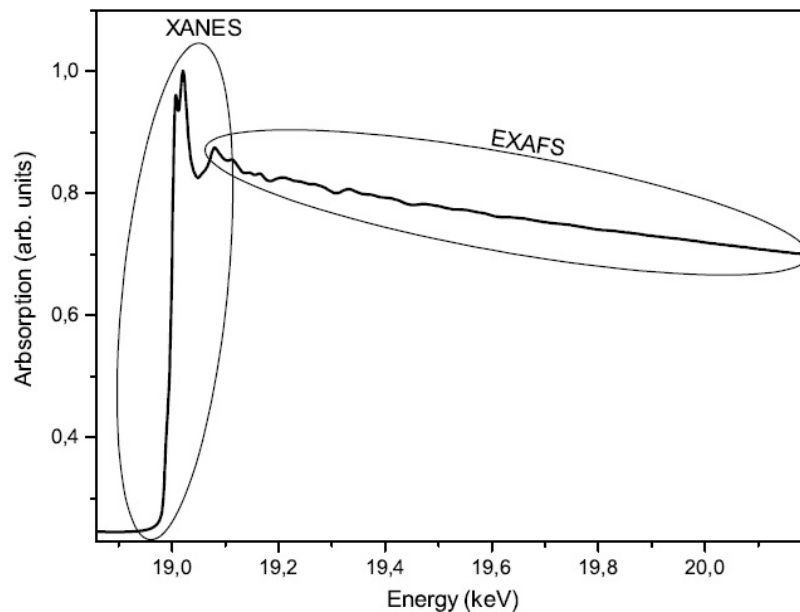


Figure 3.10: An example of a Nb K-edge X-ray absorption spectrum. The low energy region, which covers the edge jump, is considered as X-ray absorption near edge spectrum (XANES) region, while the high energy region is considered as the extended X-ray absorption fine structure spectrum (EXAFS) [88].

(XANES) for the K-edge transitions, which will be the focus for the further discussions

within this thesis, yields two important parts. The first part involves the region before the edge jump, which is called pre-edge region. In this region, usually materials reveal a fine structure, which is strongly influenced by the local surrounding environment of the atoms. The second part consists of the edge jump and some further fine features, which is usually up to 60-80 eV above the main edge. The shape and the position of the pre-edge features, as well as the edge jump, are strongly affected by the local environment of the probed atom. Thus, XANES yields information about the electronic structure and local coordination of the probed atom [89]. Considering these two regions within the XANES spectrum, two important interpretations can be made: (I) the pre-edge region is usually sensitive to coordination symmetry, i.e. by using the shape and the position of a pre-edge feature, an octahedral oxygen configuration around cobalt atoms can be distinguished from a tetrahedral configuration [90]; (II) the energy position of the edge jump gives direct information about the oxidation state of the probed atom. Moreover, the shape and the amplitude of the edge jump, where the most intense resonance occurs due to the transition from 1s shell to an unoccupied state, also carries information on the symmetry of the local atomic environment [88].

### 3.3 SQUID magnetometry

A superconducting quantum interference device (SQUID) is one of the most sensitive volume magnetometers available. A SQUID magnetometer uses the Josephson effect to measure very small variations in magnetic flux [91, 92], which is induced by a magnetic material. A SQUID usually consists of a superconductor, which is implemented with one or more Josephson junctions (Figure 3.11). SQUID magnetometers can measure down to  $10^{-9}$  emu.

In a dc SQUID (fig. 3.11), a bias current ( $I_b$ ) is applied to the superconducting loop. Shunt resistors are used in order to avoid hysteretic behavior of the I-V curve [93]. If a magnetic flux is introduced (e.g. magnetic material to be measured) to such a loop, it induces screening currents, which leads to a change in the critical current  $I_c$  of the Josephson junction. If  $I_b$  is slightly larger than  $I_c$ , there will be voltage change across the Josephson junction. Moreover, as the magnetic flux changes, the voltage change becomes

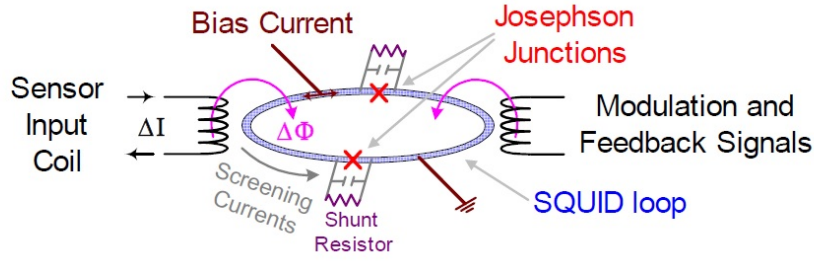


Figure 3.11: Dual junction (dc) SQUID loop. The capacitor represents the self-capacitance of the junction [91].

periodical, and this period is coupled to the period of the magnetic flux quantum. By monitoring the change in the voltage, the SQUID makes it possible to determine the magnitude of the applied magnetic flux [94].

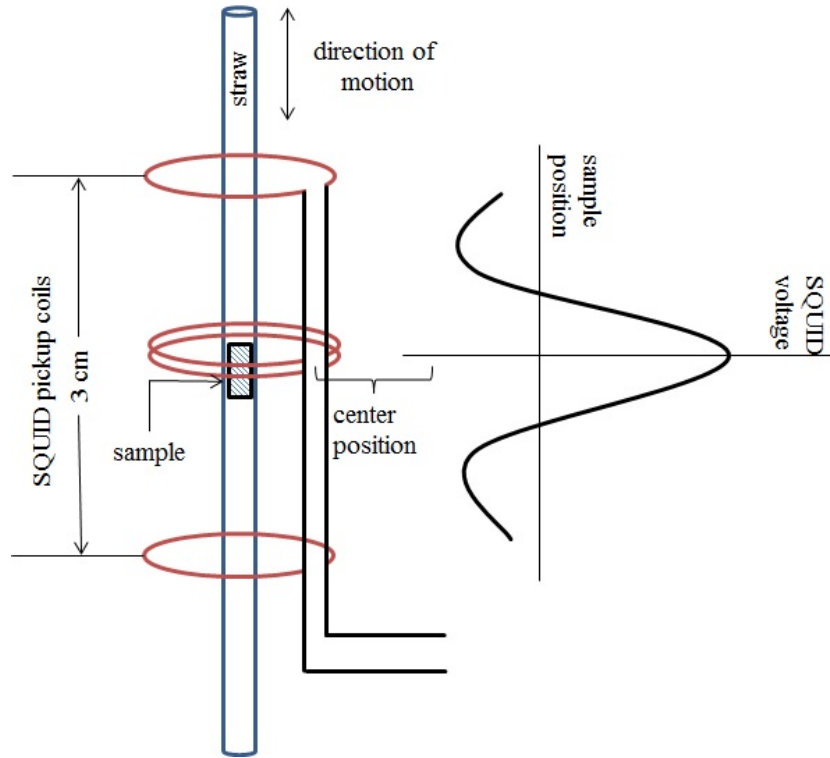


Figure 3.12: The configuration of SQUID magnetometer in a MPMS setup.

In this thesis a magnetic properties measurement system (MPMS) XL 7, from Quantum Design is employed for all of the SQUID magnetometry measurements. In the MPMS, a gradiometer configuration is used (Fig. 3.12), which consists of two SQUID coils. In order to induce a magnetic flux in SQUID coils, the sample, which is mounted in a straw, is moved along the symmetry axis through coils. In the MPMS setup, three

distinct measurement modes are available, namely DC, RSO and VSM. In DC mode, sample moves linearly (a DC motion) along the symmetry axis. This method provides large scan ranges up to 8 cm. Similar to DC mode, the RSO (reciprocating sample option) mode, moves the sample linearly along the measurement axis. In addition to the linear displacement, this motor induces a periodical vibration, which has a frequency range between 0.5 Hz to 4 Hz, resulting in an oscillating AC signal combined with a DC signal. The VSM (vibrating sample magnetometer) mode induces oscillations around the measurement center. In the VSM method the amplitude of the movement limits the sample size, while the scan range is few millimeters. In all of the three measurement methods, sample positioning with respect to the center of the two SQUID loops is the key component to obtain precise magnetization data.

Sample size and positioning are the most important things to control or to avoid the measurement errors in SQUID magnetometry. In this study, magnetometry measurements were performed by using  $8 \times 4 \text{ mm}^2$  samples, therefore the best magnetic resolution was achieved by employing RSO method. In this thesis all of the presented magnetometry results were mostly obtained by using RSO-MPMS SQUID magnetometry.

### **3.3.1 Avoiding magnetic contamination**

Magnetic contamination, as already explained in section 2.2.6, can give rise to an unwanted ferromagnetic signal. A touch of stainless steel, small piece of an iron dust (which might be a residual piece from the previous experiment), a contaminated target, to name a few, the list of possible magnetic contamination sources can be expanded further. However, prevention from it just needs more care during sample handling. In this thesis, following steps were followed in order to avoid magnetic contamination;

- (i) Use of ceramic and plastic tweezers, which are dedicated to this study only,
  
- (ii) Before film deposition, the magnetic response of the substrates is checked and verified to be diamagnetic,

(iii) replacement of all the magnetic parts of the sputter chamber with their non-magnetic equivalents,

(iv) checking all of the target composition and their products (i.e. thin films) by using particle induced X-ray emission spectroscopy measurements, which is highly sensitive to Fe, Ni and Co concentrations down to 30 ppm level,

(v) after growing a test sample using all equipments (e.g. non-magnetic parts of deposition chamber, magnetically clean substrates, contamination free target, etc.) another magnetic response test was done by SQUID magnetometer and results revealed that the achieved samples were not ferromagnetic,

(vi) deposition of twin samples, one of which is used for structural characterizations, while the other one was used only for magnetic measurements. In order to be sure about the same properties of each twins, cross-checks were performed by employing same characterization methods continuously.

### **3.4 Positron annihilation spectroscopy**

Positron annihilation spectroscopy (PAS) is a measurement method, which probes the local electron density and atomic structure of a material by the electrostatic interactions of positrons with their surroundings within a sample. Therefore, PAS measurements make it possible to probe local nano-structures embedded in bulk/thin film bodies, open-volume defects (vacancies), uncontrolled cluster formations of doped atoms, etc., namely, all kind of structures, where electron density differs significantly from the average electron density [95]. There are two ways to gain information from positron annihilation measurements, either positron-electron interaction is measured in time or in energy domain. Time dependent measurements (life-time measurements) usually are subjected to identify the type and fraction of probed defects, while the energy dependent measurements give an in-

formation on the depth and the relative amount of such defects (e.g. increase or decrease in the open-volume defect fraction). In a periodic lattice, ground state of a thermalized positrons can be described by a single particle Schrödinger equation [96]

$$-\frac{1}{2m^*} \nabla^2 \psi + (\mathbf{r}) + V(\mathbf{r})\psi + (\mathbf{r}) = E + \psi + (\mathbf{r}), \quad (3.7)$$

where,  $\psi$  is the wave function and  $m^*$  is the effective mass of the positron. The positron annihilation rate ( $\lambda$ ) inside a solid, which has also an inverse relation with the positron lifetime  $\tau$ , is proportional to the overlapping of the electron and positron densities and can be expressed as

$$\frac{1}{\tau} = \lambda = \pi r_e^2 c \int |\psi + (\mathbf{r})|^2 n - (\mathbf{r}) d\mathbf{r}, \quad (3.8)$$

Where  $r_e^2$  is the classical electron radius,  $c$  is the light velocity and  $n - (\mathbf{r})$  is the local electron density. Therefore the momentum distribution  $\rho(\mathbf{p})$  of the annihilation process, which depends on the surrounding electrons wave functions  $\psi_i$  over normalized volume  $V$  can be generally written in;

$$\rho(\mathbf{p}) = \frac{\pi r_e^2 c}{V} \sum_i \left| \int e^{-i\mathbf{p}\cdot\mathbf{r}} \psi + (\mathbf{r}) \psi_i(\mathbf{r}) d\mathbf{r} \right|^2, \quad (3.9)$$

Similar to free charge carriers in semiconductors, positrons have localized states in the vicinity of the lattice defects. Due to different electron density at around a defect site, a positron sees an open-volume defect as a potential well, which results in a localized positron states, thus a change in the lifetime of the positron [97]. Referring to eq. 3.9, due to electron density change at vacancy type defects, the momentum distribution change can be measured by Doppler broadening measurements, where two photons are emitted with energies at around 511 keV, as a product of the electron-positron annihilation.

The experimental concept of the Doppler broadening measurement requires a radioactive slow positron source, which was  $^{22}\text{Na}$  for this thesis, an accelerator, which sets up the sent positron energies and a Ge detector, which is employed in order probe the photons. The radioactive source produces the positrons and by changing positron energy, as in the case of ion implantation, a depth information within a material can be resolved.

The photon detector, which is made out of a high purity Ge, detects the photons, that are the product of positron-electron annihilation process. The motion of the annihilating electron-positron pair leads to a Doppler shift in the energies of photon radiation originating from the annihilation and can be expressed as

$$\Delta E = \frac{cpL}{2}, \quad (3.10)$$

where the momentum distribution is

$$\rho(pL) = \int \int dp_x dp_y \rho(\mathbf{p}). \quad (3.11)$$

The  $pL$  term is the longitudinal momentum distribution component of the annihilation. The electron momentum distribution  $\rho(\mathbf{p})$  leads to a broadening of the 511 keV annihilation line. The shape of the emitted photon energy distribution around 511 keV gives the one dimensional momentum distribution of the electron-positron annihilation. As a measure of the momentum shift, so called  $S$  parameter is extracted from energy distribution of the emitted photon energy distribution (Fig 3.13).

The  $S$  parameter is the ratio of the area below 511 keV peak within 1 keV range over whole peak area ( $S = A_s/A$ ). As shown in figure 3.13, open-volume defects lead to an increase of  $S$  parameter. In short the higher the  $S$  parameter the larger is the fraction of the open-volume defects inside the probed material. In this thesis, the slow positron system of Rossendorf [99] is employed for the Doppler broadening measurements. The energy of the implanted positrons varied from 28 eV to 36 keV, while a Ge detector is employed to probe annihilation products, and the energy resolution of the detector at the annihilation line is  $1.09 \pm 0.01$  keV

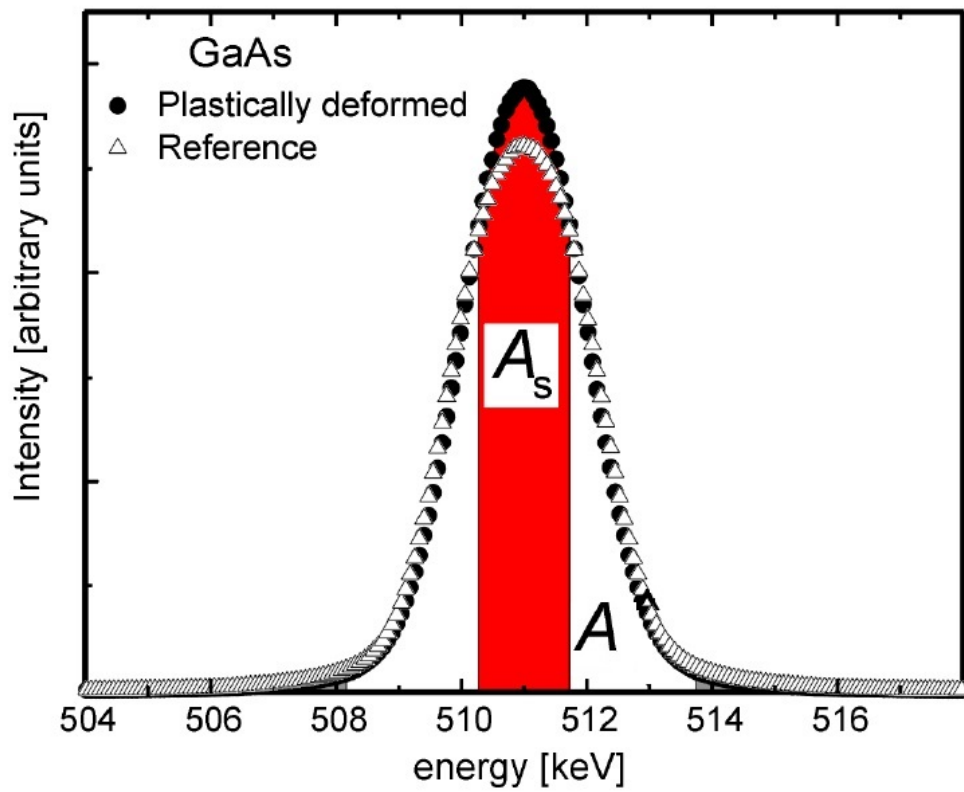


Figure 3.13: The energy distribution of the emitted photons from electron-positron annihilation within a deformed and non-deformed GaAs. [98]





---

## TM Implantation into Different TiO<sub>2</sub> Structures (TM = Co, Mn, V)

---

In chapter 4, in order to investigate the physical properties, a systematic approach has been applied to transition metal implanted TiO<sub>2</sub> films with different microstructures. Therefore, for this chapter the main experiments were performed by applying a set of common experiments, which are given in section 4.1. Apart from the common experiments, subsection specific experiments are introduced in the experiments parts before each subsection or section starts.

### 4.1 Experiments

For this chapter (4), TiO<sub>2</sub> films of 300 nm thickness were grown on SrTiO<sub>3</sub> (100) single crystals by means of DC magnetron sputtering. A high purity oxygen deficient ceramic TiO<sub>2-x</sub> target was sputtered at 120 W in Ar/O<sub>2</sub> atmosphere at a pressure of 0.7 Pa containing ~0.4 vol.% of O<sub>2</sub>. These conditions were found to yield near-stoichiometric films. Amorphous TiO<sub>2</sub> films were obtained by deposition on unheated substrates. Polycrystalline anatase TiO<sub>2</sub> structure was achieved by post-growth annealing of initially amorphous layers at 450 °C for 1 hour in vacuum (< 2.10<sup>-5</sup> Pa). Epitaxial anatase TiO<sub>2</sub>,

on the other hand, was obtained by direct deposition on heated substrates. Schematic illustration for different microstructures of as-grown  $\text{TiO}_2$  films are given in figure 4.1. For a homogeneous depth distribution of the TM ions within a layer about 150 nm thickness, five different energy and ion fluence combinations, as determined by SRIM simulations [100], have been applied. The crystalline structure of both as-grown and implanted  $\text{TiO}_2$  films was controlled by means of X-ray diffraction (XRD) measurements using Ni-filtered  $\text{Cu-K}\alpha$  radiation of a PANalytical Empyrean diffractometer. The local atomic coordination of the implanted TM atoms was investigated by X-ray absorption near-edge spectroscopy (XANES) at dopants' K-edge in energy-resolved fluorescence mode using the ROBL-MRH setup of the BM-20 beamline at the ESRF in Grenoble (France). All of the structural characterizations were performed at room temperature. Magnetic properties of the implanted films were investigated by a superconducting interference device (SQUID, Quantum Design MPMS XL 7). Magnetometry was performed as functions of temperature and magnetic field. For all samples, zero field cooled (ZFC) and field cooled (FC) thermomagnetic measurements have been carried out in an applied external magnetic field of 15 mT.

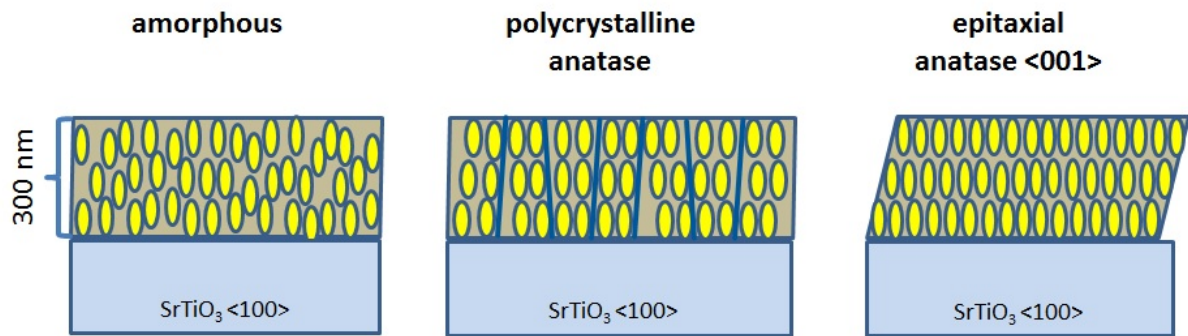


Figure 4.1: Schematic of different microstructures of the as-grown films

## 4.2 Co<sup>+</sup> implantation: from diluted paramagnetism to superparamagnetic clusters

This section (4.2) is divided into two main studies as subsections. In the first subsection (4.2.1), the effect of the microstructure on the magnetic and the structural properties of Co<sup>+</sup>-implanted TiO<sub>2</sub> at 4 at.% doping concentration is investigated. In the second subsection (4.2.2), investigation is done at 5 at.% dopant concentration, at which concentration superparamagnetic clustering starts. Therefore, in the second study, investigation focuses on the determination of the effect of the initial microstructure on dopant-host coordination and the magnetic properties of Co<sup>+</sup>-implanted TiO<sub>2</sub> thin films by considering superparamagnetic clusters as well.

### 4.2.1 Cluster-free Co<sup>+</sup>-implanted TiO<sub>2</sub> thin films

Here, the high impact of the initial crystal structures of pristine TiO<sub>2</sub> thin films, on the resulting magnetic and defect properties after 4 at.% cobalt implantation is presented.

#### 4.2.1.1 Experiments

Only for this section (4.2.1), for the epitaxial anatase films, two different substrate temperature were applied during deposition. Namely, the substrates were kept at 400 °C or 500 °C in order to achieve different qualities of epitaxial relation between the substrate and the film, and no post-annealing was performed. Correspondingly, epitaxial films are named after their rocking-curve (RC) full width at half maximum (FWHM) values, which gives an information on the degree of the epitaxial relation between the film and the substrate, and implantation angles. Moreover, 4 at.% Co<sup>+</sup>- implanted polycrystalline and amorphous films were labeled as Poly-0 and Amorph-0, in order to have a better comparability. A comprehensive outlook on sample properties and labeling can be found in table 4.1 and 4.2. The calculated 4 at.% cobalt implantation depth profiles are given in figure 4.2.

Table 4.1: Sample labeling of as-grown  $\text{TiO}_2$  films.  $T_{\text{substrate}}$  stands for the substrate temperature during growth, while  $T_{\text{annealing}}$  represents in-situ post deposition annealing temperature for 1 hour and performed only for polycrystalline structures. The epitaxial films are labeled after their epitaxial quality, which is altered by applying different substrate temperatures. The qualities were determined from RC measurement and the epitaxial sample which showed narrower RC curve has labeled as high quality (HQ-Epitaxial), while the epitaxial film with broader RC curve has labeled as standard quality (SQ-Epitaxial) (see section 4.2.1.2)

microstructure	$T_{\text{substrate}}$	$T_{\text{annealing}}$	label
amorphous	-	-	Amorph
polycrystalline	-	450	Poly
epitaxial	400	-	SQ-Epitaxial
epitaxial	500	-	HQ-Epitaxial

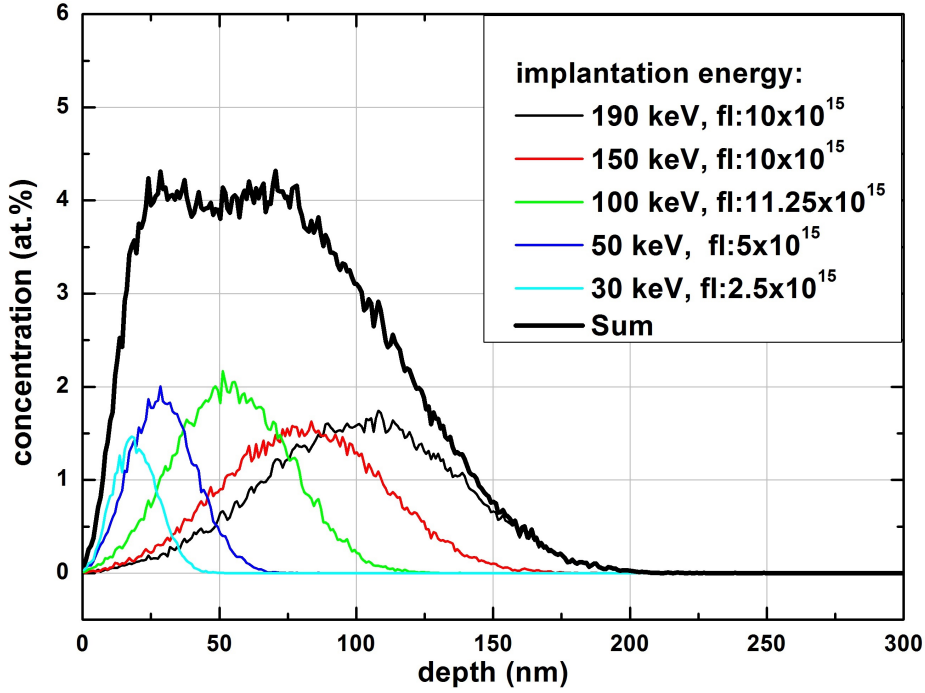


Figure 4.2: Calculated depth profile of the implanted 4 at.%  $\text{Co}^+$  depth distribution after implantation into a 300nm thick  $\text{TiO}_2$ . Implantation energies and corresponding fluences (fl) are indicated.

#### 4.2.1.2 Structural properties

In the XRD pattern of as-grown polycrystalline and epitaxial films, only anatase related reflections were observed (Fig. 4.3). Moreover,  $\omega$  scans of the epitaxial films or the

so-called rocking-curve measurements, indicate FWHM values of  $2.6^\circ$  and  $0.9^\circ$  for  $400^\circ\text{C}$  and  $500^\circ\text{C}$  grown epitaxial films, respectively. The relatively high values of RC FWHM for epitaxial films comparing to previously reported data for pulsed laser deposition grown [57] and oxygen plasma assisted molecular beam epitaxy [101] grown anatase  $\text{TiO}_2$  films, can be attributed to the relatively larger thicknesses and faster growth rate of sputtering. After 4 at.%  $\text{Co}^+$  implantation, all of the polycrystalline and the epitaxial films remained mostly in anatase phase with a small amount of rutile (111) phases and no Co related secondary phases were observed within the XRD measurements sensitivity range.

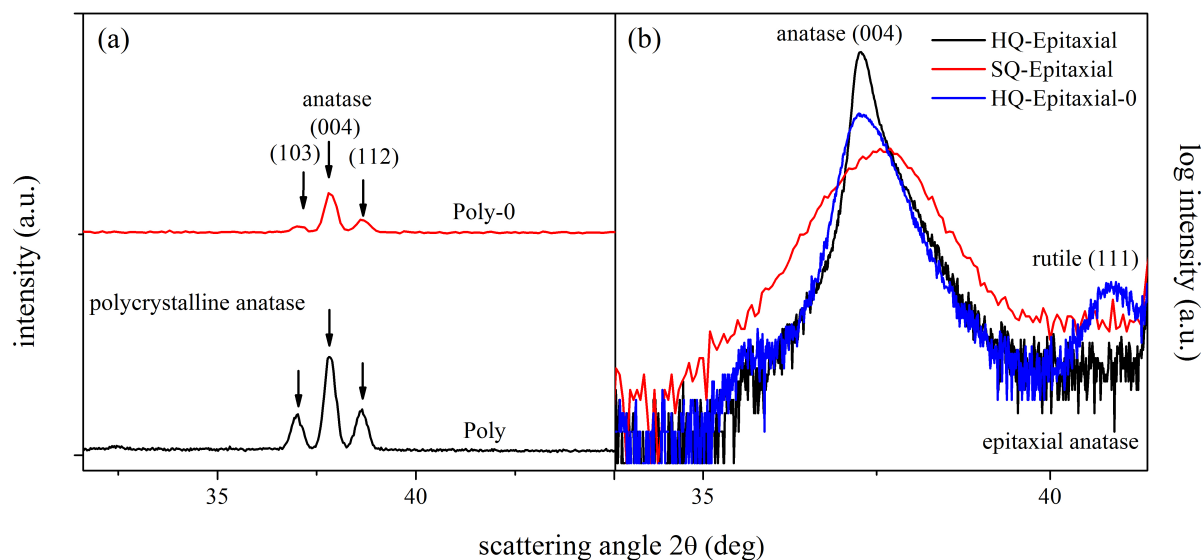


Figure 4.3: XRD pattern of as-grown and 4 at.%  $\text{Co}^+$   $\text{TiO}_2$ : a) polycrystalline film in  $1^\circ$  grazing incidence, and b) epitaxial film in aligned symmetric  $2\theta$ - $\omega$  geometry.

#### 4.2.1.3 Implantation-induced structural defects

Defect properties of the as-grown and the 4 at.%  $\text{Co}^+$ -implanted films were characterized by PAS measurements. A depth profile of the open volume defect concentration throughout the sample, is obtained by implanting positrons with different kinetic energies (see chapter 3). The data shown provides some depth information, because the positron energy defines the depth of implantation of positrons into the sample, which is then followed by diffusion until annihilation takes place. In order to understand PAS results more clearly, S parameter plots were divided into three regions. (I) represents film surface-(low energy) positron interactions. Since the film surface acts as a positron sink, due to surface

defects, the S parameter is high at lowest positron energies; (II) shows film body-(medium energy) positron interactions. Positrons, implanted at higher energies, remain in the bulk of the film, resulting in a plateau of the S parameter that provides information about defect concentration within the film. Most of the further discussions on PAS results of the films are focused on this region; (III) represents interface/substrate-(high energy) positron interaction with higher energetic positrons. PAS results on the as-grown films revealed that the different microstructures lead to different defect concentrations (Fig. 4.4a). The SQ-Epitaxial film showed lower defect concentration with lower S parameters as compared to the amorphous and polycrystalline films. Furthermore, an increase in the crystalline quality for the epitaxial films, i.e from standard quality to high quality, revealed a defect concentration decrease accompanied by lower S parameters for as-grown films.

PAS results of the  $\text{Co}^+$ -implanted  $\text{TiO}_2$  films are given in figure 4.4 (b) and (d). After 4 at.%  $\text{Co}^+$  implantation the amorphous film showed negligible difference in S parameter at film region. This is due to a large amount defect concentration within the as-grown structure and this amount is already sufficient to saturate the detector. The polycrystalline film, as expected after implantation, showed slightly higher defect concentration as compared to its as-grown state. However, after  $\text{Co}^+$  implantation, both SQ-Epitaxial-0 and HQ-Epitaxial-10 films showed lower defect concentration between 1.5 keV and 2.5 keV energy region as compared to their as-grown states. There can be two possible scenarios to explain this behavior; (I) this tendency to lower S-parameters after  $\text{Co}^+$  implantation can be attributed to possible ion channeling effects. In other words, when an implanted ion enters a crystalline solid, nuclear interactions between the implanted atom and the host lattice atoms start along the ion trajectories. If the ion enters into an amorphous substance, stopping of the implanted ion will be strong, due to random orientation of host matrix atoms. However, if the host substance has long range crystalline orientation (i.e. an epitaxial structure) and if the ion enters into the target material with a low-index, i.e  $0^\circ$  incidence with respect to the crystalline plane normal, the trajectory of the implanted ion will be longer as compared to the trajectory of an ion in a randomly oriented host, due to long free spaces between crystalline planes. This well-known phenomenon is called ion channeling [102]. For a polycrystalline film, crystalline planes, in which implanted

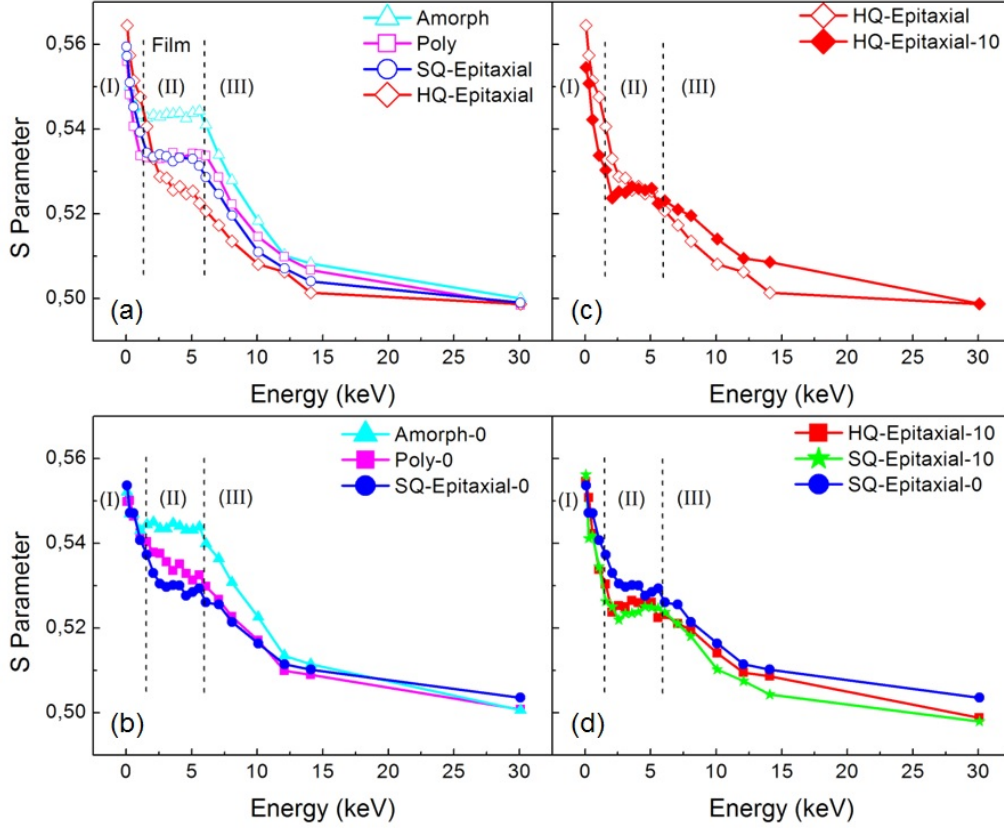


Figure 4.4: Measured positron-energy dependent S parameters for (a) as grown TiO<sub>2</sub> films with different microstructures and (b-d) after Co<sup>+</sup> implantation. (c) shows a direct comparison of the energy-dependent S-parameter for the epitaxial films, i.e. HQ-Epitaxial and HQ-Epitaxial-10, before and after Co<sup>+</sup> implantation

ion can travel freely, are limited to next grain boundary. Therefore in amorphous and polycrystalline structures, the implanted ion interacts with more host atoms and creates more defects. On the other hand in the epitaxial film implanted ion can travel freely without losing most of its energy until interacting with an obstacle [103]. In epitaxial films these obstacles can be lattice defects (e.g. vacancies, point defects, etc.), and as shown in figure 4.4 (c-d) after implantation, a drop in the defect concentration for the epitaxial films, can indicate trapping of implanted Co ions by open volume defects. By changing implantation incidence we tried to eliminate such channeling effects. However, the only difference we could achieve is to decrease stopping range by increasing the probability of interactions between the surface atoms of the film and implanted ions. But this does not



mean that no channeling occurs, because after surface interaction, implanted ions can still find a crystalline plane track to channel along with lower energy. (II) The second scenario can be, if the defect concentration in the film, especially around the surface, is too low, the positrons can diffuse a longer way (e.g. towards the surface) before they annihilate. This would result in a higher S Parameter at lower positron energies. In the case of the as-grown epitaxial film there is no clear plateau, which may be attributed to low defect concentration. The lower defect concentration can lead positrons diffuse very quickly to surface and this result in a larger Doppler broadening, in turn larger S parameter values. Since both of the scenarios have probabilities, the further discussion will mainly focus on comparing different microstructures.

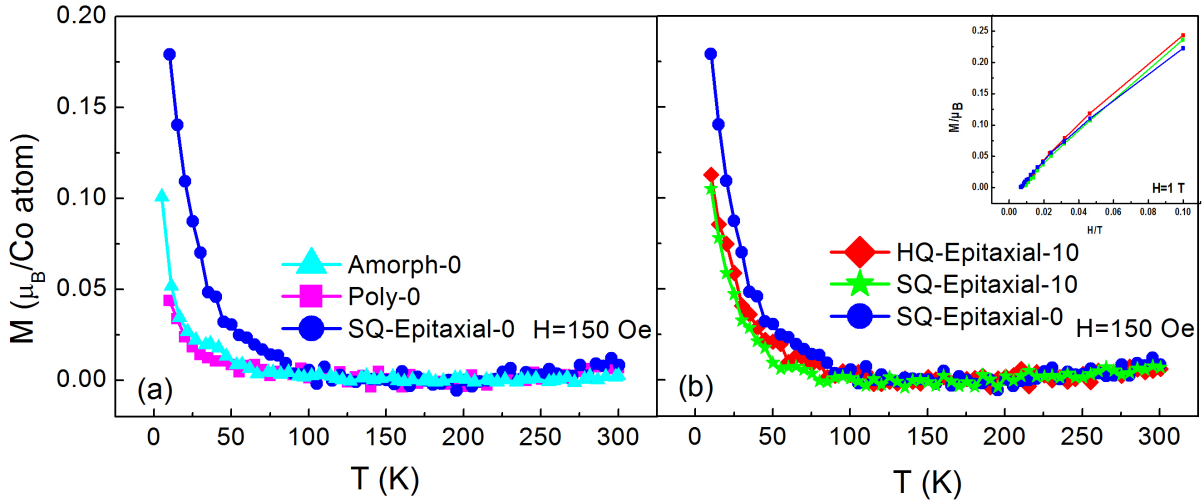


Figure 4.5: Field dependent magnetization curves of 4 at.%  $\text{Co}^+$ -implanted  $\text{TiO}_2$  films of (a) of different microstructures and (b) different qualities of epitaxial films. Inset shows the Brillouin function fits.

#### 4.2.1.4 Magnetic properties

Magnetometry measurements were carried out as a temperature function of magnetization. As a good proof of magnetic contamination free sample handling before and after  $\text{Co}^+$  implantation, none of the samples exhibited ferromagnetic properties. The exposure to  $\text{Co}^+$  ions, resulted in a strong paramagnetic response for all films. As depicted in figure 4.5, paramagnetic response strongly depends on the host films microstructure. To understand the origin of paramagnetic properties, temperature dependent magnetization curves are fitted by a Brillouin function  $M = Ng\mu_B B_J B_J(x)$ , where  $x = g\mu_B JH/k_B T$ ,  $g$

is the  $g$ -factor,  $J$  the angular momentum number,  $N$  the number of spins and  $k_B$  the Boltzmann constant. The Brillouin function provides good fit for  $J = S = 3/2$  which is consistent with the results presented by Sangaletti et. al. [104]. It is found that the calculated  $N$  values, which shows number of ions contributing paramagnetic properties, depends both structure and implantation angle (see table 4.2). As shown in figure 4.5 and table 4.2, SQ-Epitaxial-0 film showed the highest paramagnetic response and this response decreases with decreasing the order of crystalline orientation (fig 4.5a). Additionally, by changing the incidence angle of the implantation, paramagnetic response also decreases (fig 4.5b). On the other hand crystalline quality has no dramatic effect on magnetic properties under same implantation conditions, i.e see table 4.2 and figure 4.5 for the paramagnetic response of SQ-Epitaxial-10 and HQ-Epitaxial-10.

Table 4.2: Preparation parameters and magnetic properties of the 4 at.% Co<sup>+</sup> implanted TiO<sub>2</sub> films.  $T_{substrate}$  shows the substrate temperature during growth, while  $T_{postannealing}$  represents in-situ post deposition treatments.  $RC\ FWHM$  values for epitaxial structures are given.  $N$  is the total number of paramagnetic Co<sup>+2</sup> ions, which are extracted from fit values. Effective Co ions shows the effective number of Co ions compared to whole implantation concentration (*un* stands for unheated).

	Sample name	$T_{substrate}$ (K)	$T_{postannealing}$ (1h)	$RC\ FWHM$ (°)	Implantation concentration (at.%)	Implantation angle ( $\alpha$ )	$N$ (cm <sup>-3</sup> )	Effective Co ions (%)
Virgin Films	Amorph	un	-	-	4	-		
	Poly	un	450	-	4	-		
	SQ-Epitaxial	400	-	2.6	4	-		
	HQ-Epitaxial	500	-	0.9	4	-		
Co implanted Films	Amorph-0	un	-	-	4	0	$6,11 \times 10^{20}$	17,9
	Poly-0	un	450	-	4	0	$5,15 \times 10^{20}$	15,1
	SQ-Epitaxial-0	400	-	2.7	4	0	$2,10 \times 10^{21}$	61,7
	SQ-Epitaxial-10	400	-	2.7	4	10	$1,13 \times 10^{21}$	33,2
	HQ-Epitaxial-10	500	-	1.3	4	10	$1,34 \times 10^{21}$	39,4

#### 4.2.1.5 Local environment of implanted Co atoms

XANES measurements were carried out at the Co-K edge to investigate the local environment of implanted Co<sup>+</sup> ions. XANES spectra for different structures of Co<sup>+</sup>-implanted TiO<sub>2</sub> films are shown in figure 4.6. Overall, the spectra shapes for the polycrystalline and epitaxial films are similar and in good agreement with CoTiO<sub>3</sub> spectrum. The main difference in the local environment of Co (II) in CoO and CoTiO<sub>3</sub> is in the oxygen coordination. The oxygen coordination of Co atoms is undistorted and distorted octahedral in CoO and CoTiO<sub>3</sub>, respectively [105]. Moreover, Ti in both anatase and rutile TiO<sub>2</sub> also

shows distorted octahedral oxygen coordination [106]. The similarity of the measured Co-K edges of Co<sup>+</sup>-implanted TiO<sub>2</sub> to that of CoTiO<sub>3</sub> indicates a distorted octahedral oxygen coordination for both the epitaxial and polycrystalline structures. Thus, the observed Co-K edge spectra are assigned to substitutional Co<sub>Ti</sub> in the TiO<sub>2</sub> lattice, which is in agreement with previous reports [107, 108]. On the other hand, differences between each individual XANES spectra can be seen in the lower energy region, namely pre-peak region. The Co-K edge for amorphous film shows a small feature between 7712 eV and 7717 eV while for polycrystalline and both epitaxial films, the pre-peak feature becomes step-like (see figure 4.6 a inset). This small feature occurs due to a 1s-3d pre-edge resonance which becomes partially dipole allowed, because of the Co coordination with O ligands and Co 3d-O 2p mixing in low-lying conduction band states [32]. This feature, therefore, strictly depends on oxygen coordination of the probed TM atom. The difference at pre-peak region shows that even though oxidation state of the Co atoms within different structures are mostly in +2 state, they have different chemical coordination within different structures.

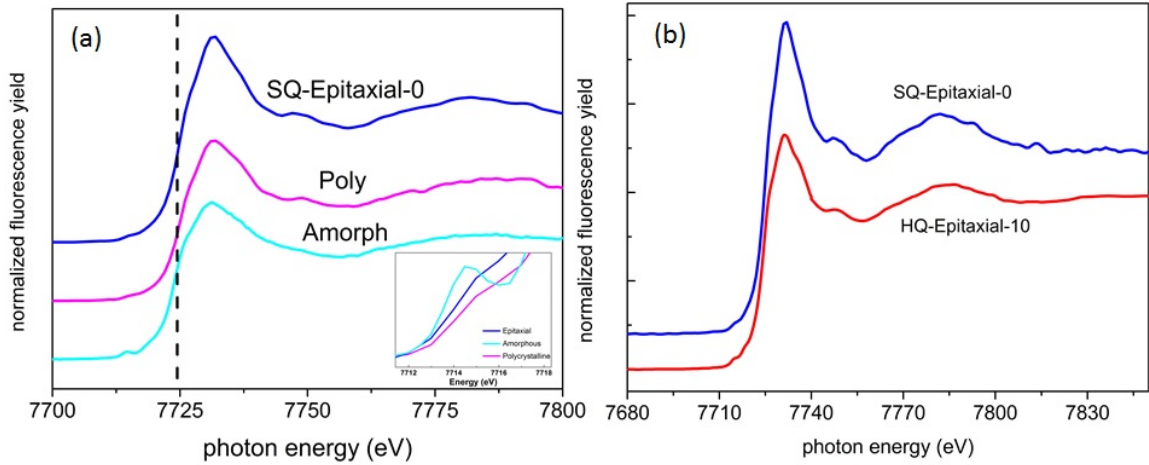


Figure 4.6: Co K-edge XANES spectra for (a) different structures of 4 at.% Co<sup>+</sup>-implanted TiO<sub>2</sub> films, (b) different qualities of 4 at.% Co<sup>+</sup>-implanted epitaxial TiO<sub>2</sub> films

#### 4.2.1.6 Summary

In summary, we have implanted different structures of TiO<sub>2</sub> films with 4 at.% cobalt ions. All of the samples, independent from their microstructure type and quality, exhibited paramagnetic properties. We have found that the as-grown microstructure affects

the observed paramagnetic properties. The highest paramagnetic response was found for 4 at.% Co<sup>+</sup>-implanted epitaxial films. From the XANES results, the existence of the Co<sup>+2</sup> ions is confirmed. Taking into account all of the structural and magnetic characterization results, we have found a strong structure type dependency on paramagnetic properties. Higher order in crystalline structure results in more Co<sup>+2</sup> phases and less open volume defects after implantation and more pronounced paramagnetic properties.

## 4.2.2 Revealing nano-clusters within Co<sup>+</sup>-implanted TiO<sub>2</sub> thin films

### 4.2.2.1 Experiments

For this subsection (4.2.2), 5 at.% cobalt ion-implantation was performed as a sequence of five different ion energy and fluence combinations that were determined by SRIM [100] simulations and given in figure 4.7. As a supporting information to XANES measurements, magneto-optic transversal Kerr effect spectroscopy were performed in order to investigate local atomic coordination of the dopant. The spectra were collected in the transversal Kerr effect (TKE) geometry using the dynamic method in the energy range from 0.5 to 3.5 eV with applied external magnetic field of 3.0 kOe. Furthermore, transmission electron microscopy (TEM) was performed using an image-corrected Titan 80-300 microscope (FEI) operated at 300 kV accelerating voltage.

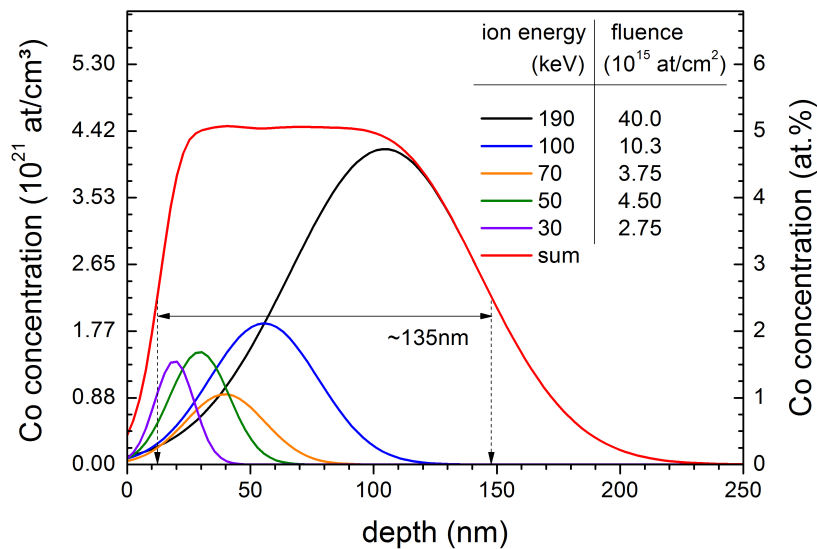


Figure 4.7: Depth profiles of Co<sup>+</sup>-implanted into TiO<sub>2</sub> calculated by SRIM. Five different energy fluence combinations have been used to achieve a box like sum profile.

### 4.2.2.2 Structural properties

XRD spectra of as-grown polycrystalline and epitaxial films reveal that both are single phase anatase (Fig. 4.8). Moreover, for the epitaxial film, only 00*l* reflections (*l*=4,8)

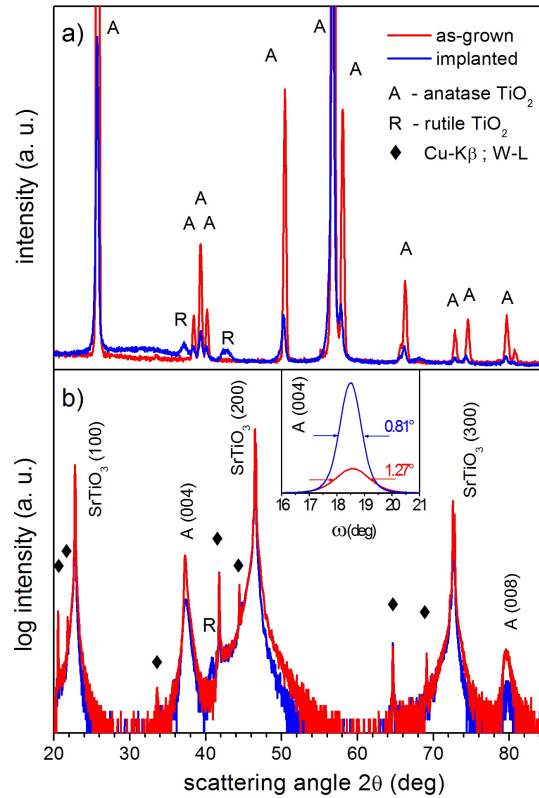


Figure 4.8: XRD pattern of as-grown and  $\text{Co}^+$ -implanted  $\text{TiO}_2$ : a) polycrystalline film in  $1^\circ$  grazing incidence, and b) epitaxial film in aligned symmetric  $2\theta$ - $\omega$  geometry. The inset in b) shows the anatase  $\text{TiO}_2$  (004) rocking curves of the epitaxial film.

are observed. Rocking-curve measurements at the anatase (004) reflection indicate a FWHM of  $0.81^\circ$  for the as-grown epitaxial film, confirming out-of plane c-axis texture i.e.  $\text{TiO}_2(001)\parallel\text{STO}(100)$ . Furthermore, single domain  $\text{TiO}_2(100)\parallel\text{STO}(001)$  in-plane order was observed during rotational scans (not shown). After  $\text{Co}^+$  implantation, both polycrystalline and epitaxial films remained mostly in the anatase phase. However, ion implantation decreased the structural quality, which is observed as lowered anatase peak intensities and increased anatase (004) RC FWHM in case of the epitaxial film (inset in Fig. 4.8). Furthermore, it is found that  $\text{Co}^+$  implantation induces the formation of rutile  $\text{TiO}_2$  crystallites in all three as-grown structures. A rough estimation on the amount of the ion implantation induced rutile phases can be made by comparing the peak areas of

the anatase and rutile reflections. The rutile-to-anatase ratio was estimated to be around 6% for the Co:TiO<sub>2</sub> polycrystalline film, whereas for the Co:TiO<sub>2</sub> epitaxial film the estimation yielded 0.2% rutile-to-anatase ratio. Furthermore, no other Co related secondary phases have been observed by XRD.

The anatase structure of TiO<sub>2</sub> is a metastable phase, which transforms irreversibly to rutile when a sufficient amount energy is introduced into the system [109]. Ion implantation is based on bombarding the host material by highly energetic ions, which leads to energy transfer to the host lattice. The energy, which is transferred to the host lattice is inversely proportional to the ion trajectory length [103]. Taking into account the ion channeling effect during implantation, the ion trajectory length should increase while going from polycrystalline to epitaxial microstructures. The applied tilt of the sample of 10° is not sufficient to fully suppress channeling effects, during implantation. The difference in penetration depths of the implanted Co<sup>+</sup> can also be seen in the TEM images. Accordingly, the amount of the energy transferred into the host lattice during ion implantation, is expected to be higher for the case of the polycrystalline film as compared to the epitaxial film. Thus the experimental findings regarding to the amount of the implantation-induced rutile phases are consistent with aforementioned mechanistic scenario.

Cross-sectional high-angle annular dark-field (HAADF) scanning TEM (STEM) micrographs of the 5 at.% Co<sup>+</sup>-implanted epitaxial and polycrystalline TiO<sub>2</sub> films are displayed in Fig. 4.9. Besides the SrTiO<sub>3</sub> substrate, the overview images of the Co:TiO<sub>2</sub> films in (a) and (c) show the unimplanted, as well as the Co<sup>+</sup>-implanted TiO<sub>2</sub> regions. In particular, these STEM micrographs confirm that the implantation profiles end at a depth of around 150 nm below the sample surface with some extended trajectories for both of the Co<sup>+</sup>-implanted crystalline samples. Hence, mixing at the TiO<sub>2</sub>/SrTiO<sub>3</sub> interface and possible long-range ion channeling are avoided. Moreover, clusters with an average diameter of approximately 3 nm and 2.5 nm are observed for the Co<sup>+</sup>-implanted epitaxial and polycrystalline films, respectively. (Fig. 4.9 b and d)

open volume defect properties of 5 at.% Co<sup>+</sup>-implanted TiO<sub>2</sub> thin films were investigated by means of PAS measurements and depicted in figure 4.10. As shown in the figure, the same trend for defect properties for 4 at.% Co<sup>+</sup>-implanted films, e.g. increasing de-

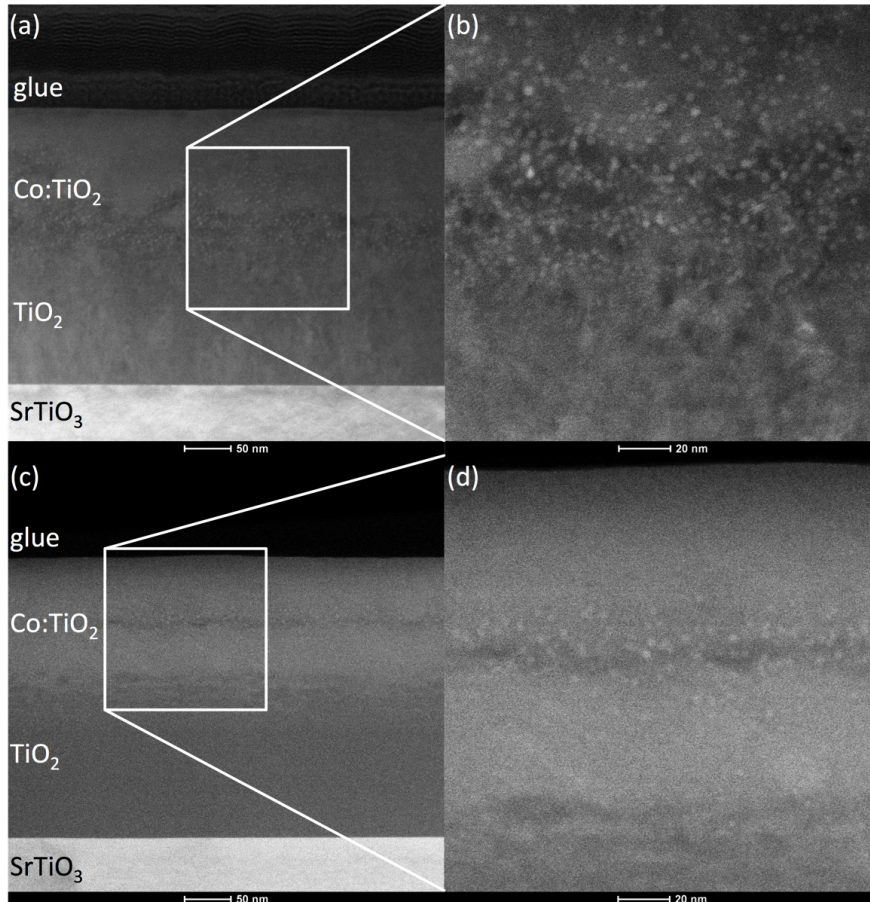


Figure 4.9: Dark field TEM image of the  $\text{Co}^+$ -implanted epitaxial  $\text{TiO}_2$  film: a) cross-section overview, b) high magnification image of the implanted area.

fect concentration for decreasing structural order, for the epitaxial  $\text{Co}:\text{TiO}_2$  amorphous film and the lowest defect concentration for the  $\text{Co}:\text{TiO}_2$ , was observed. For the 5 at.%  $\text{Co}^+$ -implanted epitaxial film similar to 4 at.%  $\text{Co}^+$ -implanted epitaxial film, a slightly lower S parameter values were found as compared to its as-grown state.

#### 4.2.2.3 Magnetic properties

SQUID magnetometry revealed the absence of room-temperature ferromagnetism for all 5 at.%  $\text{Co}^+$ -implanted films, independent on their microstructure. A higher paramagnetic response was observed for the  $\text{Co}^+$ -implanted epitaxial film as compared to the other films (fig. 4.11). The blocking temperatures ( $T_B$ ), determined from the zero-field cooling (ZFC) curve of the  $\text{Co}^+$ -implanted epitaxial and polycrystalline films, at 15 K and 9 K respectively, indicate thermally relaxed magnetic interactions, i.e. superparam-



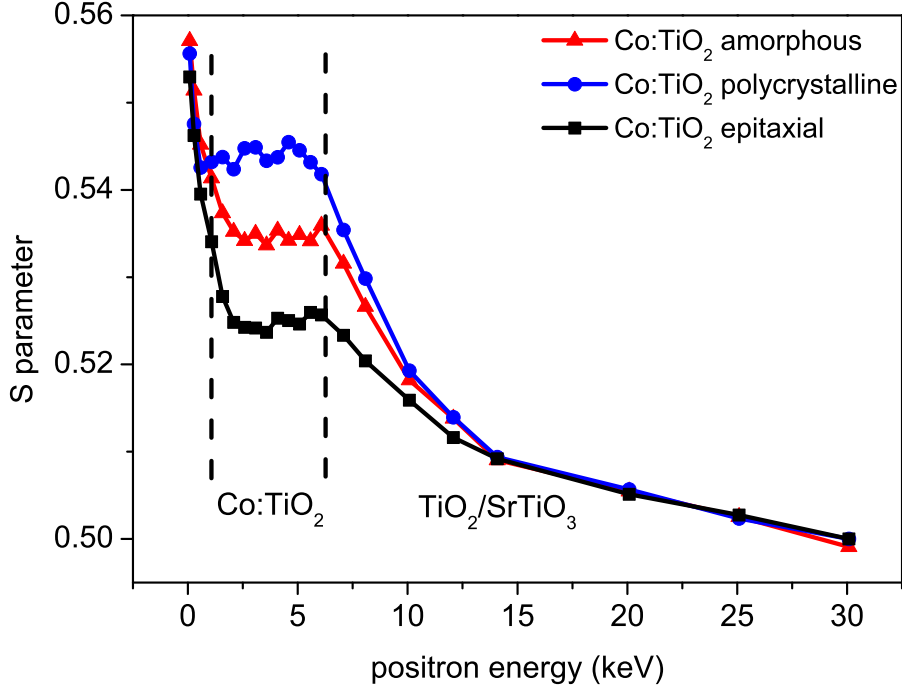


Figure 4.10: Measured positron-energy dependent S parameters for 5 at.% Co<sup>+</sup>-implanted TiO<sub>2</sub> films.

agnetic behavior. The thermal stability of a magnetic nanoparticle is determined by its volume and its anisotropy energy.  $T_B$  can be estimated by  $T_B \approx KV/30k_B$ , where  $K$  is anisotropy energy density,  $V$  is the particle volume and  $k_B$  is the Boltzmann constant [110]. Well known candidate phases for the origin of the observed superparamagnetism in the Co-Ti-O material system are hcp-Co ( $K=45 \times 10^4$  J/m<sup>3</sup>) [110] and cubic spinel Co<sub>3</sub>O<sub>4</sub> ( $K=9 \times 10^4$  J/m<sup>3</sup>) [111]. Using a size of 3 nm of the Co-rich particles as determined for the epitaxial film, the calculation yields blocking temperatures of  $\approx 15$ K and  $\approx 3$ K for hcp-Co and Co<sub>3</sub>O<sub>4</sub>, respectively. Moreover, magnetic field dependent magnetization measurements of both samples showed a ferromagnetic-like behavior (fig. 4.11 inset) below blocking temperatures, where, for Co<sub>3</sub>O<sub>4</sub>, it is expected to be an antiferromagnetic behavior [112]. Therefore, both TEM and SQUID results can be explained consistently by the formation of metallic hcp Co nanoparticles within the TiO<sub>2</sub> matrix. Additionally, the saturation magnetization of the Co<sup>+</sup>-implanted epitaxial and polycrystalline films were found to be 0.16 and 0.14  $\mu_B$  per Co atom, respectively (see inset in fig. 4.11). By comparison to the room temperature saturation magnetization of bulk hcp

Co ( $1.7\mu_B/\text{Co}$ )[113], it is estimated that, in the epitaxial and polycrystalline samples, less than 10% of the implanted Co atoms are concentrated in metallic nanoclusters. On the other hand, for the Co<sup>+</sup>-implanted amorphous film, only a paramagnetic signal could be detected, indicating the absence of superparamagnetic clusters. The non-existence of macroscopic room temperature FM in all three sample types does not necessarily exclude the presence of substitutional Co<sub>Ti</sub>, which are thought to give rise to FM according to Ref. [22, 50], but demonstrates the lack of an appropriate long-range magnetic coupling mechanism in the investigated samples.

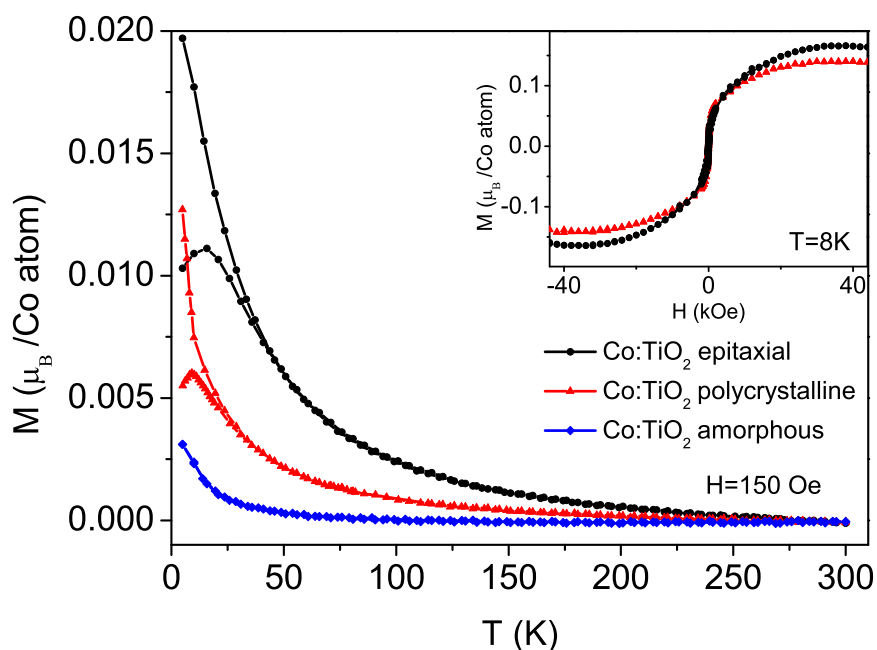


Figure 4.11: Temperature dependent magnetization curves (ZFC/FC) of Co<sup>+</sup>-implanted TiO<sub>2</sub> films with different microstructures.

#### 4.2.2.4 Local environment of implanted Co atoms

Co K-edge XANES spectra of three different Co<sup>+</sup>-implanted TiO<sub>2</sub> microstructures are shown in Fig. 4.12. The Co K-edge position of a metallic Co foil was used as an energy reference and the edge jump of all recorded spectra was normalized to unity. This allows for a proper comparison with Co, CoO [114] and CoTiO<sub>3</sub> [115] reference spectra [105]. The edge positions of the reference spectra were corrected with respect to metal

Co edge position, which is adjusted to the same energy position. The same main Co-K edge position of around 7720 eV was observed for all three Co:TiO<sub>2</sub> sample types, which is characteristic for Co in (II) oxidation state as can be inferred from the coincidence with the CoTiO<sub>3</sub> and CoO spectra. This indicates that the majority of the implanted Co atoms are indeed oxidized and only a small fraction forms the previously discussed metallic nanoclusters and the results are in agreement with the XANES results from 4 at.% Co<sup>+</sup>-implanted samples (see section 4.1). It is found that the pre-peak feature shape correlates with the presence of metallic Co clusters, i.e. it is most pronounced in case of the amorphous film where no Co cluster formation is observed, while an increase of the pre-peak feature broadening is observed for the polycrystalline and epitaxial samples, suggesting a dependence on nanocluster size and concentration. Besides the difference in the pre-peak region, the intensity of the white line at 7726 eV is significantly lower in case of the Co<sup>+</sup>-implanted amorphous film compared to the two crystalline samples. This behavior has been reported to be a signature of the prevalent tetrahedral local symmetry of Co, contrary to the octahedral environment [90].

Complementary characterization of the Co<sup>+</sup> implanted TiO<sub>2</sub> films was done by MO TKE at room temperature, where all films are in paramagnetic state. While no TKE signal could be observed for the Co:TiO<sub>2</sub> amorphous sample, the Co<sup>+</sup>-implanted polycrystalline and epitaxial anatase TiO<sub>2</sub> films showed a significant TKE signal (fig. 4.13). The observed optical transitions for the polycrystalline and the epitaxial Co:TiO<sub>2</sub> films coincide with intraionic transitions of Co (II) in octahedral oxygen coordination, which are located at around 0.9, 1.8 and 2.5 eV [116, 117]. The transitions observed around 3.1 eV are assigned to the band gap of the TiO<sub>2</sub> [118]. The MO TKE spectrum of the Co<sup>+</sup>-implanted epitaxial film resembles previously published data obtained from epitaxial anatase Ti<sub>1-x</sub>Co<sub>x</sub>O<sub>2-λ</sub> films on LaAlO<sub>3</sub> (100) substrate prepared by DC magnetron sputtering [119]. Thus, TKE measurements confirm the (II) octahedral oxygen coordination of Co, observed from XANES measurements for the Co<sup>+</sup>-implanted polycrystalline and epitaxial films. The approximately five times lower TKE signal of the present data than reported in Ref. 25, and the shift of the MO spectral features of polycrystalline film as compared to the epitaxial film suggest a competition between Co incorporation into the host lattice and secondary phase formation. Slightly different Co environment as follows

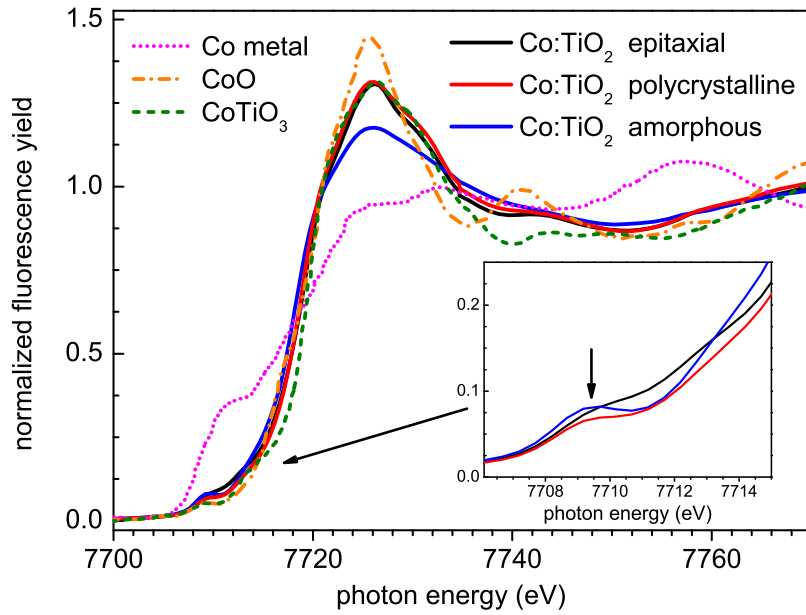


Figure 4.12: Co K-edge XANES spectra (normalized) of  $\text{Co}^+$ -implanted epitaxial anatase, polycrystalline anatase and amorphous  $\text{TiO}_2$  films together with Co K-edge spectra of Co foil,  $\text{CoO}$  [114] and  $\text{CoTiO}_3$  [115].

from XANES including different rutile-to-anatase ratios or metallic cluster formation may affect the TKE signal and determine the intricate shape and reduced intensity of the recorded MO spectra.

#### 4.2.2.5 Summary

$\text{TiO}_2$  films with different microstructures were implanted with 5 at.% Co. The presence of substitutional  $\text{Co}_{\text{Ti}}$  in the  $\text{Co}^+$ -implanted polycrystalline and epitaxial films was confirmed by a combination of XANES and magneto-optical spectroscopy methods. No long-range ferromagnetic ordering at room temperature has been observed for any of the three investigated  $\text{Co}:\text{TiO}_2$  structure types. The existence of metallic Co nanoclusters in epitaxial and polycrystalline films giving rise to superparamagnetism at low temperatures was revealed by TEM and SQUID magnetometry. The largest average cluster size and concentration was observed for epitaxial anatase  $\text{TiO}_2$ , whereas amorphous  $\text{TiO}_2$  shows paramagnetic behavior after  $\text{Co}^+$  ion implantation, indicating the absence of Co clusters.

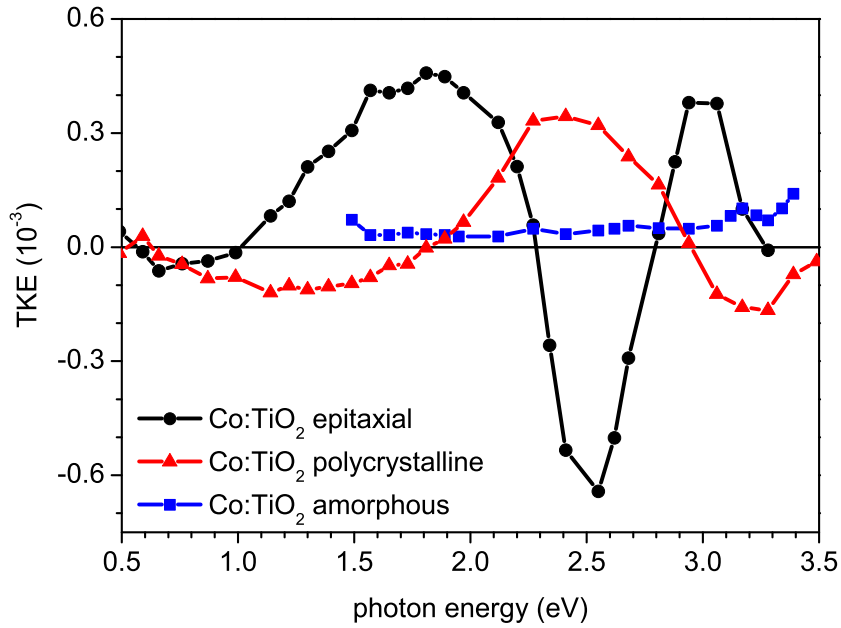


Figure 4.13: Room temperature magneto-optic (MO) transversal Kerr effect (TKE) spectra of Co<sup>+</sup>-implanted TiO<sub>2</sub> films with different microstructures.

Despite the cluster formation, high temperature ferromagnetism is absent and the substituting Co atoms are paramagnetic. This indicates that only the incorporation of the dopant within the host lattice cannot satisfy the requirements to achieve ferromagnetism. On the other hand, absence of defect-induced magnetism can be attributed to insufficient amount of defects within all of the Co:TiO<sub>2</sub> microstructures [120].

The results demonstrate that the initial microstructure of TiO<sub>2</sub> plays an important role for its magnetic properties induced by Co doping via ion implantation. Increasing the structural ordering from amorphous to polycrystalline and to epitaxial anatase promotes the formation of Co nanoclusters, which counteracts the synthesis of Co:TiO<sub>2</sub> based DMS materials.

## 4.3 Mn<sup>+</sup> implantation: from a non-magnet to a ferromagnet

### 4.3.1 Experiments

Simulated depth profile of 5 at.% manganese implantation into TiO<sub>2</sub> is given in figure 4.14. Only in this subsection (4.3), electrical transport properties of the films were characterized using a LakeShore HMS 9709 Hall Measurement system in the temperature range of 20 K and 300 K and applied external field range of 1 T with probe current of 1 mA. The Hall effect measurements were carried out in Van der Pauw geometry. Ohmic contacts were employed by sputtering gold onto sample corners and attaching silver wires with silver glue on top of gold layers.

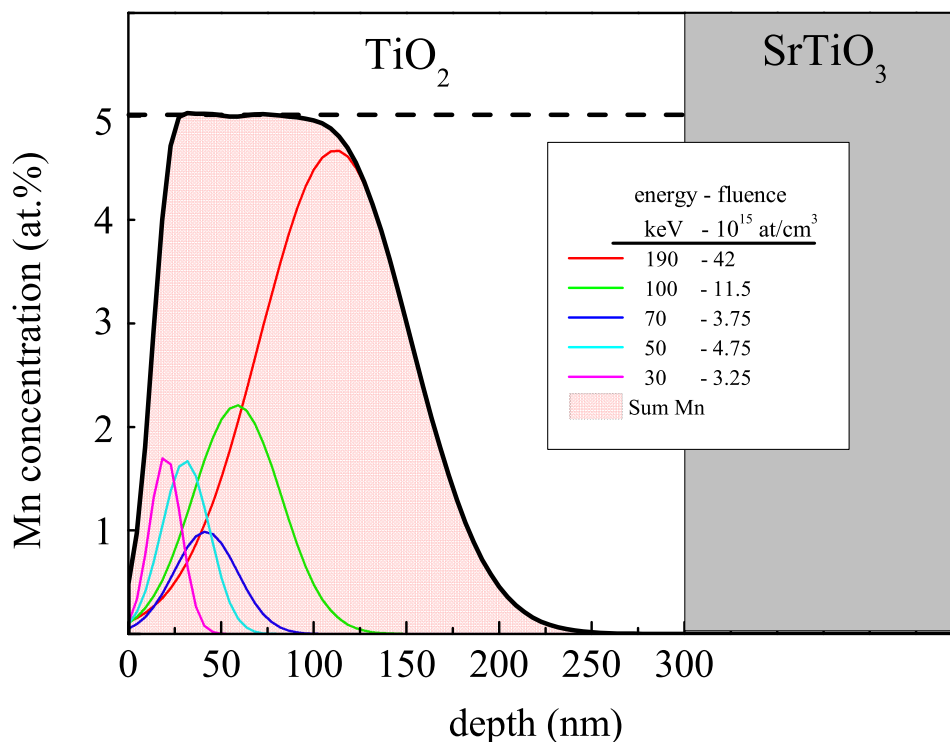


Figure 4.14: Calculated implantation profile for 5 at.% Mn doping into TiO<sub>2</sub> .

### 4.3.2 Relation between lattice damage and defects

The XRD patterns of as-grown and Mn<sup>+</sup>-implanted films are given in figure 4.15. XRD pattern analysis shows that all of the observed diffraction maxima of the polycrystalline and epitaxial films can be identified with the anatase phase of TiO<sub>2</sub>. Moreover, out-of-plane c-axis texture, i.e. TiO<sub>2</sub>(001)||STO(100), for as-grown epitaxial film is confirmed by rocking curve measurements at the anatase (004) reflection. Upon Mn<sup>+</sup> implantation, rutile formation is observed both in initially polycrystalline and epitaxial films (Fig. 4.15). However, given the weak contribution of rutile related peaks to the total XRD pattern, the initial anatase structure has been mostly preserved after implantation. Apart from the rutile phases, no other known Mn-related secondary phases could be detected by XRD.

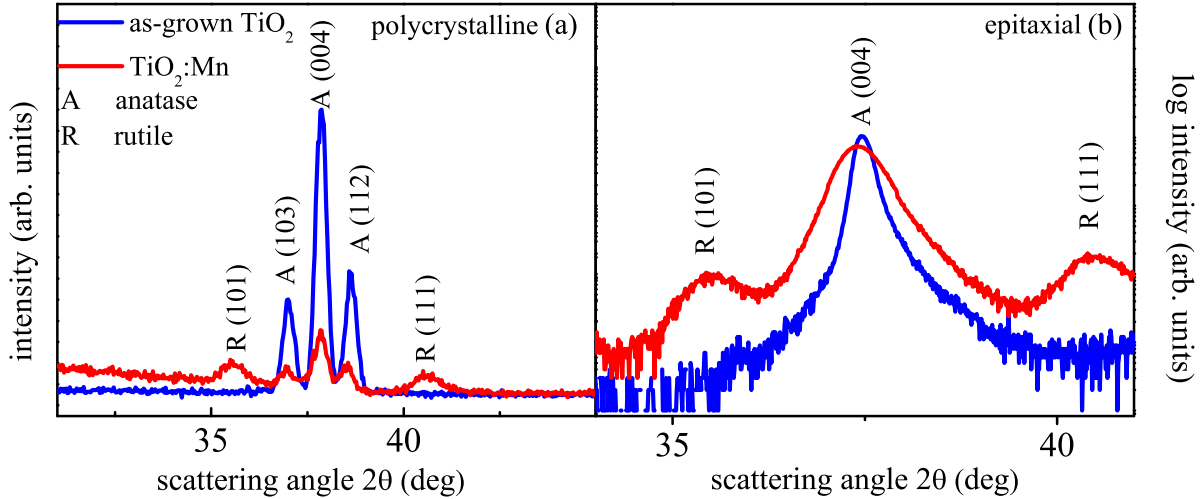


Figure 4.15: XRD patterns of as-grown and 5 at.% Mn<sup>+</sup>-implanted TiO<sub>2</sub> thin films: (a) polycrystalline films in 1° grazing incidence, and (b) epitaxial films in aligned symmetric 2θ-ω geometry.

Figure 4.16 depicts the S parameter in dependence of the positron energy as obtained from the PAS measurements on as-grown and Mn<sup>+</sup>-implanted TiO<sub>2</sub> films. The PAS measurements on as-grown TiO<sub>2</sub> films reveal that the concentration of open volume defects is the highest in as-grown amorphous TiO<sub>2</sub> and decreases in polycrystalline and further in epitaxial TiO<sub>2</sub>. (Fig.4.16 a). After the Mn<sup>+</sup> implantation this trend is preserved (Fig.4.16 b). The more pronounced plateau of the S-parameter depth profile observed in Mn<sup>+</sup>-implanted polycrystalline and epitaxial films may be attributed to an increased sub-

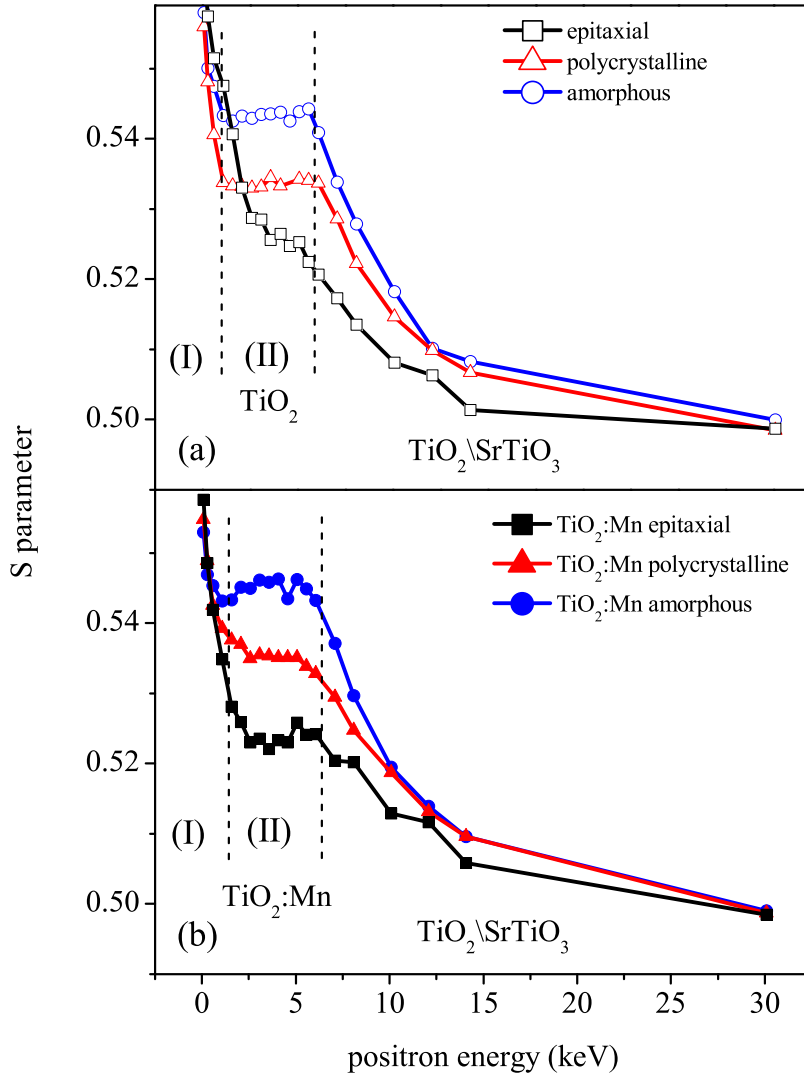


Figure 4.16: Energy-resolved depth profiles of S parameter for as-grown (a) and Mn<sup>+</sup>-implanted (b) TiO<sub>2</sub> structures. The insets show comparison plots of Mn<sup>+</sup>-implanted and as-grown polycrystalline (a) and epitaxial (b) TiO<sub>2</sub> films.

surface defect concentration leading to suppressed positron diffusion towards the surface, or similar to the previous section (4.2), can be attributed to the filling of Ti vacancies.

### 4.3.3 Electrical transport properties

The Mn<sup>+</sup>-implanted polycrystalline and epitaxial TiO<sub>2</sub> films show n-type degenerate semiconducting behavior (fig. 4.17), i.e. the electron density is temperature independent with free electron concentrations of  $1.54 \times 10^{19} \text{ cm}^{-3}$  and  $6.21 \times 10^{18} \text{ cm}^{-3}$ , for the Mn<sup>+</sup>-implanted polycrystalline and epitaxial films, respectively. The room temperature



electron mobility was  $\sim 2 \text{ cm}^2/\text{V}^{-1}\text{s}^{-1}$  for polycrystalline and  $\sim 15 \text{ cm}^2/\text{V}^{-1}\text{s}^{-1}$  for epitaxial Mn:TiO<sub>2</sub> film, which is comparable to reported values for Nb doped epitaxial anatase TiO<sub>2</sub> films [121]. In the case of amorphous films, the contact resistance was above the measurement limit ( $> 20 \text{ G}\Omega\cdot\text{cm}$ ). Additionally, no anomalous Hall effect was observed for any of the three Mn<sup>+</sup>-implanted samples within the investigated temperature range.



Figure 4.17: Temperature dependent resistivity measurements of Mn<sup>+</sup>-implanted epitaxial and polycrystalline anatase TiO<sub>2</sub> films.

#### 4.3.4 Local environment of implanted Mn atoms

Figure 4.18a shows the normalized Mn K-edge XANES spectra of the Mn<sup>+</sup>-implanted TiO<sub>2</sub> films. The positions of the Mn K-edges for all three Mn:TiO<sub>2</sub> structures, coincide with those of MnO [122] and MnTiO<sub>3</sub> [123], confirming that most of the implanted Mn atoms are in (II) oxidation state. In spite of an octahedral oxide coordination of Mn in both MnO and MnTiO<sub>3</sub>, the difference in the local Mn-O coordination depends on the distortion of the octahedra, which can also be probed and distinguished by XANES measurements [124, 125]. The XANES spectra of the three Mn:TiO<sub>2</sub> films are dominated by three common features A, B and C (Fig.4.18a). These features are most pronounced in the case of the epitaxial film and resemble the MnTiO<sub>3</sub> spectrum. With increasing

structural disorder from epitaxial to polycrystalline  $\text{TiO}_2$ , the features A to C tend to broaden. In particular, feature C, which appears as a weak shoulder in the polycrystalline film, vanishes in case of amorphous  $\text{Mn}:\text{TiO}_2$ , i.e. its presence reflects higher microstructural order. The Fourier transforms (FT) of the  $k^3\chi(k)$  weighted Mn K-edge spectra of the  $\text{Mn}^+$ -implanted  $\text{TiO}_2$  films are depicted in Fig. 4.18b. The most intense FT peak of the epitaxial film was found at the same position for Ti in anatase structure [126]. Correspondingly, peak at around 1.60 Å (marked with a dashed-dotted line) is related to the Mn-O distance in the octahedron. For the amorphous film this peak is shifted, which suggests a different Mn-O distance as compared to the epitaxial and the polycrystalline film. On the other hand, this peak contains a weak shoulder (shown by arrows) at around 1.3 Å for the epitaxial film. This shoulder becomes more pronounced for the polycrystalline and the amorphous films. This situation seems to reflect different distortions of the octahedron [127]. Backscattering amplitudes and sizes of Mn and Ti atoms are slightly different, so if both of these atoms occupy the equivalent positions in the same matrix, the corresponding EXAFS signal will be disturbed and the most intense line of the FT could broaden. As a consequence, for the amorphous film, Mn atoms show different coordination geometry as compared to the epitaxial film. The similarities between the spectra obtained from the epitaxial film and Mn environment in  $\text{MnTiO}_3$  and Ti environment in the anatase  $\text{TiO}_2$  imply that most of the implanted Mn atoms within the epitaxial film reside in Ti lattice sites. For the polycrystalline film, due to a pronounced shoulder at 1.3 Å as compared to the epitaxial film, the Mn atoms appear to have two types of oxide coordination geometries, i.e. only a partial incorporation of Mn by substitution of Ti must be assumed.

### 4.3.5 Magnetic properties

Temperature dependent magnetometry results for the  $\text{Mn}^+$ -implanted  $\text{TiO}_2$  structures are shown in figure 4.19. The  $\text{Mn}^+$ -implanted amorphous film exhibits a splitting between ZFC and FC curves and a spin-glass like transition at around 110 K (Fig. 4.19). This value is in agreement with the Néel temperature of MnO [128, 129], supporting the secondary phase-like coordination geometry of Mn in amorphous  $\text{TiO}_2$  found from

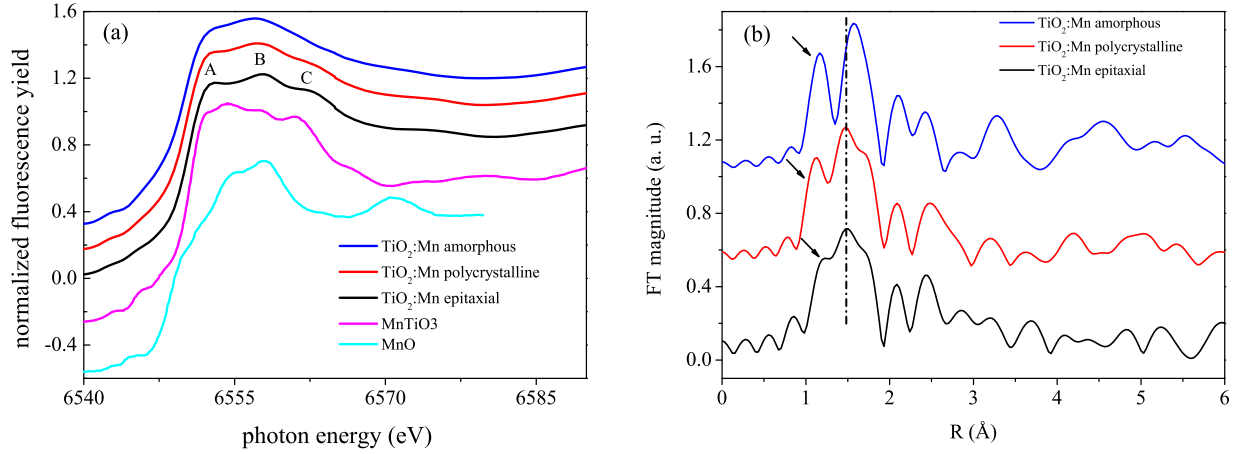


Figure 4.18: (a) Mn K-edge XANES spectra of Mn<sup>+</sup>-implanted TiO<sub>2</sub> structures along with reference spectra of MnO [122] and MnTiO<sub>3</sub> [123] (reference spectra shifted in energy axis for clarity by considering the energy calibration of experimental setup). (b) Fourier transform of  $k^3$ -weighted extended XANES spectra of the experimental data. Data was obtained in grazing incidence geometry at 1° to enhance the Mn fluorescence signal.

XANES measurements. Mn<sup>+</sup>-implanted polycrystalline film shows a ferromagnetic behavior with a  $T_C$  of around 230 K. At low temperatures ( $T \leq 25$  K) the magnetization of the polycrystalline film shows a tendency to decrease (Fig.4.19), suggesting the existence of antiferromagnetic interactions. The saturation magnetization of polycrystalline Mn:TiO<sub>2</sub> was found to be around  $0.85 \mu_B/\text{Mn}$  at 20 K (Fig. 4.19). These two contributions to magnetic properties of the polycrystalline film support the presence of two different local environments of Mn as indicated by XANES. By comparison to the amorphous film, the antiferromagnetic contribution is attributed to a Mn-related secondary phase, whereas the FM is due to the presence of Mn<sub>Ti</sub> substitutional sites. On the other hand, although most of the Mn atoms in the epitaxial film substitutes for Ti, this sample shows no signs of FM but, a well defined weak paramagnetic behavior. Recently it was reported that the FM in transition metal doped anatase TiO<sub>2</sub> appears above a certain carrier concentration ( $\sim 1.8 \times 10^{19} \text{ cm}^{-3}$ ) [39]. This is comparable to the value measured in polycrystalline Mn:TiO<sub>2</sub>, whereas the carrier concentration in the epitaxial sample is below. This may explain the absence of ferromagnetic interactions in the epitaxial Mn:TiO<sub>2</sub> sample investigated in the present work. Furthermore, compared to a previous study on 5 at.% Mn<sup>+</sup>-implanted rutile TiO<sub>2</sub> single crystals [61], the ferromagnetic behavior found for the polycrystalline film shows differences in saturation and thermal magnetization

behavior. The extrapolated Curie temperature in Ref.[61] was found to be around room temperature and the highest saturation magnetization is reported to be around  $0.4 \mu_B$ . These differences must be attributed to the use of rutile  $\text{TiO}_2$  in contrast to anatase  $\text{TiO}_2$  in the present study.

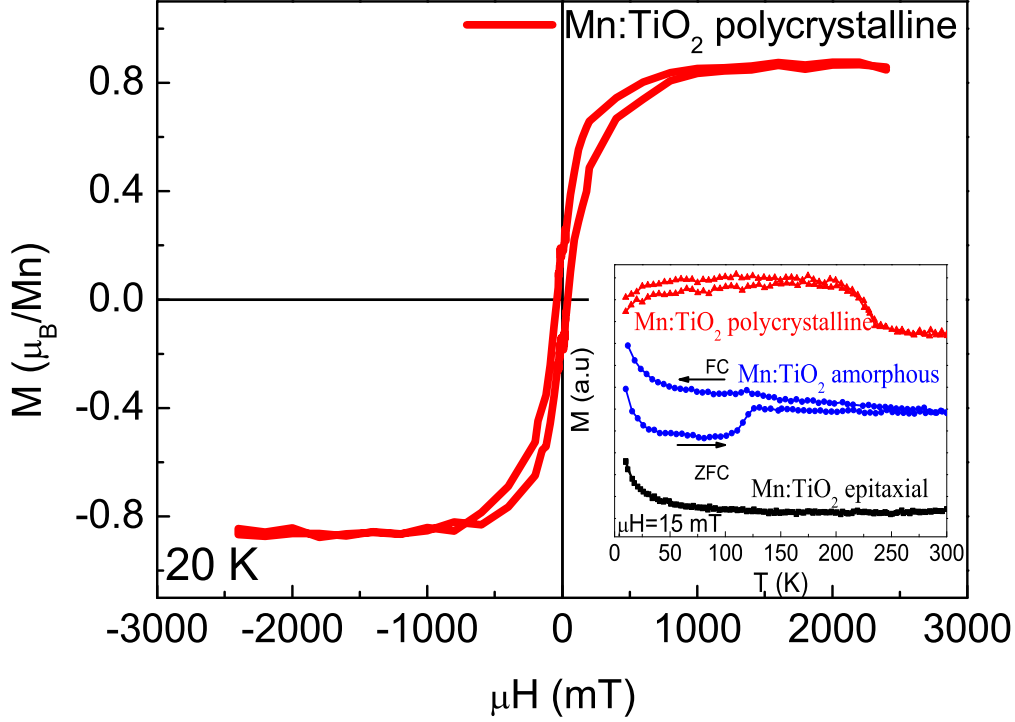


Figure 4.19: Field dependent magnetization curve of  $\text{Mn}:\text{TiO}_2$  film at 20 K. Inset shows thermal scans in 15 mT of the magnetization of  $\text{Mn}^+$ -implanted  $\text{TiO}_2$  films with different as-grown microstructures.

### 4.3.6 Summary

In summary, we prepared  $\text{Mn}:\text{TiO}_2$  with a Mn concentration of 5 at.%  $\text{Mn}^+$  as amorphous, polycrystalline anatase and epitaxial anatase structures. The initial microstructure, characterized by open volume defect concentration and crystallographic order, is found have direct consequences for the magnetic properties after  $\text{Mn}^+$  implantation. The FM, observed for the  $\text{Mn}^+$ -implanted polycrystalline film, is attributed to the presence of a high carrier concentration together with a sufficient amount of defects, which facilitate FM coupling of  $\text{Mn}_{\text{Ti}}$  sites. On the other hand, paramagnetic behavior was observed in case of the epitaxial  $\text{Mn}:\text{TiO}_2$  film, which showed the lowest defect concentration and

lower carrier density as compared to the polycrystalline film. The magnetic properties of the amorphous film is attributed to secondary phase formation. The observed dopant type, carrier and defect concentration dependent ferromagnetic behavior points towards an intrinsic mechanism for ferromagnetic order in Mn<sup>+</sup>-implanted polycrystalline anatase TiO<sub>2</sub> [130, 131].

## 4.4 V<sup>+</sup>-implanted TiO<sub>2</sub> thin films

### 4.4.1 Experiments

Calculated depth profile of implanted 5 at.% vanadium in TiO<sub>2</sub> is given in figure 4.20. Apart from the V<sup>+</sup> implantation, temperature dependent magnetization measurements along with XANES measurements V K-edge was performed.

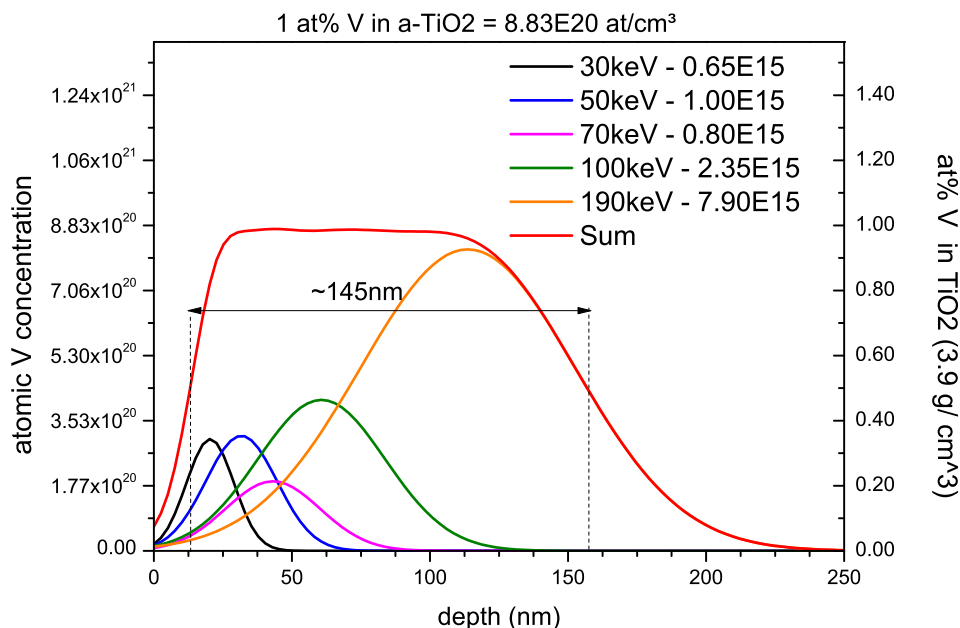


Figure 4.20: Depth profiles of V<sup>+</sup>-implanted into TiO<sub>2</sub> calculated by SRIM. Five different energy-fluence combinations have been used to achieve a box like sum profile. Fluences for 5 at.% concentration were calculated by simply multiplying each fluence values, which are shown in graph by 5.

### 4.4.2 Magnetic properties

After 5 at.% V<sup>+</sup> implantation into different microstructures of TiO<sub>2</sub>, resulting magnetic properties were investigated by means of temperature dependent magnetization measurements by applying a weak external field of 15 mT. Figure 4.21, 4.22, 4.23 show the thermomagnetic behaviors of V:TiO<sub>2</sub>.

As shown in figures above, magnetic response of the V<sup>+</sup>-implanted TiO<sub>2</sub> films mostly governed by a diamagnetic signal, as well as a weak increase at low temperatures, which indicates a paramagnetic behavior. On the other hand, no sign of any ferromagnetic

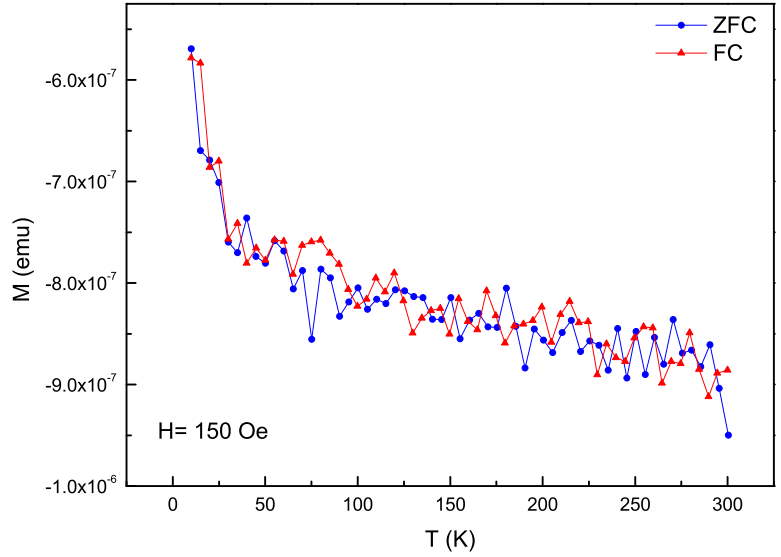


Figure 4.21: Temperature dependent magnetization curve of 5 at.% V<sup>+</sup>-implanted amorphous TiO<sub>2</sub>.

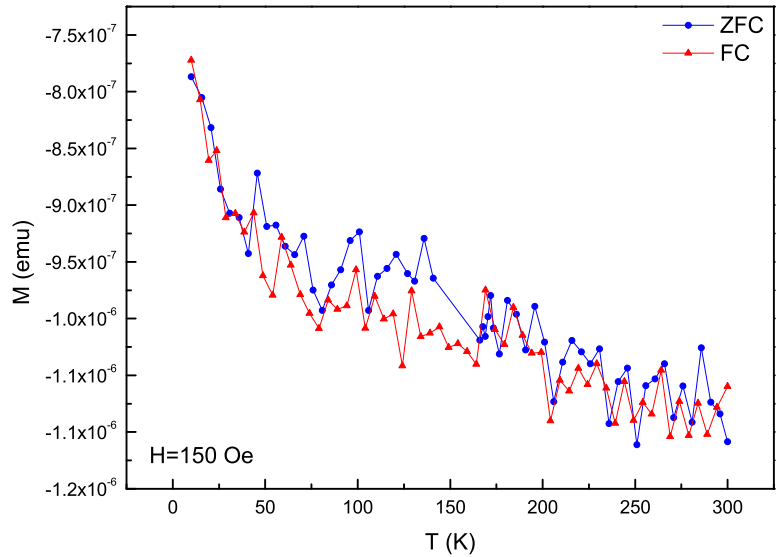


Figure 4.22: Temperature dependent magnetization curve of 5 at.% V<sup>+</sup>-implanted polycrystalline TiO<sub>2</sub>.

interaction was found for any of the three samples. The diamagnetic signal originates mostly from the SrTiO<sub>3</sub> substrate, due to relatively large amount of substrate mass as compared to TiO<sub>2</sub> film (i.e. the film thickness is 300 nm, while the substrate thickness is 500  $\mu$ m). The weak increase of the magnetization for all samples at the low temperatures can be attributed to paramagnetic centers, which are created either by inducing Ti<sup>+3</sup> ions

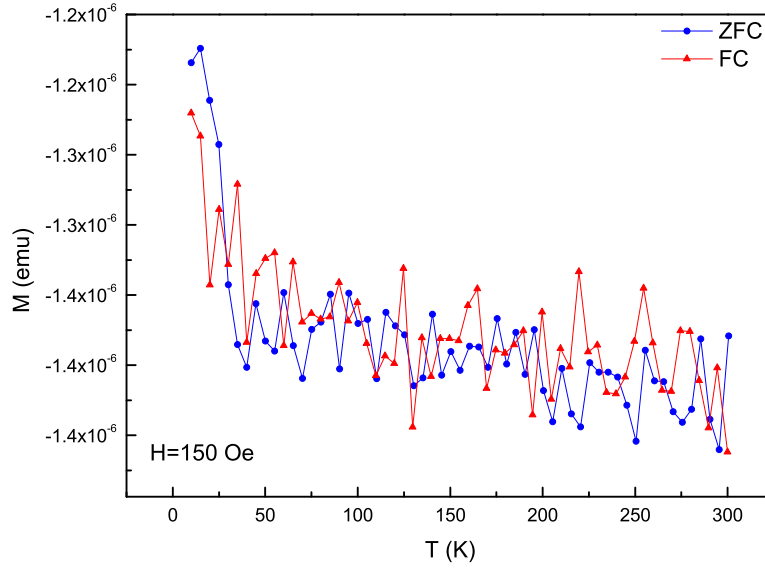


Figure 4.23: Temperature dependent magnetization curve of 5 at.% V<sup>+</sup>-implanted epitaxial TiO<sub>2</sub>.

after implantation or by metallic/substitutional V atoms. At this point, it is hard to discuss why any ferromagnetic signal was not observed. In order to draw conclusion on the lack of the ferromagnetism, it is essential to investigate the local environment and the oxidation state of the implanted V atoms. The investigation of the local environment of the implanted V atoms were carried out by performing XANES measurements at V K-edge. However, V K<sub>α</sub> line overlaps with the Ti K<sub>β</sub> line. Moreover, due to low amount of the V atoms compared to Ti atoms, which involves both TiO<sub>2</sub> and SrTiO<sub>3</sub> substrate, it was not possible to observe fine structures of V K-edge spectra for all of the V<sup>+</sup>-implanted samples.

In figure 4.24, V K-edge from V<sup>+</sup>-implanted epitaxial TiO<sub>2</sub> is depicted. As shown, the obtained spectrum, even after many corrections and ten times longer measurement time as compared to the measurements performed on Co and Mn implantations, remains noisy, which makes a detailed XANES analysis on fine features impossible. On the other hand, as compared to V metal, the main edge position of the film is shifted 13 eV to higher energies, which shows that most of the implanted V atoms are indeed oxidized. The position of the edge jump coincides with V K-edge of an V<sub>2</sub>O<sub>4</sub>, in which V atoms have +4 oxidation state [132]. The found oxidation state of V within epitaxial TiO<sub>2</sub> is also in agreement with Ti atoms oxidation state in TiO<sub>2</sub>. However, without identifying the



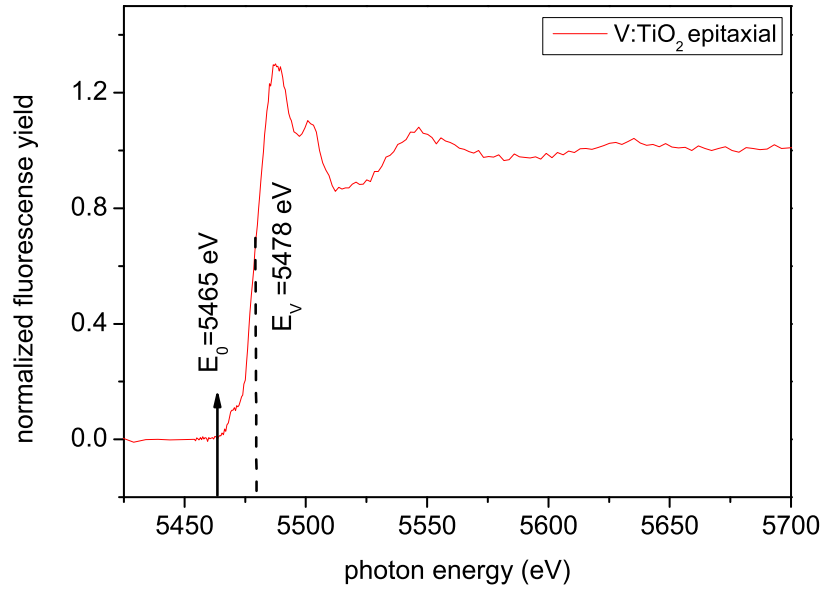


Figure 4.24: V K-edge X-ray absorption spectrum for 5 at.%  $V^+$ -implanted epitaxial anatase  $TiO_2$  film.

distribution of the oxygen atoms around V atoms, it is hard to distinguish substitutional V atoms from possible secondary phases of  $V_2O_4$ .

### 4.4.3 Summary

In summary, amorphous, polycrystalline anatase and epitaxial anatase  $TiO_2$  thin films were implanted with 5 at.% concentration of  $V^+$ . Independent from initial host microstructure, none of the films showed any sign of a ferromagnetic signal. The reason of the lack of ferromagnetism remains unclear due to very low resolution of XAS on V  $K_\alpha$  which sits in the vicinity of Ti  $K_\beta$  line.



---

## The effect of the open volume defects on the magnetic properties of V:TiO<sub>2</sub> films prepared by doping during deposition

---

In this chapter the correlation between the amount of the negatively charged open volume defects (e.g. Ti vacancies) and magnetic properties of vanadium doped TiO<sub>2</sub> films are studied. The different amount of defects also leads to different electrical transport behavior, i.e. semiconducting and insulating. Therefore, this section also considers the relation between charge carriers and ferromagnetic order in V:TiO<sub>2</sub> systems.

### 5.1 Experiments

Oxygen deficient Ti<sub>0.99</sub>V<sub>0.01</sub>O<sub>2-λ</sub> thin films of 600 nm thickness were sputtered onto LaAlO<sub>3</sub> (001) substrates by magnetron sputtering from a metallic Ti<sub>0.99</sub>V<sub>0.01</sub> alloy target in argon-oxygen atmosphere at total pressure of  $1.2 \approx 10^{-2}$  Torr. The substrates were kept at 650 °C during film deposition. By variation of the oxygen fraction in the chamber atmosphere, conducting, semiconducting ( $\rho \approx 0.008 \Omega\text{cm}$ ) or insulating ( $\rho \geq 200 \text{ G}\Omega\text{cm}$ ) films have been prepared. Kept in air, overtime as-grown films with metallic conductivity have transformed into semiconductors and therefore they are disregarded in this study. open volume defects within samples were investigated by PAS measurements,

which were performed at the Slow Positron System of Rossendorf by the depth-resolving Doppler broadening method. The structural characterizations were performed by means of XANES and energy dispersive X-ray (EDX) spectroscopy. The magnetic properties of the films were investigated by means of thermomagnetic and magnetic field versus magnetization measurements by employing SQUID magnetometry.

## 5.2 Structural Properties

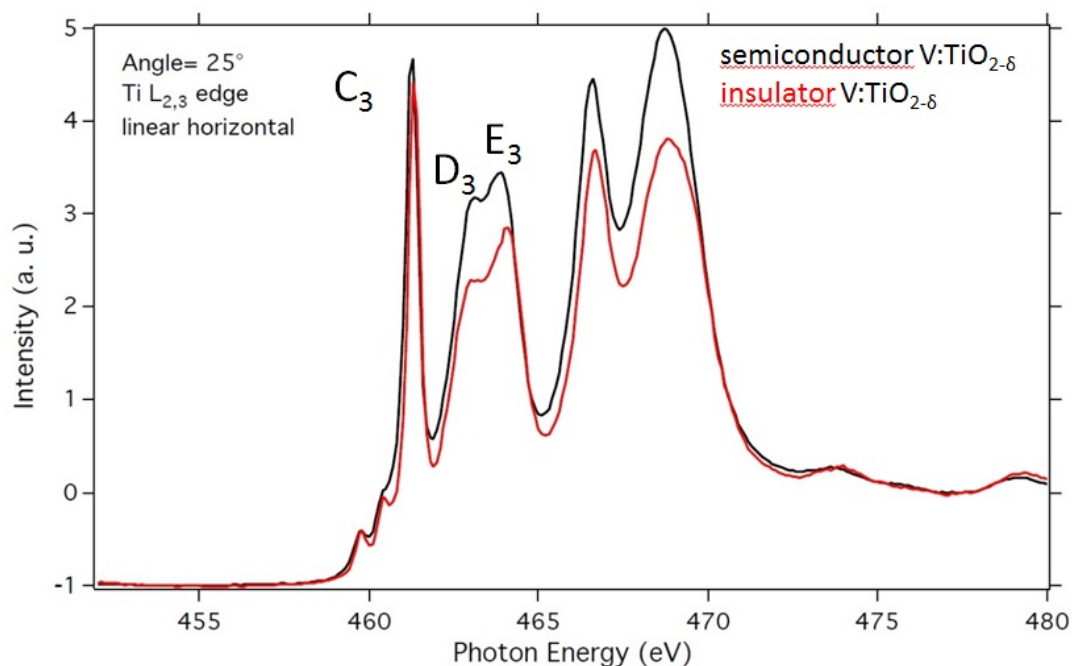


Figure 5.1: XANES measurement at Ti K-edge of semiconductor and insulator V:TiO<sub>2-δ</sub> films.

As a result of high temperature film growth, V:TiO<sub>2</sub> showed a mixture of rutile/anatase structure. In addition, element-selective XANES has been applied in soft- and hard X-rays ranges at the L<sub>2,3</sub> and K absorption edges of titanium for structural characterization, which confirmed the presence of rutile phases in the films (figure 5.1). Nevertheless, XANES spectra at the vanadium L<sub>2,3</sub> absorption edges were not detected. The most obvious explanation of this fact is the strong background signal from titanium atoms in the film and lanthanum atoms in the substrate, since all of these fluorescent lines are not well enough resolved. Energy-Dispersive X-ray spectra of the as prepared Ti<sub>0.99</sub>V<sub>0.01</sub>O<sub>2-λ</sub>

films showed the absence of the  $K_{\alpha-\beta}$  fluorescent lines of iron or cobalt contaminations (6-7 keV). Instead, La, Al, Ti, O and V lines were observed (see Fig. 5.2). Due to the low V concentration only the  $K_{\alpha}$  line of vanadium (4.95 keV) is rather well resolved while the  $K_{\beta}$  line (5.43 keV) has a non-detectable intensity. Note that from the previous section (4.4), Ti  $K_{\beta}$  and V  $K_{\alpha}$  coincides. Consequently, the quantitative determination of V concentrations is not possible with sufficient precision.

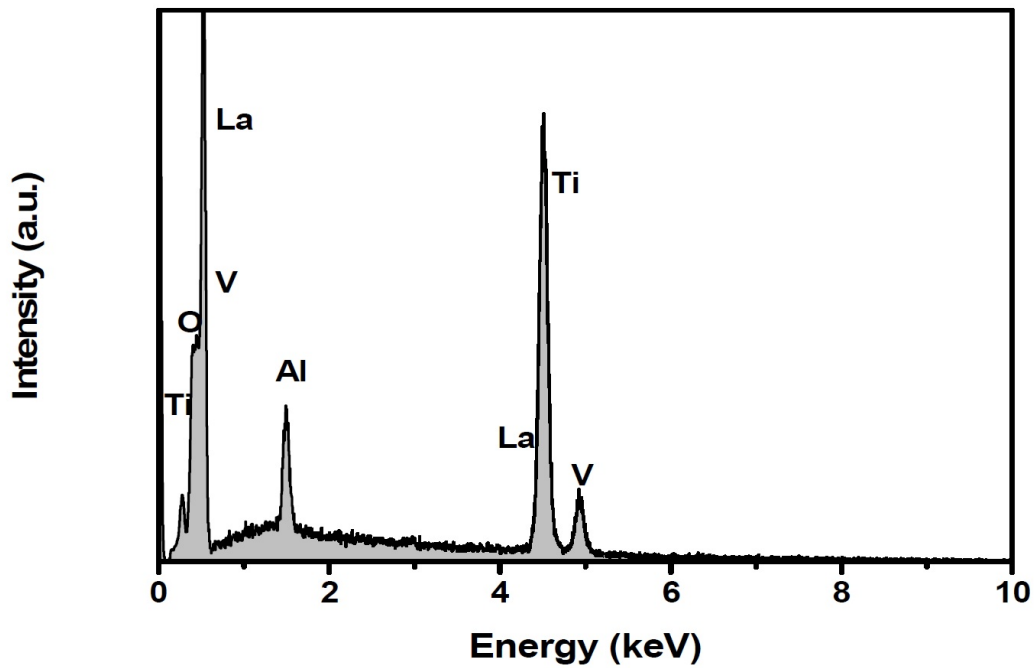


Figure 5.2: EDX spectrum of insulating  $\text{Ti}_{0.99}\text{V}_{0.01}\text{O}_{2-\lambda}$

### 5.3 Investigation of the open volume defects

In the case of V- doped  $\text{TiO}_{2-\lambda}$  films, PAS spectroscopy could be used effectively to explore Ti vacancies. As shown figure 5.3, each curve has three characteristic regions: (i) below 2 keV, which represents the surface region of the  $\text{TiO}_{2-\lambda}$  film, (ii) between 2-9 keV, which relates to the bulk  $\text{TiO}_{2-\lambda}$  and (iii) above 9 keV, which corresponds to the interface between the film and  $\text{LaAlO}_3$  substrate. The main interest is focused at the first and the second regions. Compared to the semiconducting sample, the insulating film shows a steeper slope of this dependency in the first region followed by a well pronounced plateau with the visibly smaller S-parameter, which refers to a more ordered and uniform

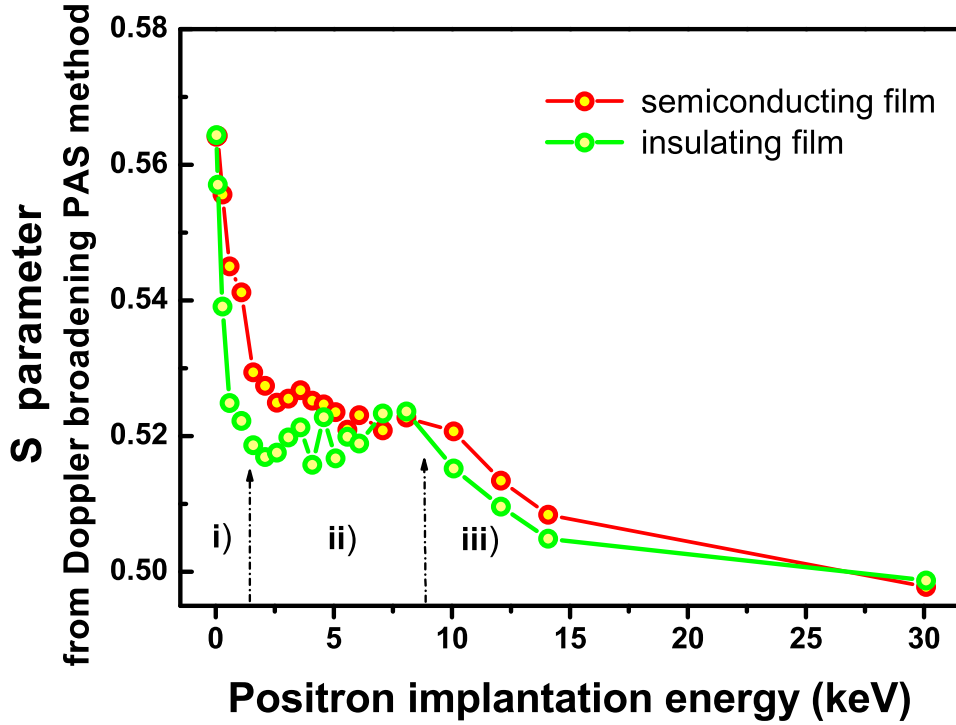


Figure 5.3: The energy dependent S-parameter measurement of insulating and semiconducting V:TiO<sub>2</sub>.

structure of bulk insulating film with a lower defect concentration. The absence of a plateau and a higher S parameter within the second region in the case of semiconductor sample indicates a higher concentration of open volume defects across the whole volume of the film. The decrease of S parameter in the third region reflects the transition from the defective films to the highly perfect single crystalline LaAlO<sub>3</sub> substrate.

## 5.4 Magnetic, optical and electrical properties

A clear magnetic behaviour with pronounced hysteresis at room temperature was found for semiconducting and insulating Ti<sub>0.99</sub>V<sub>0.01</sub>O<sub>2-λ</sub> films (Fig. 5.4). The coercive field of about 300 Oe is rather typical for Co:TiO<sub>2-λ</sub> systems with different concentrations of impurities and was also previously found for V:TiO<sub>2-λ</sub> films grown on rutile TiO<sub>2</sub> single crystal substrates [133]. The saturation magnetization for the semiconducting and insulating film corresponds to  $\approx 0.90\mu_B$  and  $0.63\mu_B$  per vanadium atom, respectively. These values differ from the results obtained by Hong et al. [134] and Orlov et. al. [135] results, where for higher V doping levels, larger magnetic moments per vanadium atom

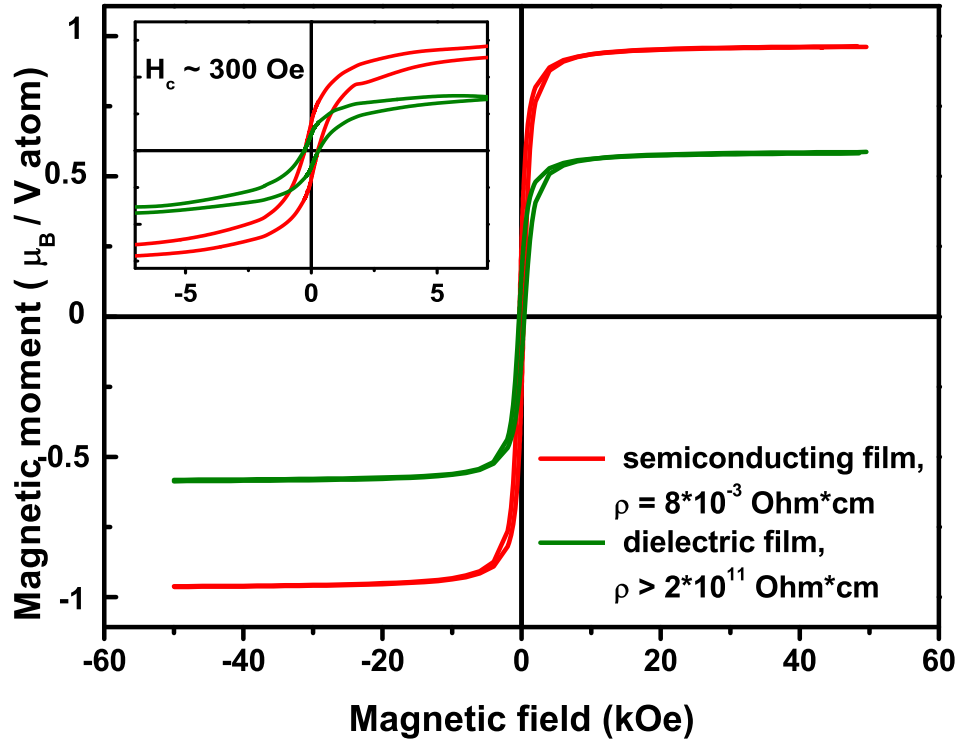


Figure 5.4: Magnetic field dependent magnetization curves of semiconducting and insulating V:TiO<sub>2</sub> films.

were found. The shape of the spectra and the magnitude of the transversal Kerr effect can

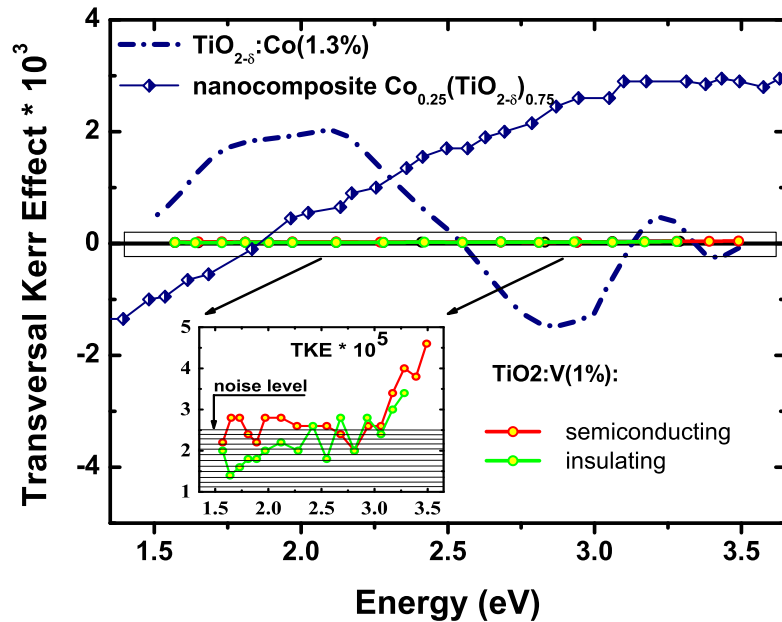


Figure 5.5: MO spectra for semiconducting and insulating V:TiO<sub>2</sub>, along with Co:TiO<sub>2</sub> reference data.

be used to determine the presence of 3d clusters in the sample studied. Surprisingly, none

of the measured MO spectra indicates the presence of spin-orbit interaction of vanadium impurities with the  $\text{TiO}_{2-\delta}$  matrix (Fig. 5.5) despite the fairly strong magnetic moment per impurity atom found from the magnetometry data. The absence of the MO signal can be considered not only as an exclusion of the V moment as the source of the ferromagnetic properties but also indirectly suggests the absence of ferromagnetic Fe and Co impurity clusters in the films.

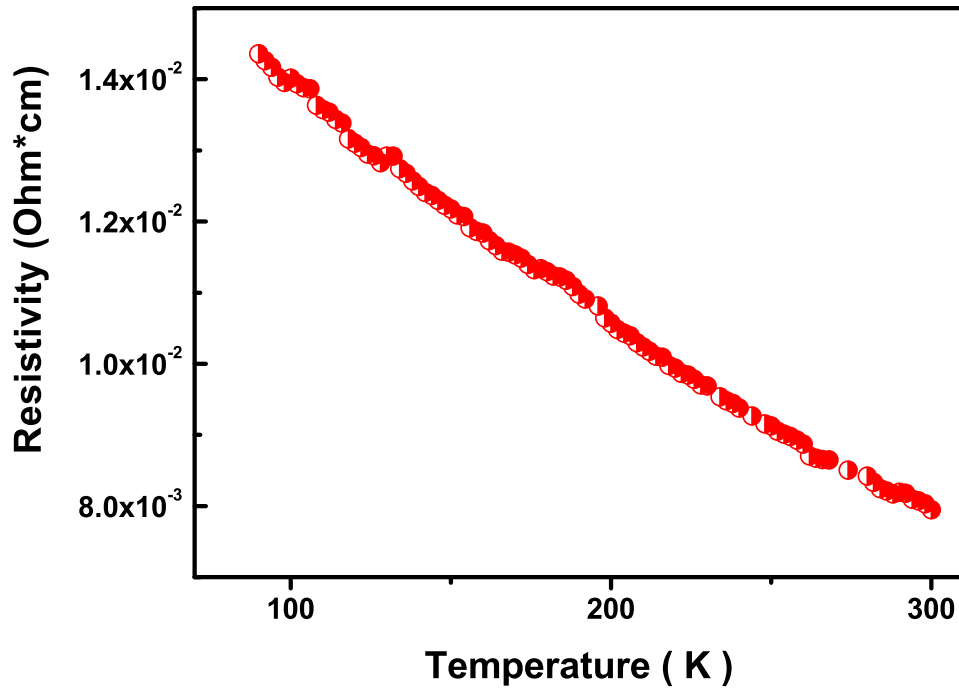


Figure 5.6: Temperature dependent resistivity of semiconducting V:TiO<sub>2</sub> film.

Temperature dependent charge transport measurements revealed n-type conductivity with  $d\rho/dT < 0$  for the semiconducting film in the temperature range of 90 K to 300 K (Fig. 5.6). Hall resistivity curves showed linear dependence on the magnetic field with no signature of anomalous Hall effect contribution.

## 5.5 Summary

As a summary, the results of structural, magnetic, transport, magneto-optical and positron annihilation studies of  $\text{Ti}_{0.99}\text{V}_{0.01}\text{O}_{2-\lambda}$  thin films have been presented. Room temperature ferromagnetism was observed in films with significantly different conductivities. The higher saturation magnetization of the semiconducting sample is found to



correlate well with a higher density of negatively charged structural defects as probed by PAS. Possible candidates for these defects are Ti vacancies or defect complexes involving  $\text{Ti}^{+3}$  [136]. Therefore, it is proposed that these types of defects (and their agglomerations) should be taken into account when considering room temperature ferromagnetism in V-doped  $\text{TiO}_{2-\lambda}$  in addition to the influence of positively charged oxygen vacancies and their complexes. Furthermore, the negligible magneto-optical transversal Kerr effect response and the absence of the anomalous Hall effect supports the assumption of defect-induced origin of magnetism in studied  $\text{Ti}_{0.99}\text{V}_{0.01}\text{O}_{2-\lambda}$  films without involvement of free charge carriers or the local magnetic moment of the V ion.



## 6.1 Defects in $\text{TiO}_2$

Positron annihilation spectroscopy investigations on different microstructures of as-grown  $\text{TiO}_2$  films revealed that the crystalline order of the films with respect to the substrate's crystalline order, dramatically influences the amount of the open-volume defects within  $\text{TiO}_2$  thin films grown on  $\text{SrTiO}_3$  (100) substrates. Figure 6.1 shows the relative amount of negatively charged open-volume defects (e.g.  $\text{Ti}^{+4}$  vacancies) within different microstructures of as-grown  $\text{TiO}_2$  thin films. The amounts were extracted from S parameter versus positron energy curves. As shown in figure 6.1, increased quality of the epitaxial relation by increasing the substrate temperature during growth results in less open-volume defects. Moreover, from epitaxial anatase to amorphous  $\text{TiO}_2$ , the amount of the open-volume defects increases. The epitaxial structure, in general, consists of crystalline grains, which are aligned in certain direction with respect to the substrate. Moreover, it is already reported that the increase in the epitaxial quality leads to fewer, and therefore larger, grains [137]. Likewise, within a polycrystalline structure, these structural grains exist. The grains inside a polycrystalline structure are oriented randomly and the amount of such structural grains is larger as compared to epitaxial films.

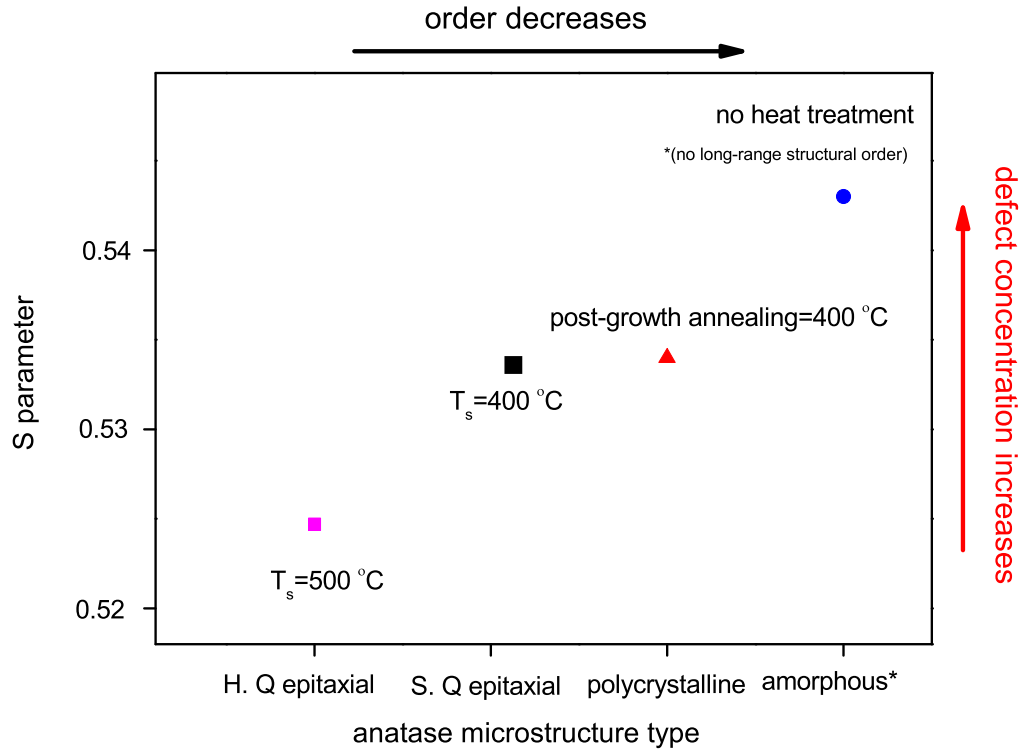


Figure 6.1: Evolution of the open-volume defects within different microstructures of as-grown  $\text{TiO}_2$  films.

The amount of the grains defines also the amount of the grain boundaries, which involves most of the structural defects. Therefore, the polycrystalline structure is expected to have more grain boundaries, which also consistently explains the increase in the amount of open-volume defects as compared to the epitaxial structure.

## 6.2 Formation of secondary phases

As shown in chapter 4,  $\text{Co}^+$  implantation into crystalline anatase  $\text{TiO}_2$  leads to formation of metallic nanoclusters after certain implantation concentration. The cluster formation starts to be visible at 5 at.% implantation concentration, whereas at 4 at.% implantation concentration, implantation induced cluster formation is not visible by means of any of the characterization methods that were employed. Therefore, 5 at.% implantation concentration is defined to be the threshold  $\text{Co}^+$  implantation concentration for metallic nanocluster formation within anatase  $\text{TiO}_2$  (fig. 6.2).

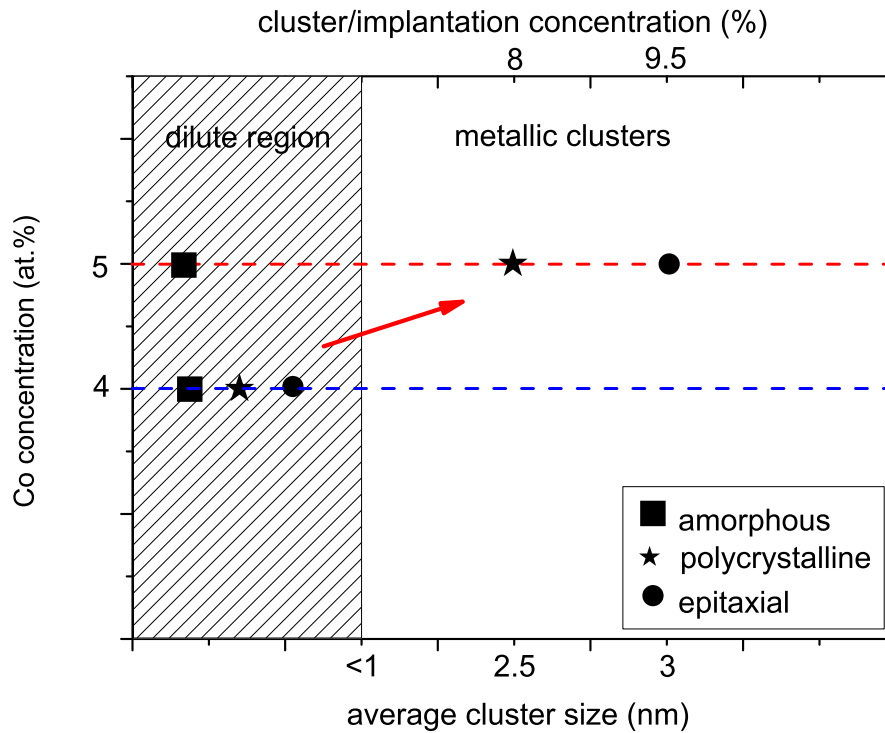


Figure 6.2: Formation of metallic cobalt nanoclusters in  $\text{Co}^+$  implanted  $\text{TiO}_2$  films.

The size of the metallic nanoclusters, as explained in Chapter 4.2.2, depends on the initial microstructure of the host  $\text{TiO}_2$ . With lower microstructural order, namely, in polycrystalline anatase  $\text{TiO}_2$ , implanted cobalt concentrates in smaller nanoclusters. Moreover, the amount of the metallic nanocluster concentration, which can be estimated from TEM images, appears to be less in polycrystalline anatase  $\text{TiO}_2$  film as compared to the epitaxial anatase  $\text{TiO}_2$ .

Therefore, considering the reduced amount and the average size of the implantation induced metallic nanoclusters when going from epitaxial anatase  $\text{TiO}_2$  to polycrystalline anatase  $\text{TiO}_2$ , the further suppression or the tailoring of metallic nanoclusters (changing the size or the orientation of the particles [138]) can be achieved by further tuning of the initial host microstructure, towards different qualities of the polycrystalline film.

After  $\text{Mn}^+$  implantation into different microstructures of  $\text{TiO}_2$ , instead of metallic nanoclusters,  $\text{MnO}$ -based secondary phases were found for both amorphous and polycrystalline anatase  $\text{TiO}_2$  films. On contrary to the  $\text{Co}^+$  implantation, secondary phase formation appears to decrease when increasing the structural order in  $\text{Mn}^+$ -implanted films.

### 6.3 Evolution of the ferromagnetism in different microstructures of TiO<sub>2</sub>

Table 6.1: Microstructure and dopant type dependencies of magnetic properties for 5 at.% transition metal implanted anatase TiO<sub>2</sub> thin films.

	V	Mn	Co
amorphous	weak PM	secondary phases	weak PM
polycrystalline	weak PM	FM+secondary phases	PM+secondary phases
epitaxial	weak PM	PM	PM+secondary phases

In order to understand the evolution of the ferromagnetism within Mn:TiO<sub>2</sub> systems, it is essential to look at whole picture of different types of TM implantations into different microstructures of TiO<sub>2</sub> (table 6.1). In the case of Co<sup>+</sup> implantation, in spite of the metallic cluster formation, a large amount of substitutional Co<sub>Ti</sub> sites within crystalline films was confirmed by means of X-ray absorption and magneto-optical spectroscopy measurements. Additionally, this case was also found to be valid for Mn:TiO<sub>2</sub>. Therefore, crystallinity is found to be promoting the substitutional sites within anatase TiO<sub>2</sub> upon transition metal ion implantation. However, when the structural order increases from the polycrystalline phase to the epitaxial phase of anatase, either nanocluster formation becomes more dramatic (e.g. for Co<sup>+</sup>-implanted epitaxial anatase TiO<sub>2</sub>) or ferromagnetism collapses, due to absence of sufficient amount of structural defects. On the other hand, when the crystalline order decreases to polycrystalline anatase TiO<sub>2</sub>; in the case of Co:TiO<sub>2</sub>, the amount of the cluster formation is suppressed, while for the case of the Mn:TiO<sub>2</sub>, polycrystallinity gives rise to ferromagnetism, due to its higher carrier concentration and sufficient amount of defects, in spite of the existence of MnO-based secondary phases.

The observed microstructure dependent magnetic properties reflect a strong influence of the open-volume defects. At the first glance such a dependency suggests defect-induced FM interactions, or so-called d<sup>0</sup> magnetism. Defect-induced ferromagnetic order occurs above a certain open-volume defect concentration. This defect concentration is believed to be the concentration, at which point they introduce levels in the bandgap, and the

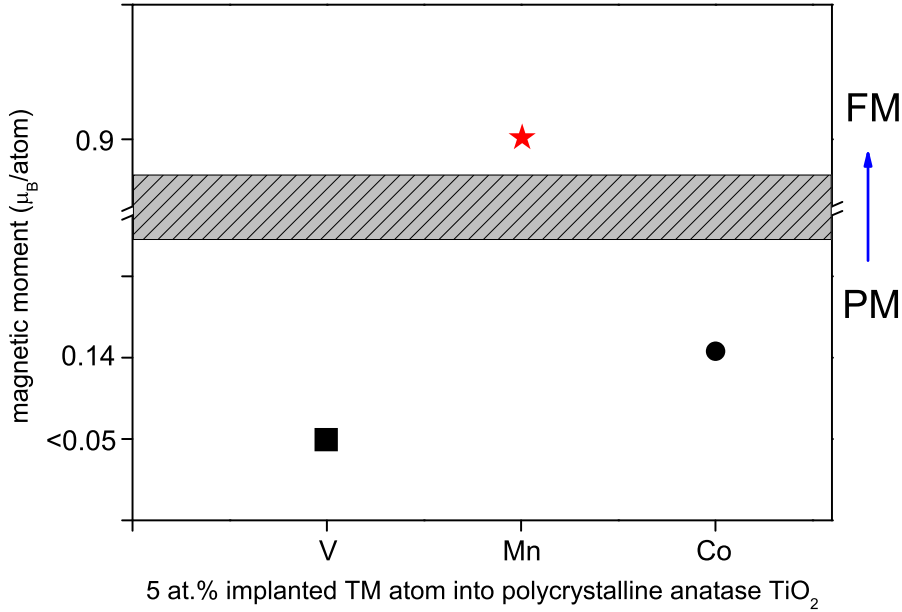


Figure 6.3: Observed magnetic properties of 5 at.% transition metal ion implanted polycrystalline anatase  $\text{TiO}_2$

electrons that occupy those levels form spin states of either 0 or  $1/2$  [139]. Likewise, almost all of the reported results on defect induced FM claim that such an order exists at higher temperatures than room temperature. By taking into account d0 FM, our results significantly differs in two main points. Firstly, the observed FM for the polycrystalline  $\text{Mn}:\text{TiO}_2$  has a transition temperature to paramagnetic state at around 230 K. Also, it is found that the observed FM is correlated to the dopant type. It is shown that, under equivalent conditions cobalt implantation leads to paramagnetic substitutional  $\text{Co}_{\text{Ti}}$  sites without a sign of any high temperature FM. Moreover, as can be expected due to similar masses of both Mn and Co, they induce almost identical defect characteristics to a polycrystalline anatase  $\text{TiO}_2$  film (Fig. 6.4). Thus, comparison of both studies suggests another mechanism than only d0 magnetism. According to bound magnetic polaron model [50], charge carriers are associated with structural defects and magnetically coupled with dopant d electrons. Due to their localization in the vicinity of the defects, the amount of the magnetic polarons is proportional to the amount of defects and the magnetization scales with the amount of effective substitutional dopant sites [64]. Moreover, such a magnetic coupling occurs via free charge carriers, therefore having sufficient amount of free carrier concentration is essential. The bound polaron model shows a better fit to

our findings. Therefore, we propose that the polycrystalline anatase  $\text{TiO}_2$  is an excellent structural candidate to attain ferromagnetism in DMOs.

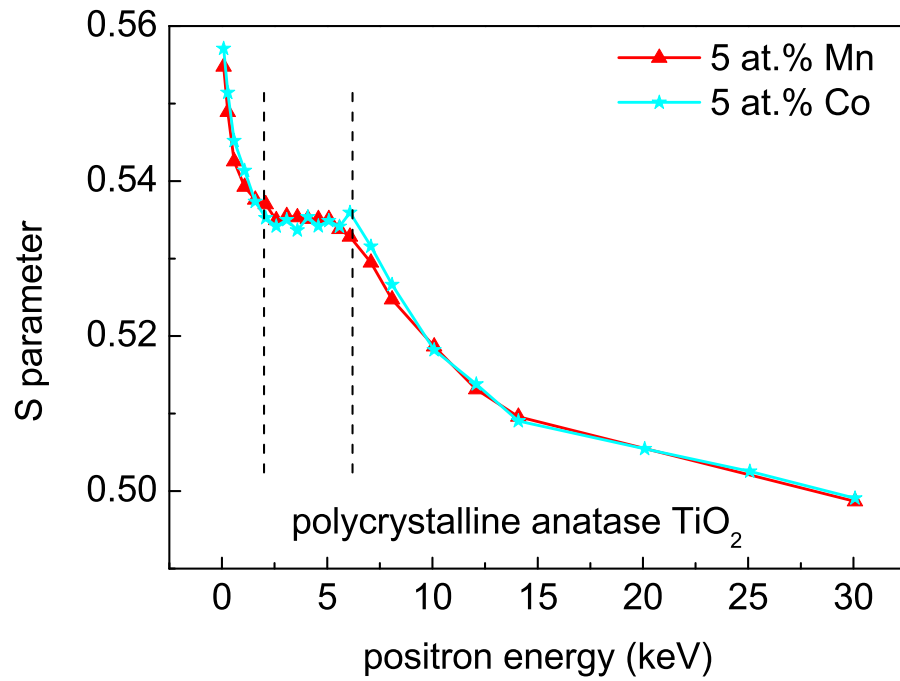


Figure 6.4: Comparison of energy-resolved S parameters for  $\text{Co}^{+}$ - and  $\text{Mn}^{+}$ -implanted polycrystalline anatase  $\text{TiO}_2$  films.





## CHAPTER 7

---

### Acknowledgments

---

First of all I would like to thank Dr. Kay Potzger for being my acting-supervisor. I am very grateful for being his PhD student and for sharing his broad knowledge. But, most of all, I deeply thank him for his trust on my ideas (even though some of them were bit nonsense). Last but not least, I am very thankful to him for hiring me for DETi.2 project, which was my PhD project.

I also want to thank Prof. Jürgen Faßbender for supervising this thesis and giving me the opportunity to conduct my PhD studies at Helmholtz-Zentrum Dresden - Rossendorf.

Furthermore, I want to thank Dr. Jürgen Lindner, for his support and fruitful discussions.

The next, I am grateful to acknowledge Dr. Steffen Cornelius for sharing his broad experience on oxides and structural characterization methods. I deeply thank him for answering my questions repeatedly, for really nice, efficient and useful discussions.

I also want to thank the partners of DETi.2 project from Moscow, Dr. Alevtina Smekhova, Prof. Dr. Nikolay Perov, Prof. Dr. Elena Ganshina, Prof. Dr. Alexander Granovsky, Dr. A. Orlov, Yuriy and Georgi for supplying me samples, giving me opportunity to use their facilities and guiding me in Moscow to very nice restaurants and bars.

I also want to acknowledge Dr. Anna Semisalova, who were initially at Moscow side of the project and at almost the end of the project has joined German side, for her help with my thesis, for being very friendly host to me during all of my visits to Moscow.

Without friends PhD study would be pretty boring, therefore, I must thank my friends; Yuriy Aleksandrov, Dr. Ciaran Fowley, Dr. Helmut Schulteiß and Julia Osten for nice and relaxing breaks. Moreover, I want to thank Ciaran not only for proof reading all my texts (papers and thesis) also for introducing me the real Guinness. Also, many thanks to Julia for introducing me to Kay when I was an internship student and her help for almost anything during my PhD study. Finally, many thanks to Helmut, for giving me the green Dragon- 97 Renault Twingo, which brought me to many places within a year.

For his patience to my excessive magnetometry usage, I want to thank Dr. Shengqiang Zhou. I also want to thank the positron group, to Dr. Maik Butterling, Dr. Wolfgang Anwand and Dr. Andreas Wagner, for conducting PAS measurements for many of my samples.

I also would like to thank

- Dr. Roman Böttger and Frank Ludewig for ion implantations,
- Dr. Jan Fiedler for transport measurements,
- Dr. Rene Hübner for TEM measurements,
- Dr. Jörg Grenzer and Mrs. Andrea Scholz for XRD measurements,
- Dr. Carsten Bähz, Dr. Valentina Cantelli and Jonathan Ehrler for X-ray absorption measurements.

I am also very grateful to my parents, who raised me with lots of love and patience and supported all of my decisions. Moreover, special thanks to little sister for taking care of my Turkey related personal things, her help and support to me.

Finally and most importantly I thank my beloved wife, who supported me from the very beginning. Just to support me she had to learn German, which is her fifth language, had to pass an exam to practice as a physician, and had to change the country for the second time. There is no word exist to express my gratitude to her.

Ps. During three years of my PhD studies, unfortunately, I have lost many people, Mehmet Dikmen, Ali Öz, Vladimir Stepanyuk, Maria Stepanyuk, Tugce Turkeyilmaz, may they rest in peace.



---

## List of Figures

---

1.1	The energy splitting of the both spin states of an electron. . . . .	3
1.2	Schematic illustration of GMR stack, which consists of two ferromagnetic layers. . . . .	4
1.3	Evolution of the magnetic structure of a DMS. . . . .	6
1.4	Experimental saturation magnetization values of 5 at.% TM doped ZnO films measured at room temperature (TM=Sc-Cu) . . . . .	8
1.5	Transmission electron microscopy images of fine metallic cobalt clusters found in rutile TiO <sub>2</sub> . . . . .	9
1.6	The number of publications on magnetic properties of cobalt doped TiO <sub>2</sub> . . . . .	10
2.1	Possible dopant locations within host oxide lattice, below percolation concentration. . . . .	15
2.2	Calculated Curie temperatures of various p-type DMS materials . . . . .	16
2.3	Bound magnetic polaron formation in the vicinity of the shallow donor states and their percolation . . . . .	18
2.4	Possible defect distributions inside a thin film . . . . .	19
2.5	An illustration of effect of the TM implantation into anatase TiO <sub>2</sub> . . . . .	22
3.1	A schematic view of a DC magnetron sputtering deposition system along with its real image. . . . .	25
3.2	A schematic view of an ion implantation setup along with its elements. . . . .	26
3.3	Ion energy dependent cross-sections for nuclear and electronic stopping. . . . .	27
3.4	A schematic of ion-solid interactions. . . . .	28
3.5	Reflection of X-rays from atomic planes of a crystalline solid. . . . .	30
3.6	An illustration of $2\theta$ - $\theta$ measurement geometry. . . . .	31
3.7	A schematic of synchrotron radiation facility. . . . .	32
3.8	X-rays absorption within a material. . . . .	33
3.9	Transitions of electronic states within an atom. . . . .	33
3.10	An example of a Nb K-edge X-ray absorption spectrum. . . . .	34
3.11	Dual junction (dc) SQUID loop. The capacitor represents the self-capacitance of the junction. . . . .	36
3.12	The configuration of SQUID magnetometer in a MPMS setup. . . . .	36

3.13	The energy distribution of the emitted photons from electron-positron annihilation within a deformed and non-deformed GaAs. . . . .	41
4.1	Schematic of different microstructures of the as-grown films . . . . .	44
4.2	Calculated depth profile of the implanted 4 at.% Co <sup>+</sup> depth distribution . . . . .	46
4.3	XRD pattern of as-grown and 4 at.% Co <sup>+</sup> TiO <sub>2</sub> . . . . .	47
4.4	Measured positron-energy dependent S parameters . . . . .	49
4.5	Field dependent magnetization curves of 4 at.% Co <sup>+</sup> -implanted TiO <sub>2</sub> films . . . . .	50
4.6	Co K-edge XANES spectra of 4 at.% implanted TiO <sub>2</sub> films . . . . .	52
4.7	Depth profiles of Co <sup>+</sup> -implanted into TiO <sub>2</sub> calculated by SRIM. Five different energy fluence combinations have been used to achieve a box like sum profile. . . . .	54
4.8	XRD pattern of as-grown and Co <sup>+</sup> -implanted TiO <sub>2</sub> : a) polycrystalline film in 1° grazing incidence, and b) epitaxial film in aligned symmetric 2θ-ω geometry. The inset in b) shows the anatase TiO <sub>2</sub> (004) rocking curves of the epitaxial film. . . . .	55
4.9	Dark field TEM image of the Co <sup>+</sup> -implanted epitaxial TiO <sub>2</sub> film: a) cross-section overview, b) high magnification image of the implanted area. . . . .	57
4.10	Measured positron-energy dependent S parameters for 5 at.% Co <sup>+</sup> -implanted TiO <sub>2</sub> films. . . . .	58
4.11	Temperature dependent magnetization curves (ZFC/FC) of Co <sup>+</sup> -implanted TiO <sub>2</sub> films with different microstructures. . . . .	59
4.12	Co K-edge XANES spectra (normalized) of Co <sup>+</sup> -implanted epitaxial anatase, polycrystalline anatase and amorphous TiO <sub>2</sub> films together with Co K-edge spectra of Co foil, CoO [114] and CoTiO <sub>3</sub> [115]. . . . .	61
4.13	Room temperature magneto-optic (MO) transversal Kerr effect (TKE) spectra of Co <sup>+</sup> -implanted TiO <sub>2</sub> films with different microstructures. . . . .	62
4.14	Calculated implantation profile for 5 at.% Mn doping into TiO <sub>2</sub> . . . . .	63
4.15	XRD patterns of as-grown and 5 at.% Mn <sup>+</sup> -implanted TiO <sub>2</sub> thin films: (a) polycrystalline films in 1° grazing incidence, and (b) epitaxial films in aligned symmetric 2θ-ω geometry. . . . .	64
4.16	Energy-resolved depth profiles of S parameter for as-grown (a) and Mn <sup>+</sup> -implanted (b) TiO <sub>2</sub> structures. The insets show comparison plots of Mn <sup>+</sup> -implanted and as-grown polycrystalline (a) and epitaxial (b) TiO <sub>2</sub> films. . . . .	65
4.17	Temperature dependent resistivity measurements of Mn <sup>+</sup> -implanted epitaxial and polycrystalline anatase TiO <sub>2</sub> films. . . . .	66
4.18	(a) Mn K-edge XANES spectra of Mn <sup>+</sup> -implanted TiO <sub>2</sub> structures along with reference spectra of MnO [122] and MnTiO <sub>3</sub> [123] (reference spectra shifted in energy axis for clarity by considering the energy calibration of experimental setup).(b) Fourier transform of k <sup>3</sup> -weighted extended XANES spectra of the experimental data. Data was obtained in grazing incidence geometry at 1° to enhance the Mn fluorescence signal. . . . .	68
4.19	Field dependent magnetization curve of Mn:TiO <sub>2</sub> film at 20 K. Inset shows thermal scans in 15 mT of the magnetization of Mn <sup>+</sup> -implanted TiO <sub>2</sub> films with different as-grown microstructures. . . . .	69

4.20	Depth profiles of V <sup>+</sup> -implanted into TiO <sub>2</sub> calculated by SRIM. Five different energy-fluence combinations have been used to achieve a box like sum profile. Fluences for 5 at.% concentration were calculated by simply multiplying each fluence values, which are shown in graph by 5. . . . .	71
4.21	Temperature dependent magnetization curve of 5 at.% V <sup>+</sup> -implanted amorphous TiO <sub>2</sub> . . . . .	72
4.22	Temperature dependent magnetization curve of 5 at.% V <sup>+</sup> -implanted polycrystalline TiO <sub>2</sub> . . . . .	72
4.23	Temperature dependent magnetization curve of 5 at.% V <sup>+</sup> -implanted epitaxial TiO <sub>2</sub> . . . . .	73
4.24	V K-edge X-ray absorption spectrum for 5 at.% V <sup>+</sup> -implanted epitaxial anatase TiO <sub>2</sub> film. . . . .	74
5.1	XANES measurement at Ti K-edge of semiconductor and insulator V:TiO <sub>2</sub> films. . . . .	77
5.2	EDX spectrum of insulating Ti <sub>0.99</sub> V <sub>0.01</sub> O <sub>2-λ</sub> . . . . .	78
5.3	The energy dependent S-parameter measurement of insulating and semiconductor V:TiO <sub>2</sub> . . . . .	79
5.4	Magnetic field dependent magnetization curves of semiconducting and insulating V:TiO <sub>2</sub> films. . . . .	80
5.5	MO spectra for semiconducting and insulating V:TiO <sub>2</sub> , along with Co:TiO <sub>2</sub> reference data. . . . .	80
5.6	Temperature dependent resistivity of semiconducting V:TiO <sub>2</sub> film. . . . .	81
6.1	Evolution of the open-volume defects within different microstructures of as-grown TiO <sub>2</sub> films. . . . .	85
6.2	Formation of metallic cobalt nanoclusters in Co <sup>+</sup> implanted TiO <sub>2</sub> films. . .	86
6.3	Observed magnetic properties of 5 at.% transition metal ion implanted polycrystalline anatase TiO <sub>2</sub> . . . . .	88
6.4	Comparison of energy-resolved S parameters for Co <sup>+</sup> - and Mn <sup>+</sup> -implanted polycrystalline anatase TiO <sub>2</sub> films. . . . .	89



---

## List of Tables

---

4.1	Sample labeling of as-grown TiO <sub>2</sub> films. $T_{substrate}$ stands for the substrate temperature during growth, while $T_{annealing}$ represents in-situ post deposition annealing temperature for 1 hour and performed only for polycrystalline structures. The epitaxial films are labeled after their epitaxial quality, which is altered by applying different substrate temperatures. The qualities were determined from RC measurement and the epitaxial sample which showed narrower RC curve has labeled as high quality (HQ-Epitaxial), while the epitaxial film with broader RC curve has labeled as standard quality (SQ-Epitaxial) (see section 4.2.1.2) . . . . .	46
4.2	Preparation parameters and magnetic properties of the 4 at.% Co <sup>+</sup> implanted TiO <sub>2</sub> films. $T_{substrate}$ shows the substrate temperature during growth, while $T_{postannealing}$ represents in-situ post deposition treatments. $RC\ FWHM$ values for epitaxial structures are given. $N$ is the total number of paramagnetic Co <sup>+2</sup> ions, which are extracted from fit values. Effective Co ions shows the effective number of Co ions compared to whole implantation concentration ( <i>un</i> stands for unheated). . . . .	51
6.1	Microstructure and dopant type dependencies of magnetic properties for 5 at.% transition metal implanted anatase TiO <sub>2</sub> thin films. . . . .	87

---

## Bibliography

---

- [1] H. E. White. *Introduction to Atomic Spectra*. McGraw-Hill Book Company, New York, 1934.
- [2] W. Gerlach and O. Stern. *Zeitschrift fr Physik*, 9:349–352, 1922.
- [3] W. Gerlach and O. Stern. *Zeitschrift fr Physik*, 9:353–355, 1922.
- [4] S. A. Wolf nad D. D. Awschalom, R. A. Buhrman, J. M. Daughton, S. von Molnar, M. L. Roukes, A. Y. Chtchelkanova, and D. M. Treger. *Science*, 294:1488, 2001.
- [5] I. Zutic, J. Fabian, and S. Das Sarma. *Rev. Mod. Phys.*, 76:2, 2004.
- [6] M. N. Baibich, J. M. Broto, A. Fert, F. Nguyen Van Dau, F. Petroff, P. Etienne, G. Creuzet, A. Friederich, and J. Chazelas. *Phys. Rev. Lett.*, 61:2472, 1988.
- [7] G. Binasch, P. Gruenberg, F. Saurenbach, and W. Zinn. *Phys. Rev. B*, 39:4828, 1989.
- [8] G. Prinz. *Science*, 282:1660, 1998.
- [9] J. C. Slonczewski. *J. Magn. Magn. Mater.*, 159:L1, 1996.
- [10] L. Berger. *Phys. Rev. B*, 54:9353, 1996.
- [11] A. Manchon and S. Zhang. *Phys. Rev. B*, 78:212405, 2008.
- [12] F. Matsukura, Y. Tokura, and H. Ohno. *Nature Nanotechnology*, 10:209, 2015.
- [13] B. Lee, T. Jungwirth, and A. H. MacDonald. *Semicond. Sci. Technol.*, 17:393, 2002.
- [14] Science highlights. *Probing the origins of magnetism in Dilute Magnetic Oxides*. [www.diamond.ac.uk](http://www.diamond.ac.uk), 2010.
- [15] J. K. Furdyna. *J. Appl. Phys.*, 64:R29, 1988.

- [16] A. Haury, A. Wasiela, A. Arnoult, J. Cibert, S. Tatarenko, T. Dietl, and Y. M. Aubigne. *Phys. Rev. Lett.*, 79:511, 1997.
- [17] H. Munekata, H. Ohno, S. Vonmolnar, A. Segmuller, L. L. Chang, and L. Esaki. *Phys. Rev. Lett.*, 63:1849, 1989.
- [18] K. Sato, A. Shen, F. Matsukura, A. Oiwa, A. Endo, S. Katsumoto, and Y. Iye. *Appl. Phys. Lett.*, 69:363, 1996.
- [19] H. Ohno, D. Chiba, F. Matsukura, T. Omiya, E. Abe, T. Dietl, Y. Ohno, and K. Ohtani. *Nature*, 408:944, 2000.
- [20] Y. Ohno, D. K. Young, B. Beschoten, F. Matsukura, H. Ohno, and D. D. Awschalom. *Nature*, 402:790, 1999.
- [21] H. Dietl, H. Ohno, F. Matsukura, J. Cibert, and D. Ferrand. *Science*, 287:1019, 2000.
- [22] Y. Matsumoto, M. Murakami, T. Shono, T. Hasegawa, T. Fukumura, M. Kawasaki, P. Ahmet, T. Chikyow, S. Koshihara, and H. Koinuma. *Science*, 291:854, 2001.
- [23] Y. Matsumoto, M. Murakami, T. Shono, T. Hasegawa, T. Fukumura, M. Kawasaki, P. Ahmet, T. Chikyow, S. Koshihara, and H. Koinuma. *J. Jpn. J. Appl. Phys.*, 40:L1204, 2001.
- [24] S. P. Wong, Y. Gao, K. H. cheng, C. F. Chow, N. Ke, W. Y. Cheung, Q. Li, and G. S. Shao. *Proc. SPIE*, 19:III, 2004.
- [25] A. Manivannan, G. Galspell, and M. S. Seehra. *J. Appl. Phys.*, 94:6994, 2003.
- [26] M. Murakami, Y. Matsumoto, T. Hasegawa, P. Ahmet, K. Nakajima, T. Chikyow, H. Ofuchi, and I. Nakai H. Koinuma. *J. Appl. Phys.*, 95:5330, 2004.
- [27] D. H. Kim, J. S. Yang, Y. S. Kim, D. W. Kim, T. W. Noh, S. D. Bu, Y. W. Kim, Y. D. Park, S. J. Pearton, Y. Jo, and J. G. Park. *Appl. Phys. Lett.*, 83:4574, 2003.
- [28] M. Venkatesan, C. B. Fitzgerald, J. G. Lunney, and J. M. D. Coey. *Phys. Rev. Lett.*, 93:177206, 2004.
- [29] Y. W. Heo, M. P. Ivill, and K. Ip. *Appl. Phys. Lett.*, 84(13):2292, 2004.
- [30] N. H. Hong, J. Sakai, and N. T. Huong. *Phys. Rev. B*, 72:045336, 2005.
- [31] D. L. Hou, X. J. Ye, and H. J. Meng. *Appl. Phys. Lett.*, 90:242509, 2007.
- [32] A. Chambers, S. M. Heald, and T. Droubay. *Phys. Rev. B*, 67:100401(R), 2003.
- [33] T. Tietze, M. Gacic, G. Shutz, G. Jakob, S. Bruck, and E. Goering. *New J. Phys.*, 10:055009, 2008.
- [34] B. Vodungbo, F. Vidal, Y. Zheng, M. Marangolo, D. Demaille, V. H. Etgens, J. Varalda, A. J. A. de Oliveira, F. Maccherozzi, and G. Panaccione. *J. Phys.: Condens. Mater.*, 20:125222, 2008.

- [35] T. Hitosugi, G. Kinoda, Y. Yamamoto, Y. Furubayashi, K. Inaba, Y. Hirose, K. Nakajima, T. Chikyow, T. Shimada, and T. Hasegawa. *J. Appl. Phys.*, 99:08M121, 2006.
- [36] Z. Wang, W. Wang, J. Tang, L. D. Tung, L. Spinu, and W. Zhou. *Appl. Phys. Lett.*, 83:518, 2003.
- [37] H. Ohno, A. Shen, F. Matsukura, A. Owia, A. Endo, S. Katsumoto, and Y. Iye. *Appl. Phys. Lett.*, 69:363, 1996.
- [38] F. Matsukura, H. Ohno, A. Shen, and Y. Sugawara. *Phys. Rev. B*, 57:R2037(R), 1998.
- [39] T. S. Krasienapibal, S. Inoue, T. Fukumura, and T. Hasegawa. *Appl. Phys. Lett.*, 106:202402, 2015.
- [40] R. J. Kennedy, P. A. Stampe, H. Erhong, X. Peng, S. Von Molnar, and X. Yan. *Appl. Phys. Lett.*, 84:2832, 2004.
- [41] S. R. Shinde, S. B. Ogale, J. S. Higgins, H. Zheng, A. J. Millis, V. N. Kulkarni, R. Ramesh, R. L. Greene, and T. Venkatesan. *Phys. Rev. B*, 67:115211, 2003.
- [42] K. A. Griffin, A. B. Pakhomov, C. M. Wang, S. M. Heald, and K. M. Krishnan. *J. Appl. Phys.*, 97:10D320, 2005.
- [43] S. R. Shinde, S. B. Ogale, J. S. Higgins, H. Zheng, A. J. Millis, V. N. Kulkarni, R. Ramesh, R. L. Greene, and T. Venkatesan. *Phys. Rev. Lett.*, 92:16, 2004.
- [44] S. Ghosh, G. G. Khan, and K. Mandal. *EPJ Web of Conferences*, 40:03001, 2013.
- [45] J. Ran and Z. Yan. *Journal of Semiconductors*, 30:10, 2009.
- [46] P. Esquinazi, W. Hergert, D. Spemann, A. Setzer, and A. Ernst. *IEEE Magn. Trans.*, 49:4668, 2013.
- [47] T. Tietze, P. Audehm, Y. C. Chen, G. Shuetz, B. B. Straumal, S. G. Protasova, A. A. Mazilkin, P. B. Straumal, T. Prokscha, H. Luetkens, Z. Salman, A. Suter, B. Baretzky, K. Fink, W. Wenzel, D. Danilov, and E. Goering. *Scientific Reports*, 5:8871, 2015.
- [48] Y. Yamada, K. Ueno, T. Fukumura, H. T. Yuan, H. Shimotani, Y. Iwasa, L. Gu, S. Tsukimoto, Y. Ikuhara, and M. Kawasaki. *Science*, 332:1065, 2011.
- [49] N. N. Hai, N. T Khoi, and P. V. Vinh. *J. Phys.: Conf. Series*, 187:012071, 2009.
- [50] J. M. D. Coey, M. Venkatesan, and C. B. Fitzgerald. *Nature Materials*, 4:173, 2005.
- [51] B. B. Straumal, A. A. Mazilkin, S. G. Protasova, A. A. Myatiev, P. B. Straumal, G. Shuetz, P. A. Aken, E. Goering, and B. Baretzk. *Phys. Rev. B*, 79:205206, 2009.
- [52] Y. B. Nian, J. Strozieri, N. J. Wu, X. Chen, and A. Ignatiev. *Phys. Rev. Lett.*, 98:146403, 2007.

- [53] W. Yan, Z. Sun, Z. Pan, Q. Liu, T. Yao, Z. Wu, C. Song, F. Zeng, Y. Xie, T. Hu, and S. Wei. *Appl. Phys. Lett.*, 94:042508, 2009.
- [54] J. M. D. Coey, P. Stamenov, R. D. Gunning, M. Venkatesan, and K. Paul. *New Journal of Physics*, 12:053025, 2010.
- [55] M. J. Calderon and S. Das Sarma. *Annals of Physics*, 322:2618, 2007.
- [56] Y. Matsumoto, M. Murakami, T. Hasegawa, T. Fukumura, M. Kawasaki, P. Ahmet, K. Nakajima, T. Chikyow, and H. Koinuma. *Appl. Surf. Sci.*, 189:344, 2002.
- [57] M. Murakami, Y. Matsumoto, K. Nakajima, T. Makino, Y. Segawa, T. Chikyow, P. Ahmet, M. Kawwasaki, and H. Koinuma. *Appl. Phys. Lett.*, 78:18, 2001.
- [58] T. Zhao, S. R. Shinde, S. B. Ogale, H. Zheng, T. Venkatesan, R. Ramesh, and S. D. Sarma. *Phys. Rev. Lett.*, 94:126601, 2005.
- [59] K. A. Griffin, A. B. Pakhomov, C. M. Wang, S. M. Heald, and K. M. Krishnan. *Phys. Rev. Lett.*, 94:157204, 2005.
- [60] J. B. Torrance, M. W. Shafer, and T. R. McGuire. *Phys. Rev. Lett.*, 29:1168, 1972.
- [61] D. Menzel, I. Jursic, J. Schoenes, F. Iacomi, and D. Caccina. *Phys. Stat. Sol. (c)*, 3:4119–4122, 2006.
- [62] L. R. Shah, W. Wang, H. Zhu, B. Ali, Y. Q. Song, H. W. Zhang, S. I. Shah, and J. Q. Xiao. *J. Appl. Phys.*, 105:07C515, 2009.
- [63] T. C. Kaspar, S. M. Heald, C. M. Wang, J. D. Bryan, T. Droubay, V. Shutthanandan, S. Thevuthasan, D. E. McCready, A. J. Kellock, D. R. Gamelin, and S. A. Chambers. *Phys. Rev. Lett.*, 95:217203, 2005.
- [64] H. Bednarski and J. Spalek. *J. Phys.: Condens. Matter*, 24:235801, 2012.
- [65] H. P. Gunnlaugsson, R. Mantovan, H. Masenda, T. E. Molholt, K. Johnston, K. Bharuth-Ram, H. Gislason, G. Langouche, D. Naidoo, S. Olafsson, A. Svanne, and G. Weyer. *Phys. Rev. B*, 54:9353, 1996.
- [66] K. Potzger, S. Zhou, J. Grenzer, M. Helm, and J. Fassbender. *Appl. Phys. Lett.*, 92:182504, 2008.
- [67] B. Santara, P. K. Giri, K. Imakita, and M. Fuji. *J. Phys. D: Appl. Phys.*, 47:235304, 2014.
- [68] A. Barla, G. Schmerber, E. Beaurepaire, A. Dinia, H. Bieber, S. Colis, F. Scheurer, J. P. Kappler, P. Imperia, F. Nolting, F. Wilhelm, A. Rogalev, D. Mueller, and J. J. Grob. *Phys. Rev. B*, 76:125201, 2007.
- [69] G. Z. Xing, Y. H. Lu, Y. F. Tian, J. B. Yi, C. C. Lim, Y. F. Li, G. P. Li, D. D. Wang, B. Yao, J. Ding, Y. P. Feng, and T. Wu. *AIP Advances*, 1:022152, 2011.

- [70] S. Zhou, K. Potzger, G. Talut, H. Reuther, K. Kueoer, J. Grenzer, Q. Xu, A Mcklich, M. Helm, and J. Fassbender. *J. Phys.D: Appl. Phys.*, 41:105011, 2008.
- [71] A. Chambers. *Surf. Sci. Rep*, 61:345, 2006.
- [72] T. Dietl and H. Ohno. *Materials Today*, 9:18, 2006.
- [73] D. W. Abraham, M. M. Frank, and S. Guha. *Appl. Phys. Lett.*, 87:252502, 2005.
- [74] J. M. D. Coey, P. Stamenov, R. D. Gunning, M. Venkatesan, and K. Paul. *New J. Phys.*, 12:053025, 2010.
- [75] S. Cornelius. *PhD Thesis*. Helmholtz-Zentrum Dresden - Rossendorf, TU Dresden, 2014.
- [76] Rob Pearson. *Rochester Institute of Technology*. <http://aplusphysics.com/flux/tag/microelectronics/>, 2012.
- [77] S. M. Rossnagel. *Opportunities for Innovation: Advanced Surface Engineering*. Technomic Publishing Co., Switzerland, 1995.
- [78] wikiwand. *Stopping power (particle radiation)*. wikipedia, [www.wikiwand.com/en/Stopping-power-particle-radiation](http://www.wikiwand.com/en/Stopping-power-particle-radiation), 20.10.2015.
- [79] Wolfhard Möller. *Fundamentals of Ion-Solid Interaction*. HZDR-internal, Dresden, 2013.
- [80] J. S. Williams and J. M. Poate. *Ion implantation and Beam processing*. Academic Press Australia, North Ryde, 1984.
- [81] K. Potzger. *Nucl. Instr. Meth. Phys. B*, 272:78, 2012.
- [82] B. D. Cullity. *Elements of X-ray diffraction*. Addison-Wesley Publishing Company Inc., Massachusetts, USA, 1956.
- [83] Arthur L. Robinson. *History of Synchrotron Radiation*. available online at <http://xdb.lbl.gov/Section2/Sec2-2.html>, Berkeley Lab., 2014.
- [84] booklet. *The working principles and the instrumentation of the BESSY synchrotron radiation facility*. BESSY, Berlin, 2004.
- [85] B. K. Teo. *Inorganic Chemistry Concepts*, 9:1, 1986.
- [86] E. A. Stern. *Theory of EXAFS. X-Ray Absorption: Principles, Applications, Techniques of EXAFS, SEXAFS and XANES*. Wiley, New York, 1988.
- [87] B. K. Agarwal. *X-Ray Spectroscopy: An Introduction*. Springer - Verlag, Berlin, 1991.
- [88] T. Vitova. *X-ray absorption spectroscopy investigation of structurally modified lithium niobate crystals, PhD Thesis*. Bonn University, Bonn, 2008.

- [89] B. Ravel. *J. Alloys Compd.*, 401:118, 2005.
- [90] Y. Zhao C. Park Y. Meng S. V. Sinogeikin G. Shen L. Bai, M. Pravica. *J. Phys.: Condens. Matter.*, 24:435401, 2012.
- [91] R. L. Fagaly. *SQUID instruments and applications*. Tristan Technologies, San Diego, 2004.
- [92] B. D. Josephson. *Phys. Lett.*, 1:251, 1962.
- [93] C. D. Tesche and J. Clarke. *J. Low Temp. Phys.*, 29:301, 1982.
- [94] J. Clarke. *Squid sensors: Fundamentals, fabrication and applications*. Kluwer Academic, London, 1997.
- [95] R. Krause-rehberg and H. Leipner. *Positron Annihilation in Semiconductors*. Springer-Verlag, Berlin, 1999.
- [96] O. V. Boev, M. J. Puska, and R. M. Nieminen. *Phys. Rev. B*, 36:7786, 1987.
- [97] I. Makkonen, A. Snicker, M. J. Puska, J.-M-Maki, and F. Tuomisto. *Phys. Rev. B*, 82:041307, 2010.
- [98] R. Krause-Rehberg. *Fundamentals of positron annihilation spectroscopy and its applications in semiconductor*, Lecture:Halle–Wittenberg, 2015.
- [99] W. Anwand, G. Brauer, M. Butterling, H. R. Kissener, and A. Wagner. *Defect and Diffusion Forum*, 331:25–40, 2012.
- [100] J. Ziegler, J. Biersack, and U. Littmark. *The stopping and range of ions in matter*. Pergamon, New York, 1985.
- [101] S.A Chambers, S. Thevuthasan, R.F.C. Farrow, R.F. Marks, J.U. Thiele, M.G. Samant L. Folks, A.J Kellock, N. Ruzycki, D.L Ederer, and U. Diebold. *Appl. Phys. Lett.*, 40:Part2, L1204, 2001.
- [102] L. C. Feldman, J. W. Mayer, and S. T. Picraux. *Materials analysis by ion channeling: submicron crystallography*. Academic Press, New York, 1982.
- [103] W. Möller. *Ion Beams in materials processing and analysis*. Springer, Wien, 2012.
- [104] L. Sangaletti, M. C. Mozatti, P. Galinetto, C. B. Azzoni, A. Speghini, M. Bettinelli, and G. Calestani. *J. Phys.: Condens. Matter*, 18:7643, 2006.
- [105] S. A. Chambers, S. M. Heald, and T. Droubay. *Phys. Rev. B.*, 67:100401, 2003.
- [106] K. S. Lin, H. W. Cheng, W. R. Chen, and J. F. Wu. *J. Environ. Eng. Manage.*, 20(2):69, 2010.
- [107] W. Yan, Z. Sun, Z. Pan, Q. Liu, T. Yao, Z. Wu, C. SOng, F. Zeng, Y. Xie, T. Hu, and S. Wei. *Appl. Phys. Lett.*, 94:042508, 2009.

- [108] V. Shutthanandan, S. Thevuthasan, S. M. Heald, M. H. Engelhardt, T. C. Kaspar, D. E. McReady, L. Saraf, S. A. Chambers, B. S. Mun, N. Hamdan, P. Nachimuthu, B. Taylor, R. P. Sears, and B. Sinkovic. *Science*, 291:854, 2001.
- [109] N. T. Nolan, M. K. Seery, and S. C. Oillai. *J. Phys. Chem.*, 113:16151, 2009.
- [110] B. D. Cullity. *Introduction to Magnetic Materials*. Addison-Wesley, New York, 1972.
- [111] S. Takada, M. Fuji, S. Kohiki, T. Babasaki, H. Deguchi, M. Mitome, and M. Oku. *Nano Lett.*, 1:379, 2001.
- [112] D. Brankovic, V. Jonakovic, B. Babic-Stojic, Z. Jaglicic, D. Lisjak, and D. Kojic. *J.Phys.: Condens. Mater.*, 21:095303, 2009.
- [113] R. C. O'Handley. *Modern Magnetic Materials*. Wiley, New York, 2000.
- [114] S. Disch and. *The Spin Structure of Magnetic Nanoparticles and in Magnetic Nanostructures*. Forschungszentrum Julich GmbH, Julich, 2011.
- [115] T. Jiang and D. E. Ellis. *J. Mater. Sci*, 11:2242, 1996.
- [116] J. W. D. Martens, W. L. Peeters, H. M. Van Noort, and M. Erman. *J. Phys. Chem. Solids*, 46:4, 1985.
- [117] R. Newman and R. M. Chrenko. *Phys. Rev.*, 115:1, 1959.
- [118] H. Tang, K. Prasad, R. Sanjines, P. E. Schmid, and F. Levy. *J. Appl. Phys.*, 75:2042, 1994.
- [119] E. A. Ganshina, A. B. Granovsky, A. F. Orlov, N. S. Perov, and M. V. Vashuk. *J. Magn. Magn. Mat*, 321:723, 2009.
- [120] P. Esquinazi, W. Hergert, D. Sperman, A. Setzer, and A. Ernst. *IEEE Trans. Magn.*, 48(8):4668, 2013.
- [121] Y. Furubayashi, T. Hitosugi, Y. Yamamoto, K. Inaba, G. Kinoda, Y. Hirose, T. Shimada, and T. Hasegawa. *Appl. Phys. Lett.*, 86:252101, 2014.
- [122] K.-W. Nam, M. G. Kim, and K.-B. Kim. *J. Phys. Chem. C*, 111:749–758, 2007.
- [123] M. Valant, T. Kolodiazhnyi, I. Arcon, F. Aguesse, A.-K. Axelsson, and N. M. Alford. *Adv. Funct. Mater.*, 22:2114–2122, 2012.
- [124] L. Zhang, J. Li, Y. Du, J. Wang, X. Wei, J. Zhou, J. Cheng, W. Chu, Z. Jiang, Y. Huang, C. Yan, S. Zahng, and Z. Wu. *New Journal of Physics*, 14:013033, 2012.
- [125] S. W. Chen, P. A. Lin, H. T. Jeng, S. W. Fu, J. M. Lee, J. F. Lee, C. W. Pao, H. Ishii, K. D. Tsuei, N. Hiraoka, D. P. Chen, S. X. Dou, X. L. Wang, K. T. Lu, and J. M. Chen. *Appl. Phys. Lett.*, 104:082104, 2014.



- [126] G. Vlaic, J. C. J. Bart, W. Cavigiolo, S. Mobilio, and G. Navarra. *Z. Naturforsch.*, 86a:1192–1195, 1981.
- [127] T. Nedoseykina, M. G. Kim, S.-A. Park, H.-S. Kim, S.-B. Kim, J. Cho, and Y. Lee. *Electrochimica Acta*, 55:8876–8882, 2010.
- [128] D. P. Shoemke, M. Grossman, and R. Seshadri. *J. Phys.: Condens. Matter*, 20:195219, 2008.
- [129] Z. Ge, W. L. Lim, S. Shen, Y. Y. Zhou and dX. Liu, J. K. Furdyna, and M. Dobrowolska. *Phys. Rev. B*, 75:014407, 2007.
- [130] A. Kaminski and S. Das Sarma. *Phys. Rev. Lett.*, 88:247202, 2002.
- [131] H. Chou, C. P. Lin, J. C. A. Huang, and H. S. Hsu. *Phys. Rev. B*, 77:245210, 2008.
- [132] B. Poumellec, R. Cortes, C. Sanchez, J. Berthon, and C. Fretigny. *J. Phys. Chem. Solids*, 54:751, 1993.
- [133] A. Semisalova, Yu. O. Mikhailovskiy, and A. Smekhova et. al. *JSNM*, 28:805, 2015.
- [134] N. H. Hong, J. Sakai, and A. Hassini. *Appl. Phys. Lett.*, 84:2606, 2004.
- [135] A. F. Orlov, L. A. Balagurov, and I. V. Kulemanov. *SPIN*, 2:1250011, 2012.
- [136] J. Osorio-Guillen, S. Lany, and A. Zunger. *Phys. Rev. Lett.*, 100:036601, 2008.
- [137] A. Lotnyk, S. Senz, and D. Hesse. *Thin Solid Films*, 515:3439–3447, 2007.
- [138] N. Akdogan, A. Nefedov, H. Zabel, K. Westerholt, H. W. Becker, C. Somsen, S. Gok, A. Bashir, R. Khaibullin, and L. Tagirov. *J. Phys. D.: Appl. Phys.*, 42:115005, 2009.
- [139] O. Volnianska and P. Boguslawski. *J. Phys.: Condens. Matter*, 22:073202, 2010.

## List of publications

- 1- “Ferromagnetism and structural defects in V-doped titanium dioxide”, **O. Yildirim**, M. Butterling, Y. Mikhailovsky, A. Novikov, A. Semisalova, A. Orlov, E. Ganshina, N. Perov, W. Anwand, A. Wagner, K. Potzger, A.B. Granovsky, A. Smekhova, Phys. Stat. Sol. **11**, 1106 (2014)
- 2- “Above room temperature ferromagnetism in Co-and V-Doped TiO<sub>2</sub>-revealing the different contributions of defects and impurities”, A.S. Semisalova, Yu. O. Mikhailovsky, A. Smekhova, A.F. Orlov, N.S. Perov, E.A. Ganshina, A. Lashkul, E. Lhderanta, K. Potzger, **O. Yildirim**, B. Aronzon, A.B. Granovsky, JOSCS, **28**, 2776 (2014)
- 3-“Influence of film thickness and composition on the martensitic transformation in epitaxial NiMnSn thin films”, N. Teichert, A. Auge, E. Yzak, I. Dincer, Y. Elerman, B. Krumme, H. Wende, **O. Yildirim**, K. Potzger, A. Hutten, Acta Mater. **86**, 279 (2015)
- 4-“Direct measurement of the magnetic anisotropy field in Mn–Ga and Mn–Co–Ga Heusler films”, C. Fowley, S. Ouardi, T. Kubota, **O. Yildirim**, A. Neudert, K. Lenz, V. Sluka, J. Lindner, J. M. Law, S. Mizukami, G. H. Fecher, C. Felser, A. M. Deac, J. Phys.: Appl. Phys. **48**, 164006 (2015)
- 5-“Structure and Giant Inverse Magnetocaloric Effect of Epitaxial Ni-Co-Mn-Al Films”, N. Teichert, D. Kucza, **O. Yildirim**, E. Yuzuak, I. Dincer, A. Behler, L. Helmich, A. Boehnke, S. Klimova, A. Waske, Y. Elerman, A. Hutten, Phys. Rev. B, **91**, 18 (2015)
- 6-“The local environment of cobalt in amorphous, polycrystalline and epitaxial anatase TiO<sub>2</sub>: Co films produced by cobalt ion implantation”, **O. Yildirim**, S. Cornelius, A. Smekhova, G. Zykov, E.A. Ganshina, A.B. Granovsky, R. Huebner, C. Baetz, K. Potzger, J. Appl. Phys. **117**, 18 (2015)
- 7- “From a non-magnet to a ferromagnet: Mn implantation into different TiO<sub>2</sub> structures”, **O. Yildirim**, S. Cornelius, M. Butterling, W. Anwand, A. Wagner, A. Smekhova, J. Fiedler, C. Baetz, R. Böttger, K. Potzger, Appl. Phys. Lett. **107**, 242405 (2015)
- 8- “Tuning the antiferromagnetic to ferromagnetic phase transition in FeRh thin films by means of low-energy/low fluence ion irradiation”, A. Heidarian, R. Bali, J. Grenzer, R. A. Wilhelm, R. Heller, **O. Yildirim**, J. Lindner, and K. Potzger, Nucl. Instr. Meth. Phys. Res. B **358**, 251-254 (2015)
- 9-“Evolution of the perpendicular magnetic anisotropy in MgO/CoFeB/Ta/Ru based multilayers as a function of annealing temperature”, Y. Aleksandrov, C. Fowley, E. Kowalska, V. Sluka, **O. Yildirim**, J. Lindner, B. Ocker, J. Fassbender, A. Deac, APEX **submitted**, (2015)
- 10-“Threshold concentration for ion implantation-induced Co nanocluster formation

in TiO<sub>2</sub>:Co thin films”, **O. Yildirim**, S. Cornelius, A. Smekhova, M. Butterling, W. Anwand, A. Wagner, C. Baetz, R. Böttger, K. Potzger, Nucl. Instr. Meth. Phys. Res. B **submitted**

11-“Absence of ferromagnetism in V implanted TiO<sub>2</sub> structures”, **O. Yildirim**, S. Cornelius, A. Smekhova, J. Ehrler, C. Baetz, K. Potzger, **in preparation**

12-“Magnetic and structural studies of Mg<sub>2</sub>Fe<sub>(x)</sub>Si<sub>(1-x)</sub> hydrides”, T. Trinh, **O. Yildirim**, W. Anwand, M. O. Liedke, J. Grenzer, K. Potzger, J. Lindner, K. Asano, B. Dam, **in preparation**

### **Awards**

1- “QD Preisausschreiben”, Quantum Design user award, DPG-Tagung 2015, Berlin.

2- “Recognized Reviewer”, of Journal of Alloys and Compounds, since July 2015.

## **Erklärung**

Hiermit versichere ich, dass ich die vorliegende Arbeit ohne unzulässige Hilfe Dritter und ohne Benutzung anderer als der angegebenen Hilfsmittel angefertigt habe; die aus fremden Quellen direkt oder indirekt übernommenen Gedanken sind als solche kenntlich gemacht. Die Arbeit wurde bisher weder im Inland noch im Ausland in gleicher oder ähnlicher Form einer anderen Prüfungsbehörde vorgelegt.

Die vorliegende Arbeit wurde am Institut für Ionenstrahlphysik und Materialforschung im Helmholtz-Zentrum Dresden-Rossendorf e.V. unter der wissenschaftlichen Betreuung von Herr Prof. Dr. Jürgen Faßbender und Herr Dr. Kay Potzger angefertigt. Die Promotionsordnung der Fakultät für Mathematik und Naturwissenschaften der Technischen Universität Dresden in der Fassung vom 23.02.2011 erkenne ich an.

Dresden, November 2015

Oğuz Yıldırım